Spin-Orbit Torque Magnetization Switching in Co/Pt Multilayers for Multistate Memory and Logic Devices

Gerard Joseph Lim

SCHOOL OF PHYSICAL AND MATHEMATICAL SCIENCES

2020

Spin-Orbit Torque Magnetization Switching in Co/Pt Multilayers for Multistate Memory and Logic Devices

Gerard Joseph Lim

SCHOOL OF PHYSICAL AND MATHEMATICAL SCIENCES

A thesis submitted to the Nanyang Technological University in partial fulfilment of the requirement for the degree of Doctor of Philosophy

2020

Statement of Originality

I hereby certify that the work embodied in this thesis is the result of original research done by me except where otherwise stated in this thesis. The thesis work has not been submitted for a degree or professional qualification to any other university or institution. I declare that this thesis is written by myself and is free of plagiarism and of sufficient grammatical clarity to be examined. I confirm that the investigations were conducted in accord with the ethics policies and integrity standards of Nanyang Technological University and that the research data are presented honestly and without prejudice.

11 Aug 2020

. . . .

Date   Gerard Joseph Lim

Supervisor Declaration Statement

I have reviewed the content and presentation style of this thesis and declare it of sufficient grammatical clarity to be examined. To the best of my knowledge, the thesis is free of plagiarism and the research and writing are those of the candidate's except as acknowledged in the Author Attribution Statement. I confirm that the investigations were conducted in accord with the ethics policies and integrity standards of Nanyang Technological University and that the research data are presented honestly and without prejudice.

11 Aug 2020

. . . .

Date

. . . .

Prof. Lew Wen Siang

Authorship Attribution Statement

This thesis contains material from 3 papers published in the following peer-reviewed journals in which I am listed as an author.

Chapter 5 is published as G. J. Lim, W. L. Gan, W. C. Law, C. Murapaka, W. S. Lew, "Spin-Orbit Torque Induced Multi-State Magnetization Switching in Co/Pt Hall Cross Structures at Elevated Temperatures". *J. Magn. Magn. Mater.*, 514, 167201 (2020)

DOI: 10.1016/j.jmmm.2020.167201.

The contributions of the co-authors are as follows:

- I designed the experiment and prepared the manuscript drafts.
- The manuscript was revised together with W. L. Gan, W. C. Law, and C. Murapaka
- I processed and analyzed the data.
- Kerr microscopy images was performed with the help of W. L. Gan.
- W. C. Law performed vibrating sample magnetometer measurements.
- Prof. W. S. Lew edited the manuscript drafts.

Chapter 6 is published as G. J. Lim, W. L. Gan, W. S. Lew, “Effect of Seed and Interlayer Pt Thickness on Spin-Orbit Torque Efficiency in Co/Pt Multilayer with Perpendicular Magnetic Anisotropy”, *J. Phys. D.*, 53, 505002 (2020)

DOI: 10.1088/1361-6463/abacef

The contributions of the co-authors are as follows:

- I designed the experiment, performed the finite element and micromagnetic simulations, and prepared the manuscript drafts.
- The manuscript was revised together with W. L. Gan, and Prof. W. S. Lew.
- Kerr microscopy images was performed with Gan Weiliang.
- Prof. W. S. Lew edited the manuscript drafts.

Chapter 7 is published as G. J. Lim, D. Chua, W. L. Gan, C. Murapaka, W. S. Lew, "Programmable Spin-Orbit-Torque Logic Device with Integrated Bipolar Bias Field for Chirality Control", *Adv. Electron. Mater.*, 6, 1901090. (2020)

DOI: 10.1002/aelm.201901090

The contributions of the co-authors are as follows:

- C. Murapaka and I came up with the experimental design.
- I wrote the drafts of the manuscript. The manuscript was revised together with D. Chua, W. L. Gan, and C. Murapaka.
- Kerr microscopy images was performed the help of W. L. Gan.
- D. Chua and I prepared the SPICE modelling and simulation.
- Prof W. S. Lew edited the manuscript drafts.

11 Aug 2020

. . . .

Date   Gerard Joseph Lim

Abstract

Spintronics is a highly researched topic for its rich underlying physics as well as for practical applications such as in magnetic random-access memory (MRAM). It has proven to be a serious contender in emerging memory technology due to its intrinsic non-volatility, low power dissipation, and high speed. The spin degree of freedom further opens opportunities that exploit its ultrafast dynamics and spin transport. Instead of transistors and charge-based elements, spintronic devices use the magnetization state in a ferromagnetic material to store and interpret information. More recently, spintronic devices have been proposed for logical, neuromorphic, and compute-in-memory applications. Further investigation on material and device physics are crucial for developing new spintronic memory and computation elements.

In this thesis, the quantification and optimization of current-induced spin-orbit torques (SOT) in [Co/Pt] multilayers are investigated. The thin film multilayer exhibiting perpendicular magnetic anisotropy (PMA) is characterized using adiabatic harmonic Hall measurements for SOT efficiency optimization. Due to the complex structure, the effect of Pt seed and interlayer thickness on the magnetic properties and SOT efficiency is studied. Manipulation of magnetization for multistate memory and logic functionality is also explored. Multistate magnetization switching, useful for synaptic applications due to the analogue-like behaviour, is experimentally demonstrated in a Hall cross device. Through finite element and Mumax simulations, the analogue-like response is shown to be a result of the geometrically-induced inhomogeneous current-density profile of the Hall cross structure. The thermal impact on the multi-state device operation is also studied through multi-state switching at elevated device temperatures. A compound structure using similar switching techniques is used to develop a reconfigurable logic device, in which an integrated bias field line

allows for on-chip local Oersted field generation for breaking the switching symmetry in PMA devices. The logic device is then used to construct a half-adder through the circuit simulator "Simulation Program with Integrated Circuit Emphasis" (SPICE). The results from the works presented in this thesis aims to provide a platform from which to develop more efficient SOT-driven spintronic memory and logic devices.

Acknowledgements

I would like to express my gratitude to all who have been a part of this journey, for their technical input, critical advice, relentless support, as well as for the casual discussions and social gatherings that were just as important.

I would like to first and foremost thank my supervisor, Prof. Lew Wen Siang, for granting me the opportunity of pursuing research work in his group. He has been a mentor and a teacher, providing technical insights and sharing his experience from my time as an undergraduate student thru this PhD journey.

I would also like to thank all whom I've worked closely with – Dr. Gan Weiliang, Dr. Law Wai Cheung, Dr. Tan Funan, Dr. Luo Feilong, Dr. Shawn Wong, Dr. Roger Soh, Dr. Jin Tianli, Calvin Ang, Putu Andhita Dananjaya, Grayson Wong, Shane Wong, and many others over the course of my PhD. I also had the pleasure of interacting with some visiting students in our group – Wang Xuan and Xu Zhan. I've also had the opportunity to learn from the brilliant staff who brought with them their vast experience – Dr. Lai Weng Hong, Dr. Ee Yong Chiang, Dr. Somsubhra Charkrabhati, Dr. Chandrasekhar Murapaka, Dr. Goolaup Sarjoosing, Dr. Chandrasekhar Murapaka, Dr. Kwon Jaesuk, Louis Retnam, Henry Kwang, and Hoo Siew Wei. I'd also like to express appreciation and gratitude to the faculty and staff at the School of Physical and Mathematical Sciences, Nanyang Technological University. Many others whom I have missed mentioning, but am as appreciative of having the opportunity to work with and learn from!

Most importantly, I'd like to thank my family for their support and patience. They have always provided me with encouragement in all my endeavours. [C]

Table of Contents

Abstract 8

Acknowledgements 10

Table of Contents 11

List of Figures 15

List of Tables 25

Acronyms 26

Chapter 1 Introduction 29

1.1 Objective of this Thesis 31

Chapter 2 Spintronic Devices 34

2.1 Spintronics for Logic Applications 37

2.2 Spintronics for Neuromorphic Engineering 39

2.2.1 Spintronic Synapses 41

2.2.2 Spintronic Neurons 43

2.3 Spintronics for Probabilistic Computing 48

Chapter 3 Magnetism and Spintronics 50

3.1 Orbital and Spin Angular Momentum 50

3.2 Magnetic Interactions, Energies, and Fields 52

3.2.1 Symmetric Exchange Interaction 52

3.2.2 Asymmetric Exchange Interaction (Dzyaloshinskii-Moriya Interaction) 53

3.2.3 Zeeman Energy 54

3.2.4 Anisotropy Energy 54

3.2.5 Demagnetization Energy 55

3.3 Stoner-Wohlfarth Model 56

3.4 Dynamic Equation 58

3.5 Spin Tranport 61
3.5.1 Spin Currents 61
3.5.2 Characteristic Lengths 62
3.5.3 Two-Channel Model 63
3.5.4 Decoupling of the Charge and Spin Quantities 65
3.5.5 Diffusion Equations 66
3.6 Spin Transfer Torque 67
3.7 Spin Orbit Coupling 68
3.7.1 Spin Hall Effect 69
3.7.2 Rashba Effect 72
3.7.3 Spin Orbit Torque 72
3.7.4 Anomalous Hall Effect 73
Chapter 4 Fabrication and Characterization Techniques 75
4.1 Device Fabrication 75
4.1.1 Thin Film Sputtering 76
4.1.2 Electron Beam Lithography 78
4.1.3 Resist Spin Coating 79
4.1.4 Ion Beam Etching 81
4.2 Characterization Techniques 83
4.2.1 Surface Resistance and Resistivity 83
4.2.2 Vibrating Sample Magnetometer 85
4.2.3 DC Measurements 86
4.2.4 Harmonic Hall Measurement 88
4.2.5 Kerr Microscopy 90
Chapter 5 Spin-Orbit Torque Induced Multi-State Magnetization Switching in Hall Cross Structure at Elevated Temperatures 92
5.1 Motivation 92
5.2 Experimental Details 93

5.3 Multi-State Behaviour by Current-Induced Spin-Orbit Torque Magnetization Switching 95
5.4 Effect of Elevated Device Temperature on Reading and Writing..........97
5.5 Effective Out-Of-Plane Field Due to Current-Induced Spin-Orbit Torque at Elevated Temperature 99
5.6 Conclusion 104
Chapter 6 Effect of Seed and Interlayer Pt on SOT Efficiency 106
6.1 Motivation...106
6.2 Experimental Details...108
6.3 Current Shunting Due to Varying Seed and Interlayer Pt Thicknesses111
6.4 Quantification of SOT Efficiency...113
6.5 Conclusion 118
Chapter 7 Programmable Spin-Orbit Torque Logic Device with Integrated Bipolar Bias Field for Chirality Control 120
7.1 Motivation...120
7.2 Experimental Details...122
7.3 Logic Operation With a Double Hall Cross Device 124
7.4 Integrated Bias Field Line for Self-Contained Chirality Control.........128
7.5 Simulation of SOT-Driven Reconfigurable Logic Device and Half-Adder 130
7.6 Conclusion 134
Chapter 8 Conclusion and Future Works 136
8.1 Conclusion 136
8.2 Future Works 138
8.2.1 Characterization of New Materials with Large SOC for High-Efficiency Current-Induced SOT Magnetization Switching......138
8.2.2 VCMA-Assisted Magnetization Switching...............................138
8.2.3 Stochastic MTJ as a Multistate Device 139
Appendix A Analytical Derivation for Harmonic Measurement................141
A1 Magnetization Angle Due to Effective Magnetic Fields......................141

A2 Determining the Equilibrium Magnetization Direction 142
A3 Effect of Current-Induced Effective Fields on the Magnetization 144
A4 Expression for the Hall voltage 148
A5 Angular Dependence of the SOT Effective Fields for Out-Of-Plane Magnetized Systems 151
Appendix B SPICE Circuit Modelling 157
B1 Landau-Lifshitz-Gilbert Model 157
B2 Spin Hall Effect Module 159
B3 Anomalous Hall Effect Module 166
B4 SPICE Simulations 166
Appendix C Implementation of Multistate Device in a Hopfield Network 169
C1 Hopfield Network 169
C2 Training 171
C3 Hardware Implementation 172
Bibliography 177
List of Publications 200
List of Conferences 203
List of Intellectual Properties 205
Award 205

List of Figures

Figure 1: Memory-storage hierarchy showing different classes of memory based on their response time, capacity, and complexity. 30

Figure 2: (a) Ferromagnetic wire. (b) Current-in-plane spin valve. (c) Current-perpendicular-to-plane spin valve. (d) Magnetic tunnel junction. Black arrows indicate the flow of current Ic. Red and blue arrows indicate pinned and free magnetic layers, respectively. 35

Figure 3: (a) Toggle MTJ. (b) Thermally-assisted MTJ. (c) STT-MTJ. (d) SOT-MTJ. (e) DW-MTJ. Device resistance states are probed by a read current represented by a thin black arrow through the MTJ stack. Bold black arrows indicate write line current for field-induced magnetization switching of toggle and thermally-assisted MTJs...37

Figure 4: Distinctive symbols of logic gates: (a) BUFFER, (b) NOT, (c) AND, (d) NAND, (e) OR, (f) NOR, (g) XOR, and (h) XNOR. 38

Figure 5: (a) Half-adder comprising XOR and AND gates. (b) Full-adder comprising two half-adders and an OR gate...38

Figure 6: A biological neuron comprises of a cell body containing the nucleus, an axon, and the axon terminal. An action potential sends an electrical impulse along the axon toward the axon terminal when the cumulative inputs from the dendrites exceed the threshold potential. 40

Figure 7: A biological neuron receives pre-synaptic input of excitatory and inhibitory nature. The signals are integrated at the axon hillock. Upon exceeding a threshold potential, an action potential is triggered. Electrical impulses travel down the axon and toward the axon terminal to other neurons. (b) An artificial neuron Nn mimics the biological counterpart by summing the product of inputs from multiple pre-synaptic inputs Im and artificial synapses

wm,n. (c) A synaptic crossbar array where programmable resistive devices represent artificial synapses at each cross-point. 42

Figure 8: (a) & (b) The step transfer function behaviour can be mimicked with STT or SOT MTJs. When $I > Ic$, the MTJ switches deterministically. (c) A step transfer function (perceptron) triggers at some threshold input Ic, also known as the critical current. 44

Figure 9: (a) The resistance state of the DW neuron MTJ scales with DW position. (b) A non-step transfer function. 45

Figure 10: (a) The resistance state of the DW neuron MTJ switches only when the domain under the PL changes between up and down states. (b) DW position and displacement due to input spikes. Green lines indicate input signal spikes that incrementally drive the DW, while the red line indicates the position of the DW. 46

Figure 11: (a) An anisotropy gradient causes the DW to drift away from the MTJ towards the region of lower anisotropy when no input current spikes are injected. (b) DW position and displacement due to input spikes. The DW moves in the opposite direction away **from** the threshold as part of the leaky feature. Green lines indicate input signal spikes that incrementally drive the DW, while the red line indicates the position of the DW. 47

Figure 12: Parallel alignment of magnetization for $Jij > 0$, and anti-parallel alignment of magnetization for $Jij < 0$. 52

Figure 13: (a) Clockwise chirality for $Dij > 0$. (b) Counter-clockwise chirality for $Dij < 0$. 53

Figure 14: Spin (blue spheres) canting in the ferromagnetic layer due to interfacial DMI from an adjacent HM atom (red sphere). 54

Figure 15: (a) Stoner-Wohlfarth particle with anisotropy axis along the xz plane. (b) $M - H$ hysteresis loops of the Stoner-Wohlfarth particle with anisotropy axis along $\varphi = 0°$ (blue), $45°$ (red), and $90°$ (black). 57

Figure 16: (a) Precession of a spin without damping. (b) Precession of a spin with non-zero damping. 59

Figure 17: (a) Pure charge current with randomly oriented spins. (b) A pure spin current has no net electronic charge flow, but a non-zero spin current flow. (c) A spin polarized current with non-zero charge and spin current flow.62

Figure 18: Representation of an electron and characteristic lengths. 63

Figure 19: Transmission line representation for (a) charge current Ic through a resistive load of length l and resistance r, and (b) two-channel model accounting for spin-up and spin-down electrons, and intermittent spin-flip conductances gsf bridging up and down spin current lines. 64

Figure 20: Charge current flow through a non-magnetic conductor leading to spin accumulation at the lateral interfaces due to the SHE. 70

Figure 21: (a) Skew scattering and (b) side-jump scattering events. 71

Figure 22: Spin accumulation at opposite interfaces of the HM/FM bilayer due to current density J. 73

Figure 23: Process flow for device fabrication from bare Si wafer to fabricated device, ready for measurement and characterization. The order may be adjusted and repeated to meet the required end result. 76

Figure 24: (a) AJA Orion sputter system. (b) Co-sputtering with two confocal and one central source within the UHV chamber. 78

Figure 25: Raith eLine electron beam lithography system. 79

Figure 26: Process for the preparation of spin-coated substrates prior to lithography. 80

Figure 27: Positive and negative tone resist after electron beam exposure and development. 81

Figure 28: AJA ion beam etching system with a secondary ion mass spectrometer (SIMS) end point detector. 82

Figure 29: (a) Directional Ar ion beam incident on a tilted and rotating water-cooled sample stage. A neutralizer eliminates charge build up on the substrate surface. (b) Active Kaufman and Robinson Ar ion source straight-on with neutralizer (bright glow on the right). 83

Figure 30: (a) Schematic of four-point probe configuration on a thin conductive layer. (b) Current injection from a probe into a thin conductive layer. 84

Figure 31: Vibrating sample magnetometer with close up illustration of vibrating sample-mounted rod between pick-up coils mounted on each pole face. 86

Figure 32: (a) Measurement set up with a Keithley 2400 series source-measure unit. (b) Schematic of device with polar θ and azimuthal φ angles of magnetization m, and polar θH and azimuthal φH angles of effective field H. I represents the flow of current along x-axis. 87

Figure 33: Exemplary plots of anomalous Hall resistance $\boldsymbol{RH}$ in a device with PMA (a) in a sweeping IP field $\boldsymbol{Hx}$, (b) and a sweeping OOP field $\boldsymbol{Hz}$....88

Figure 34: (a) Harmonic measurement set-up comprising an AC/DC source and a lock-in amplifier. (b) Device schematics with magnetization and field polar and azimuthal angles. 89

Figure 35: (a) MagVision Kerr microscopy system. (b) Kerr image of the Demagnetized state of a magnetic sample. 91

Figure 36: (a) In-plane and out-of-plane hysteresis loops obtained via vibrating sample magnetometry. Inset shows the zoomed-in out-of-plane hysteresis loop. (b) Device schematic with current delivery along the $\boldsymbol{x}$ direction, and Hall voltage measurement along the $\boldsymbol{y}$ direction. (c) Sample mount for in-situ temperature control. (d) Device coercivity from 290 K to 360 K. 94

Figure 37: a) $RH - Ich$ loops at RT (295 K), showing intermediate resistance states, and (b) in-situ Kerr microscopy images of the device magnetization configurations at various Ich corresponding to respective Hall resistances RH..96

Figure 38: (a) Current density profile across a Hall cross due to current Ich along the device channel. Lateral shunting of the current at the device junction results in an inhomogeneous current density. (b) Magnetization configuration across the device with increasing effective out-of-plane magnetic field. 97

Figure 39: (a) Thermally-assisted switching at 2.8 kOe results in monotonic decrease in switching current Isw with increasing temperature T. The change in Hall resistance ΔRH peaks at 340 K as the reduced anisotropy is unable to sustain a fully OOP magnetization above that temperature. (b) Phase diagrams across varying IP fields show ΔRH due to 1 ms write pulses across varying IP bias field Hx..98

Figure 40: (a) Schematic of measurement set-up showing heater with integrated thermocouple, and air-core coil providing an OOP magnetic field Hz. A larger electromagnet (not shown) provides an IP Hx field. (b) $RH - Hz$ loop at RT for $Hx = 0.1$ T and $Iprobe = \pm 12$ mA showing shifts in loop centers. Vertical offset is for clarity. (c) Loop shift (black dots) due to $Iprobe$. (d) Loop shifts due to bias fields of opposite polarity. Effective field χ for (e) $T = RT$ and (f) $T = 360$ K. 100

Figure 41: (a) Current-induced effective fields Hz, eff acting on chiral Néel domain walls in the absence of an external in-plane magnetic field. (b) Breaking of the DMI-induced DW chirality by applying an external magnetic field Hx. The current-induced effective field Hz, eff acts to expand and contract domains. 101

Figure 42: (a) Procedure for multistate write and read involves applying a write pulse Ich in the presence of an IP field Hx. The resistance state is probed with a non-perturbing $Iprobe = 200$ μA. The procedure is repeated with alternating polarities and amplitudes of Ich. (b) Phase diagram for multistate write and read across varying temperatures T and IP bias field Hx. 103

Figure 43: (a) and (b) Anomalous Hall resistance Rxy in a sweeping in-plane field Hx (black) and out-of-plane field Hz (red) across varying $tseed$ and $tinterlayer$. All devices show PMA with square hysteresis loops in Hz. Kerr images (i) – (iv) show the respective remanent z-magnetization state at $Hx = 0$ Oe. (c) Rxy across all devices from the OOP field sweep measurement. (d) The normalised $RxyIP$ in the $+Hx \rightarrow 0$ Oe quadrant is converted to $\cos - 1RxyIP$ to determine the device anisotropy. (e) The effective anisotropy field is then determined from the effective anisotropy energy Ku, eff shown in the integrated area shaded in grey. (e) Effective anisotropy field Hk, eff across devices with varying $tseed$ and $tinterlayer$ thicknesses. 110

Figure 44: (a) Resistances of measured devices showing monotonic decrease in resistance as $\boldsymbol{tseed}$ and $\boldsymbol{tinterlayer}$ increases. Inset shows a circuit schematic of four-resistor approximation with respective conductance Gi, where i represents the Ta adhesion layer, Pt seed layer, [Co/Pt]3/Co multilayer, and the Ta cap layer. (b) Resistivities ρ of Ta and Pt of varying thicknesses deposited on thermally oxidised Si substrate. α-Ta resistivity is shown for comparison [54]. (c) Ratio r of current through the Pt and Ta layers sandwiching the [Co/Pt]3/Co multilayer. 113

Figure 45: (a) Schematic set up for harmonic lock-in measurement of a Hall cross structure with coordinate system, where θ and φ are the polar and azimuthal angles, respectively. (b) and (d) First harmonics $V\omega$ measurements in the longitudinal and transverse schemes, respectively, (c) and (e) Second harmonics $V2\omega$ measurement in the longitudinal and transverse schemes, respectively, for the sample with $tseed = 3$ nm and $tinterlayer = 0.36$ nm. 115

Figure 46: (a) φ-dependent (θ ≈ 90°) Rxy curves fitted with equation (57) for $tseed = 2$ nm. (b) RP and (d) $\xi = RP/RA$ across all devices with $tseed$ and $tinterlayer$...117

Figure 47: Uncorrected SOT efficiencies (dashed lines) accompanied by current-density and PHE-corrected SOT efficiencies for (a) longitudinal and (b) transverse efficiencies. The corrections result in efficiencies several times larger than uncorrected values...118

Figure 48: (a) Schematic of SOT-driven logic device. (b) Cumulative anomalous Hall voltage VH across a sweeping OOP magnetic field Hx.........123

Figure 49: External field Hx, inputs $J1$ and $J2$, and corresponding anomalous Hall voltage output VH of a double Hall cross logic device..........125

Figure 50: Kerr microscopy images of the magnetization states in a double Hall cross logic device with channels spaced approximately 8 μm apart. Each Kerr microscopy image is accompanied by the corresponding interpretation of truth table using different read schemes and half- or full-rectification........127

Figure 51: (a) Schematic of SOT-driven logic device with integrated bias field line. (b) Cross section of bias field line over device channel showing locally generated field line due to a field line current IFL...129

Figure 52: Field line current IFL, inputs $J1$ and $J2$, and corresponding anomalous Hall voltage output VH of a double Hall cross logic device with integrated bias field line. 130

Figure 53: (a) Simulation device dimensions. (b) Cross-section of simulated device. (c) Model of simulated device showing parallel current flow across layers with different resistances and resistivities. 131

Figure 54: (a) The SHE circuit is represented by charge and spin circuits with respective conductance [24]. The charge circuit between terminals 1c and 2c contains a series conductance $G0$ and two current sources $I0c$ which represent spin-to-charge conversion via the SHE. The spin circuit between terminals 3y and 4y consists of a series conductance $G2y$, shunt conductances $G1y$ which represent spin current attenuation via spin-flip processes, and current sources $I0y$ which represent charge-to-spin conversion by the SHE. (b) Capacitor-current source circuits which represent the LLG equation. Magnetization components mx, my and mz are represented as node voltages. (c) Voltage source circuit representation of the AHE where $VAHE \propto IcMz$. Modular representations of the SHE, LLG, and AHE are shown under their respective circuit representations [23]. (d) Compact model of our multilayer Hall cross device. The HM layers are modelled using SHE modules while the FM layer is modelled using an LLG module and resistance RFM. The AHE module accepts mz from the LLG module and the current flowing through the FM layer Ic as inputs and outputs a transverse voltage VAHE. The correlation between the compact model to the symbolic representation is shown in blue dashed lines. Black arrows represent the magnetization state of the Hall cross, where an ↑ indicates $mz > 0$ and ↓ indicates $mz < 0$. (e) Design of half-adder circuit using two logic devices. Devices 1 and 2 have magnetization configurations and rectification circuits that yield the logical outputs of an XOR and AND gate respectively. Current sources

are wired to the devices such that input current pulses can be delivered to both devices simultaneously. (f) Demonstration of half-adder functionality. 132

Figure 55: (a) Stochastic readout of a probabilistic bit across varying bias voltages over 100 ms sample time. (b) Average magnetization over 100 ms across a range of bias voltage. 140

Figure 56: Schematic of a Hall cross structure. 141

Figure 57: (a) Current-capacitor circuit for the LLGS module. (b) Voltage source for the effective fields. (c) Current source for the spin currents. 159

Figure 58: (a) Spin current along the $+\boldsymbol{x}$ direction and polarised spins accumulating along the $\boldsymbol{x}$-$\boldsymbol{y}$ and $\boldsymbol{x}$-$\boldsymbol{z}$ surfaces. (b) Terminals for each side of the NM block. 160

Figure 59: Circuit representation of charge current flowing across terminals *1c* and *2c*. 164

Figure 60: Circuit representation of $\boldsymbol{x}$ and $\boldsymbol{y}$ polarized spin current flow with respective spin flip conductance for spin attenuation. 166

Figure 61: (a) Magnetization components mX, my, and mz over 3 ns due to an in-plane magnetic field Hx. (b) Magnetization trajectory of the magnetization m. 167

Figure 62: (a) In-plane field Hx (black) and pulse current I (pink) applied to the SPICE model. (b) Magnetization components across 10 ns due to Hx and I. 168

Figure 63: An 8-neuron (node) Hopfield network. The red line represents the synaptic weight $w1,2$ between neurons 1 and 2. 170

Figure 64: Learning the letter N and converting the white and black pixels to -1 and $+1$, respectively 171

Figure 65: (a) Histogram of weights across 300 synapses for a 5-by-5 array pixel after learning the letters N, T, and U. (b) Individually addressed synapses and their respective weights. 172

Figure 66: (a) A substrate with 20 devices wire bonded on to a CCL board. (b) A PCB cartridge with mounted CCL board and soldered discrete electronic components and IC chips. 173

Figure 67: Schematic of SOT device array with controllers. 173

Figure 68: Arduino, main multiplexer, and single cartridge set-up. ...174

Figure 69: (a) $I - RH$ hysteresis for Device #0 with linear region indicated by dashed lines for corresponding range of I and RH. (b) $I - RH$ hysteresis loops for the first ten devices: #0 thru #9. 174

Figure 70: Histogram of RH frequency for current range $14 \text{ mA} \leq I \leq 20 \text{ mA}$...175

Figure 71: Resolving 5-by-5 pixel characters "N", "T", and "U" from noisy or distorted inputs..176

List of Tables

Table 1: Comparison of conventional and emerging solid-state memory technologies. 31

Table 2: Comparison table of $HDMI$ values obtained from similar measurement methods. Values of $HDMI$ obtained in this and other works using similar measurement methods of determining χ. 102

Table 3: Differentiation of operating modes. 126

Table 4: Material parameters used in SPICE for the HM Pt and Ta. . 134

Table 5: Magnetic parameters used in SPICE for the ferromagnetic multilayer. 134

Acronyms

AC	Alternating Current
AHE	Anomalous Hall Effect
AFM	Anti-Ferromagnet
AMR	Anisotropic Magnetoresistance
ANE	Anomalous Nernst Effect
AP	Anti-Parallel
ASL	All-spin Logic
CMOS	Complementary Metal-Oxide-Semiconductor
CIP	Current-in-Plane
CPP	Current Perpendicular to Plane
CPU	Central Processing Unit
DC	Direct Current
DMI	Dzyaloshinskii-Moriya Interaction
DOS	Density of States
DSP	Digital Signal Processor
DW	Domain Wall
DWM	Domain Wall Motion
DRAM	Dynamic Random Access Memory
EB	Exchange Bias
EBL	Electron Beam Lithography
FFT	Fast Fourier Transform
FI	Ferromagnetic Insulator
FL	Free Layer
FM	Ferromagnet
FMR	Ferromagnetic Resonance
GDS	Graphic Design/Database System
GMR	Giant Magnetoresistance
GPIB	General Purpose Interface Bus
HDD	Hard Disk Drive

HM	Heavy Metal
IBE	Ion Beam Etching
ICP	Inductively Coupled Plasma
IL	Insulator Layer
IMA	In-Plane Magnetic Anisotropy
IPA	Isopropyl Alcohol (C3H8O)
IrMn	Iridium Manganese (IrMn3)
LLG	Landau-Lifshitz-Gilbert
ME	Magnetoelectric
MIBK	Methyl Isobutyl Ketone
MOKE	Magneto-Optic Kerr Effect
MRAM	Magnetoresistive Random Access Memory
MTJ	Magnetic Tunnel Junction
NLSV	Non-Local Spin Valve
NM	Non-Magnetic/Normal Metal
OFHC	Oxygen-Free High Conductivity
OHE	Ordinary Hall Effect
P	Parallel
PHE	Planar Hall Effect
PL	Pinned Layer
PMA	Perpendicular Magnetic Anisotropy
PMMA	Poly(Methyl Methacrylate)
pMTJ	Perpendicular Magnetic Anisotropy MTJ
PVD	Physical Vapour Deposition
RAM	Random Access Memory
RE	Rare Earth
RF	Radio Frequency
RF-ICP	Radio Frequency Inductively Coupled Plasma
SAF	Synthetic Antiferromagnet
SHE	Spin Hall Effect
SIMS-EPD	Secondary Ion Mass Spectrometer End Point Detector

SMR	Spin Hall Magnetoresistance
SMU	Source Measure Unit
SNR	Signal-to-Noise Ratio
SOC	Spin-Orbit Coupling
SOI	Spin-Orbit Interaction
SOT	Spin-Orbit Torque
SRAM	Static Random Access Memory
SSD	Solid State Drive
STT	Spin-Transfer Torque
TMR	Tunnelling Magnetoresistance
USB	Universal Serial Bus
UV	Ultraviolet
UVL	Ultraviolet Lithography
VCMA	Voltage-Controlled Magnetic Anisotropy

Chapter 1

Introduction

Modern electronic memory and computing devices make use of charge and charge states to store, process, and transmit data. These technologies have seen significant progress over the decades that have led to faster clock rates, greater memory density, lower latency, and shrinking cost per bit. This was enabled by numerous innovations in integrated circuit design, more advanced lithography, denser interconnects, and overall semiconductor and transistor technology. The memory-storage hierarchy shown in **Figure 1** compares the different memory technologies, and their implementation in today's computer systems. Closer to the base of the pyramid are non-volatile and slower memory, while the faster, volatile memories are closer towards the peak of the pyramid. HDDs can store a lot of data, are cost effective, and have been a mainstay for data storage medium for decades. However, they have higher power draw and are slower relative to SSDs which have seen greater adoption due to their high speed and non-mechanical operation. SSDs and HDDs make up the class of non-volatile memories, in which the data stored does not get lost when power is removed. Unlike HDDs that rely on spinning magnetic platters, SSDs utilize solid-state memory in the form of NAND Flash. On the other hand, volatile memory such as RAM store data in capacitors that slowly leak electric charge and requires power to maintain charge states that represent the data. Dynamic RAMs (DRAM) and static RAMs (SRAM) are two main variants. Due to their multiplexing and demultiplexing circuitry (random access), they are very fast and typically used to store large chunks of data temporarily. Finally, CPU cache and registers at the top of the memory hierarchy pyramid represent the fastest memory and are located close to the processor core [1].

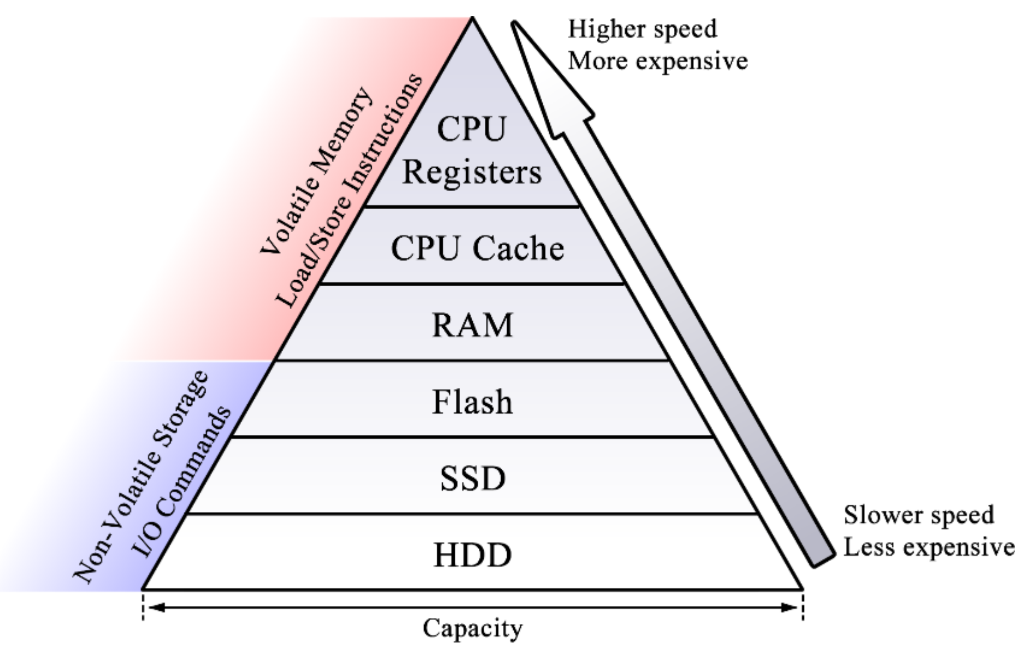

Figure 1: Memory-storage hierarchy showing different classes of memory based on their response time, capacity, and complexity.

Calculations are performed on processors, and today's CPUs come with multiple cores, multi-threading, and technologies to reduce latency and increase throughput in a bid to improve overall computing performance. This is particularly important as computers take on more compute-intensive tasks such as weather forecasting, cryptography, and physical simulations. Demand for greater computational performance with lower power dissipation and smaller footprint have driven transistor count and packing density to double almost every two years [2]. This trend was described by Gordon Moore, and this observation is now referred to as Moore's law. While not an actual physical law, it has been used to aid in the projection of technological progress. However, the momentum is not expected to keep pace indefinitely, as the physical limit of transistor scaling are fast approaching. Furthermore, there has been a stagnation in processor operating frequency due to heat dissipation and thermal management [3-5]. This has necessitated and stimulated research on alternative approaches to circumvent the challenges brought about by transistor scaling limits [6]. The International Technology Roadmap for Semiconductors (ITRS) and its successor, the

International Roadmap for Devices and Systems (IRDS), have been predicting the technological development, potential roadblocks and challenges, and finding solutions. The IRDS, comprising experts from various fields, also coordinates efforts between the industry, research bodies, academia, and equipment suppliers to circumvent or overcome these challenges. Research on several potential beyond-CMOS technologies are being actively pursued [6]. One approach is to develop technologies that can complement or replace CMOS such as in spin-based devices, or spintronics – a neologism describing spin transport electronics. In this thesis, we explore the optimization and design of Co/Pt thin film multilayer-based multistate memory and logic devices. Table 1 compares certain performance parameters between convention and emerging solid-state memories [7-9]. Volatility, large cell size, long read and write time, high power dissipation, and poor (low) endurance are some of the undesirable characteristics present in conventional memory technologies.

Parameter	Conventional Memory Technology			Emerging Memory Technology	
	SRAM	DRAM	NAND Flash	STT-MRAM	SOT-MRAM
Volatility	No	No	Yes	Yes	Yes
Cell Size (F^2)	50 – 120	6 – 10	5	6 – 20	6 – 20
Read Time (ns)	≤ 2	30	10^3	1 – 20	≤ 10
Write Time (ns)	≤ 2	50	10^6	~ 10	≤ 10
Write Power	Low	Low	High	Low	Low
Endurance (Cycles)	> 10^{15}	> 10^{15}	10^5	> 10^{15}	> 10^{15}

Table 1: Comparison of conventional and emerging solid-state memory technologies.

1.1 Objective of this Thesis

This thesis aims to enable the development of spin-orbit torque driven spintronic multi-state memory and logic devices using Co/Pt thin film multilayer with perpendicular magnetic anisotropy, with potential applications in beyond-CMOS logic and computation-in-memory. As such, the objectives are driven

towards the characterization of the thin film multilayer to optimize the spin-orbit torque efficiency, structure design for multistate characteristics and logic functionality. The main objectives of this thesis are as follows:

i) Due to the HM/FM multilayer, SOT contribution from differing HM thicknesses will affect the current-induced magnetization switching efficiency of devices. Therefore, the characterization and optimization of Co/Pt thin film multilayers using the adiabatic harmonic Hall measurement technique across varying interlayer and seed Pt thicknesses is studied.

ii) The binary state of MTJ devices are used in the form of non-volatile random-access memory such as MRAM. Storing more than one bit of data in a single magnetic memory cell can improve data storage density. Thus, the development of a multistate memory device based on the Co/Pt multilayer, as well as the effective SOT out-of-plane field due to operation under elevated device temperatures are studied and discussed.

iii) Aside from memory storage, spintronic devices are also promising candidates for logic and computation-in-memory. Using a perpendicularly magnetized Co/Pt multilayer, a reconfigurable logic device with an integrated bias field line is developed. Half-adder functionality is further demonstrated using SPICE modeling.

The work is thus organised as follows:

Chapter 2 introduces spintronic devices with applications to logic. As computation is evolving beyond traditional von Neumann architecture and as a potential application for spintronic multistate memory devices, spintronic devices for neuromorphic engineering will be discussed.

Chapter 3 discusses the fundamentals of magnetism and spintronic physics which will be utilized throughout the thesis chapters.

Chapter 4 describes the experimental techniques employed in this thesis. Device fabrication is achieved through thin film sputtering, electron beam lithography, and ion beam etching. The blanket thin films and devices are then characterized through various magnetic and electrical means.

Chapter 5 presents the development of a Co/Pt thin film multilayer device with multistate characteristics, its switching behaviour and changes to the effective out-of-plane field due to spin-orbit torque at elevated temperatures.

Chapter 6 presents the results on the effect of interlayer and seed Pt in Co/Pt thin film multilayers on spin-orbit torque efficiency using the adiabatic harmonic Hall measurement technique.

Chapter 7 presents the development of a Co/Pt multilayer-based logic device with on-chip reconfigurability due to the integrated bias field line, and SPICE modelling of the device for expansion to half-adder functionality.

Chapter 8 summarizes the work and proposes future works to pursue, discussing strategies to improve current-induced magnetization switching efficiencies and new spintronic approaches to computation.

Chapter 2
Spintronic Devices

Alongside its charge properties, an electron also possesses an intrinsic spin associated with its magnetic moment. The first observations of spin-related phenomena can be dated back to 1857, when Lord Kelvin observed that a charge current flowing through Fe and Ni was influenced by magnetism [10]. We now attribute his observations to anisotropic magnetoresistance (AMR), which is the dependence of electrical resistance on the angle between the magnetization and charge current directions. Subsequently in 1929, electronic spin-dependent transport was described by Mott [11]. By then, the concept of a magnetic moment in electrons was already hypothesized to account for duplexity in atomic spectra, through the Stern-Gerlach experiment, and on newly established theory on the magnetic moment in electrons. The recent decades saw the advancement of thin film processing technology that enabled the growth of monolayers and multi-layered devices with contiguous interfaces using molecular beam epitaxy (MBE) and sputtering techniques. In 1975, Julliere demonstrated spin-dependent tunnelling through a semiconductor in a Fe/Ge/Co multilayer, demonstrating 10 % change in resistance at 4.2 K [12]. In 1988, GMR was discovered independently by Albert Fert and Peter Grünberg in FM/NM/FM multilayers which earned them the 2007 Nobel Prize in Physics [13,14]. It was discovered that by replacing the NM layer with a thin dielectric barrier such as Al_2O_3, a change of resistance up to 70 % at room temperature was observed [15,16]. With an MgO barrier in place of the Al_2O_3 barrier layer, Parkin and Yuasa achieved up to 220 % TMR [17,18]. As the electrons are required to tunnel through the oxide barrier, this process is a quantum mechanical phenomenon. Fast-forward to today, spintronic devices see industrial and commercial applications, especially in data storage technology. The HDDs of today make use of TMR in MTJs in read heads.

New materials and device physics, with applications such as in solid-state spintronic memory, in-memory and neuromorphic computation continue to drive research in this field.

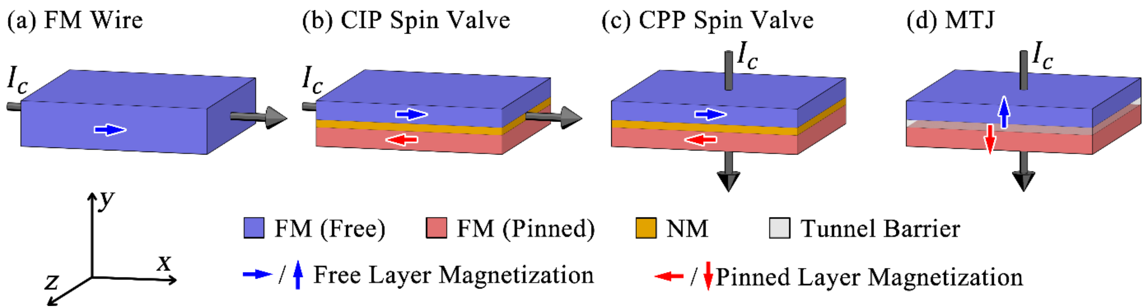

Figure 2: (a) Ferromagnetic wire. (b) Current-in-plane spin valve. (c) Current-perpendicular-to-plane spin valve. (d) Magnetic tunnel junction. Black arrows indicate the flow of current I_c. Red and blue arrows indicate pinned and free magnetic layers, respectively.

Several examples of spintronic devices are illustrated in **Figure 2** (a) to (d). Functional spintronic devices can be formed from simple FM wires, in which the magnetization can be manipulated using an external magnetic field or by current-induced spin transfer torque. In such nanowire devices, information is represented by DWs, and the DW position along the wire can be manipulated by field and current-induced torques [19,20]. When two FM layers sandwich a NM layer such as Cu, the structure is referred to as a spin-valve (SV) [21]. In an SV, one of the FM layers known as the pinned layer serves as a reference. The pinned layer has a larger anisotropy and coercivity as compared to the FL [21]. This makes the FL relatively easier to flip as it is used to store the data bit. To read the magnetization state, a small probing current is passed through the device. For a current-in-plane (CIP) SV, the charge current flows along the film plane, while in a current-perpendicular-to-plane (CPP) SV, the charge current runs through the heterostructure. Spin-dependent electron scattering occurs due to the differing density of states (DOS) between up and down spins in oppositely oriented pinned and free FM layers. If the NM layer is replaced with a tunnel barrier layer, the structure is known as an MTJ. The parallel (P) and anti-parallel (AP)

magnetization states result in low and high TMR, respectively [22]. MTJs form the basis of modern-day HDD read heads as well as a relatively new type of non-volatile memory known as magnetic random-access memory (MRAM). The first generation of MRAM devices used current-induced local magnetic fields from orthogonal write lines to switch the magnetization state of specific cells, as shown in **Figure 3** (a). While the technique was extremely simple, it imposed limitations to device scaling. Subsequently, new techniques of magnetization switching such as thermal assisted switching (TAS), spin-transfer torque (STT), SOT, and domain wall (DW) propagation were developed and proposed, as illustrated in **Figure 3** (b) to (e), respectively. In TAS devices, localised generation of Joule heat is used to reduce the MTJ FL coercivity, to assist in the magnetization switching [23]. As the current through the MTJ also provides a means of STT, the field line can be removed in order to improve the device scalability. The STT-MRAM technology is mature enough to be a commercially viable non-volatile memory storage device. However, the ultrathin tunnel barrier for a low resistance-area product, and challenges posed by the read and write current sharing the same path (read-write disturb), has led to the search for alternative means of current-induced magnetization switching techniques. The SOT-driven MTJ allows for separate read and write current paths at the expense of additional transistors [24-27]. These SOT-driven devices generate polarised spin currents by passing charge current through a HM with large SOC sharing a contiguous interface with the FM FL [28]. With the use of FM layers with PMA, the spintronic memory cells can be scaled to smaller dimensions. However, large FM layers that can harbour magnetic domains can serve niche roles that require analogue-like behaviour or thresholding features.

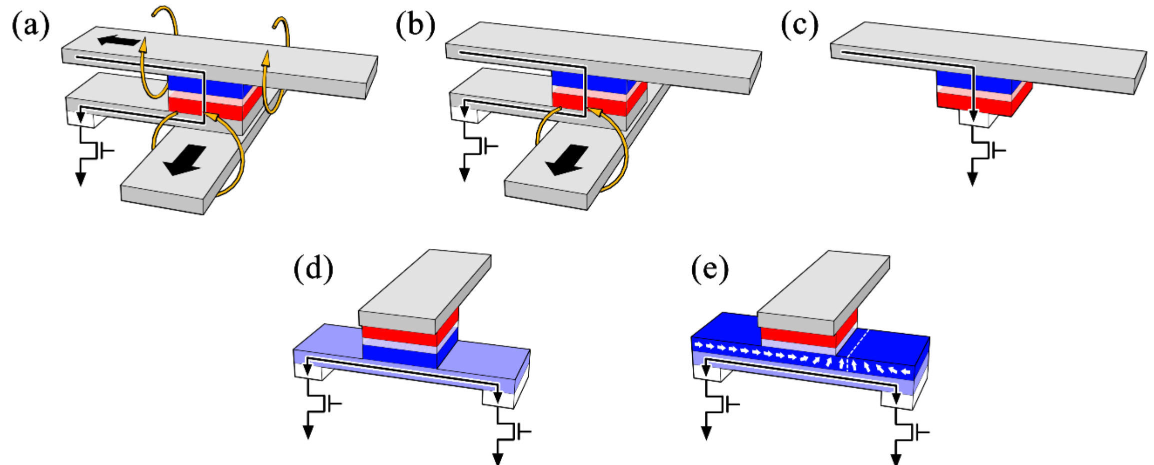

Figure 3: (a) Toggle MTJ. (b) Thermally-assisted MTJ. (c) STT-MTJ. (d) SOT-MTJ. (e) DW-MTJ. Device resistance states are probed by a read current represented by a thin black arrow through the MTJ stack. Bold black arrows indicate write line current for field-induced magnetization switching of toggle and thermally-assisted MTJs.

Spintronic devices are not limited to memory applications. Research has been ongoing for spintronic devices applied to compute-in-memory and logic-in-memory architectures. Furthermore, non-von Neumann approaches to computation such as brain-inspired computing or neuromorphic computation [29,30], and probabilistic computation promise even greater performance metrics [31-34].

2.1 Spintronics for Logic Applications

Aside from memory storage, spintronic devices are also potential candidates for computing-in-memory. In the following sections, we look at how spintronic devices can function in logic and neuromorphic applications.

Conventional computers perform arithmetic and other complex operations using circuits comprising Boolean logic gates. These logic gates compare one or more binary input signals and produce a binary output, and areshown in their distinctive symbols in **Figure 4** (a) to (h). Single-input logic gates include the BUFFER and NOT gates. The BUFFER gate simply passes on the input logic unchanged, while the NOT gate inverts the input logic and is also

referred to as the inverter. The AND, OR, and XOR gates compare two inputs, and their inverted counterparts are NAND, NOR, and XNOR, respectively.

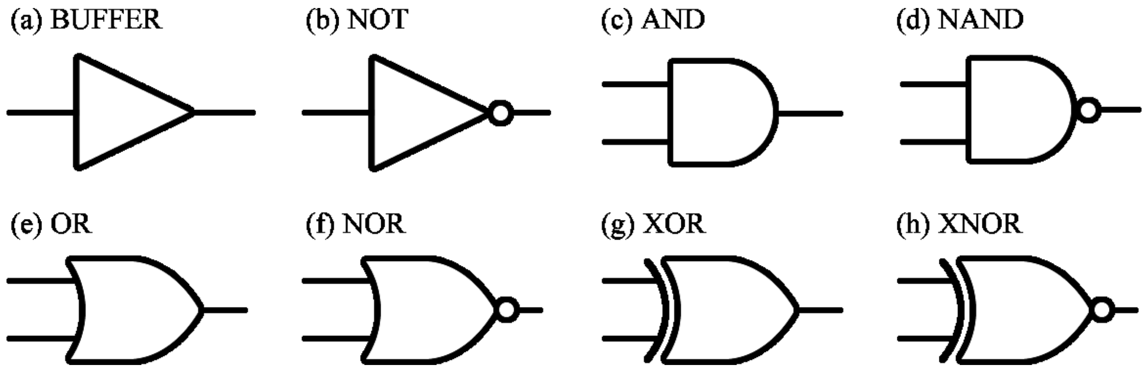

Figure 4: Distinctive symbols of logic gates: (a) BUFFER, (b) NOT, (c) AND, (d) NAND, (e) OR, (f) NOR, (g) XOR, and (h) XNOR.

Logic gates can be used to construct circuits that can perform basic arithmetic functions. The half-adder schematic illustrated in **Figure 5** (a) can be constructed out of an XOR and an AND logic gate, and takes in two single binary digits and sums them. The outputs SUM from the XOR gate and the CARRY from the AND gate depend on the combination of inputs A and B. A signal from the CARRY output indicates an overflow, which can be fed into subsequent adder circuits.

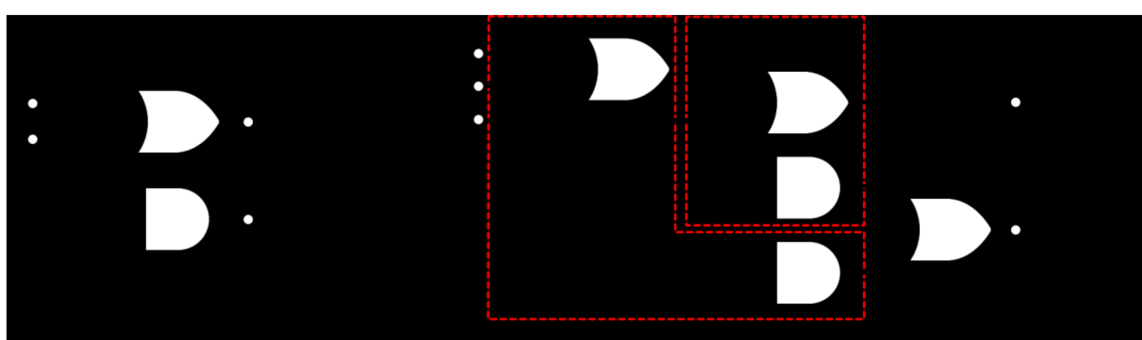

Figure 5: (a) Half-adder comprising XOR and AND gates. (b) Full-adder comprising two half-adders and an OR gate.

A full-adder as illustrated in **Figure 5** (b) performs addition on binary numbers, and also accepts CARRY IN values from a previous overflow. A one-bit full-adder can be constructed out of two half-adders indicated in red dashed

outlines. Multi-bit adders are simply concatenated one-bit adders. Such adder circuits are constructed out of transistor-based logic circuits, and the outputs persist while the input signals are present.

Spintronic devices have been proposed, demonstrated, and continue to be extensively studied due to their potential as logic-in-memory devices. The advantage of spintronic-based logic devices is in its non-volatility and low power operation. Examples of spintronic logic devices include all-spin logic (ASL) using non-local spin valves (NLSV) [35-40], domain wall (DW) logic [41-44], nano-magnetic logic [45-50], and MTJ-based logic [51-54]. Due to the persistent magnetization states in spintronic logic devices, memory and logic are unified, alleviating the von Neumann bottleneck. In addition, spintronic logic boasts high switching speed and endurance, giving it a competitive advantage and potential for logic-in-memory applications. This thesis explores the reconfigurable SOT-driven logic device in Chapter 6, and how it is implemented to perform half-adder functionality.

2.2 Spintronics for Neuromorphic Engineering

When compared to the von Neumann architecture in computers, the biological brain operates through massively parallel processing, consumes much less power (~20 W), is extremely plastic and reconfigurable, and co-locates processing with memory [55]. Furthermore, the human brain learns using a small range of examples and over the course of his/her lifetime, while computers require a relatively larger and more comprehensive dataset. This has led to the field of neuromorphic computing, first conceived by Carver Mead while at Caltech [56]. In neuromorphic computing and engineering, humans try to describe the various mechanisms of the biological brain using brain-inspired models, in hopes of developing faster and more efficient computation systems. This degree of likeness of the brain-inspired model is termed bio-fidelity.

The brain comprises of the nervous system, primarily composed of ~10^{11} neurons which are specialised cells that manage the transmission of nerve impulses as depicted in **Figure 6** [57]. Neurons communicate by sending neurotransmitters across a ~20 nm gap known as the synaptic cleft [58], of which there are about ~10^{15} [57]. The conveyance of information pertaining to sensory input, motor control, and cognition are due to interactions between different types of neurons. A typical neuron comprises of several distinct sections: (i) The metabolic centre of the neuron known as the soma (cell body), (ii) dendrites which extend from the cell body and receive information impulses from pre-synaptic neurons, (iii) the axon which conducts electrical impulses away from the soma toward the axon terminal, and (iv) the axon terminal which contains synaptic vesicles that hold neurotransmitters, which are released across the synapse to post-synaptic neurons.

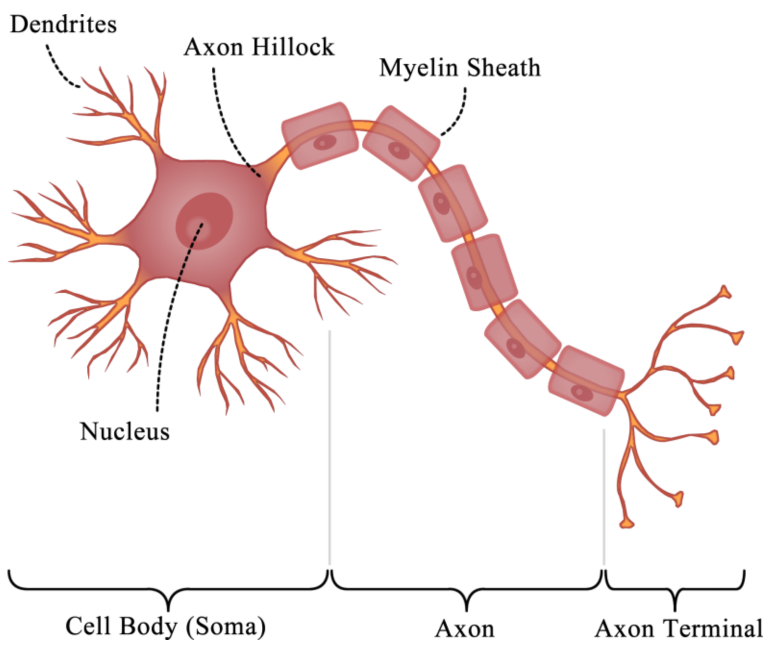

Figure 6: A biological neuron comprises of a cell body containing the nucleus, an axon, and the axon terminal. An action potential sends an electrical impulse along the axon toward the axon terminal when the cumulative inputs from the dendrites exceed the threshold potential.

The input received at the dendrites come from many other neurons and can either be excitatory or inhibitory. The inputs contribute to an analogue voltage

signal called the membrane potential. The axon hillock operates on an all-or-none law that sums all the input signals and triggers an action potential when a threshold potential is breached. When sufficient excitatory input exceeds the potential threshold, an action potential will propagate along the axon to the axon terminals. Aside from the analogue and digital mechanisms found within the brain, there are also dynamic, time-dependent features. For example, in the spike-timing-dependent plasticity (STDP) process, the synaptic strength between neurons is adjusted based on the relative timing between pre- and post-synaptic activity. Neuron behaviour varies vastly depending on their type and function [59]. In designing an artificial neuron/synapse, there is a trade-off between device complexity, computational power efficiency, and bio-fidelity.

Most of the ongoing research work in artificial neural networks and machine learning is through a top-down approach of developing algorithms to mimic biological neural processes while still relying on hardware based on mature CMOS technologies. Several takes on artificial neurons, synapses, and neural network hardware using conventional transistors include the IBM TrueNorth and Intel Loihi chips. Such chips attempt to emulate biological neuronal and synaptic behaviour using transistors, but not necessarily capture the same bio-fidelity of actual biological neurons and synapses. However, properties and characteristics unique to emerging technologies such as spintronics enable a bottom-up approach in the development of brain-inspired computational hardware with greater bio-fidelity. In this section, we look at various spintronic devices and discuss how they can be used to mimic behaviours, mechanisms, and features of the biological brain, as well as in building functional features, efficient computational primitives, and circuits for real world applications.

2.2.1 Spintronic Synapses

The biological neuron receives excitatory and inhibitory post-synaptic potentials along dendrites as shown in **Figure 7** (a). The plasticity of the synapse

is what leads to learning and memory as described by Hebb's postulate, in which the relationship between neurons depend on the pre-synaptic and post-synaptic activity [60]. The summation of the input potentials can ultimately lead towards generating an action potential. In an artificial neural network, synapses with synaptic weights $w_{m,n}$ determine the connection strengths between the pre- and post-synaptic neurons. The post-synaptic neuron N_n receives inputs I_m from pre-synaptic neurons as shown in **Figure 7** (b), such that $N_n = \sum I_m w_{m,n}$. An equivalent circuit in the form of a synaptic crossbar array is shown in **Figure 7** (c). In the crossbar array, a programmable device with memristive or analogue-like behaviour is used to encode the synaptic weight at each cross-point. The output at each neuron is then the sum of dot products between voltage inputs and synaptic conductance.

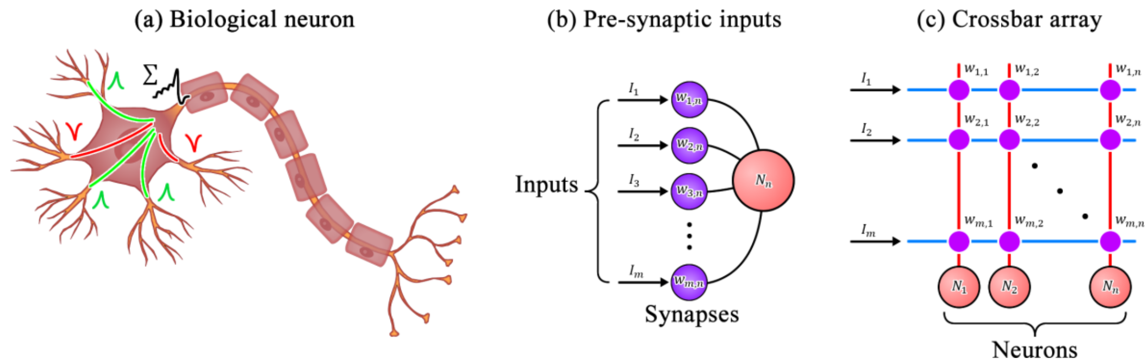

Figure 7: A biological neuron receives pre-synaptic input of excitatory and inhibitory nature. The signals are integrated at the axon hillock. Upon exceeding a threshold potential, an action potential is triggered. Electrical impulses travel down the axon and toward the axon terminal to other neurons. (b) An artificial neuron N_n mimics the biological counterpart by summing the product of inputs from multiple pre-synaptic inputs I_m and artificial synapses $w_{m,n}$. (c) A synaptic crossbar array where programmable resistive devices represent artificial synapses at each cross-point.

The ability to adjust the strength between neurons can be used to reflect the correlation between pre- and post-synaptic neurons is called the synaptic plasticity. Several approaches using spintronic devices to function as artificial synapses are possible, either through the manipulation of relative sizes of

magnetic domains such as in DW or skyrmions in the device, or by time averaging of a biased stochastic magnetic cell [61-66].

MTJs have been available commercially in the form of MRAM, where a single bit is deterministically switched to store binary data. The reliability of such a memory element is only possible using precise fabrication processes. However, it has also been shown that "misbehaving" MTJs that do not switch deterministically, but rather, stochastically may also find purpose in neuromorphic engineering. An MTJ operating in the stochastic regime may switch up or down 50% of the time. Using this switching distribution, multiple MTJs with this quality can jointly function as a single synapse and demonstrate analogue-like behaviour [67].

In a DW MTJ, the TMR corresponds with DW position, and the DW position can be manipulated by current-induced spin torques [63,68]. Alternatively, synaptic weights can be represented by anomalous Hall voltage states in a Hall cross device with memristive or analogue-like behaviour due to the magnetization polarization of the material as well as spin-orbit coupling [69,70]. These spintronic synapses contain the weights in the form of non-volatile magnetization states and can be adjusted through an iterative learning process by updating the device magnetization states.

2.2.2 Spintronic Neurons

Spintronic neurons come with various functionalities and characteristics, and range in behavioural complexity. The output of spintronic neurons can be described by their likeness to their biological counterpart, or bio-fidelity. In its simplest form, stepwise neurons with binary output can be achieved with commercially available MTJs [71]. However, one may require non-step transfer functions in order to handle non-binary inputs and outputs. For both step and non-step neurons, the magnetization dynamics and time-domain are not considered. We know that the biological brain does indeed have time-dependence behaviour,

therefore, spintronic neurons with features such as in leaky-integrate-and-fire (LIF), or simply IF if no leaky feature is present, as well as stochasticity would emulate biological neurons more closely. The various spintronic neuronal behaviours are discussed in increasing bio-fidelity.

The simplest neuronal response is that of a perceptron with a step transfer function as shown in **Figure 8** (a). The most common spintronic device with such a response is the MTJ as shown in **Figure 8** (b) and (c), which switches between high and low resistance states via STT or SOT when the input $I > I_c$. The resistance states can be deterministically switched when the critical switching current I_c is exceeded, aligning the magnetization in the free and reference layers between parallel and anti-parallel orientations. For STT-MTJs, this requires a voltage bias through the tunnel junction. Such a switching mechanism has several drawbacks: i) As the read and write current paths are shared, there is a tendency for unintentional switching due to read disturb. ii) The high voltage bias required affects the device endurance and is not energy efficient as compared to other switching mechanisms. As such, SOT is a more energy-efficient means of magnetization switching, at the expense of an additional terminal that results in separate read and write current paths. For such spintronic step-transfer function neurons, the MTJ can be extremely small such that only a mono-domain magnetization in the FL exists. The magnetization dynamics are neglected for a more simplistic binary output behaviour for such an artificial neuron.

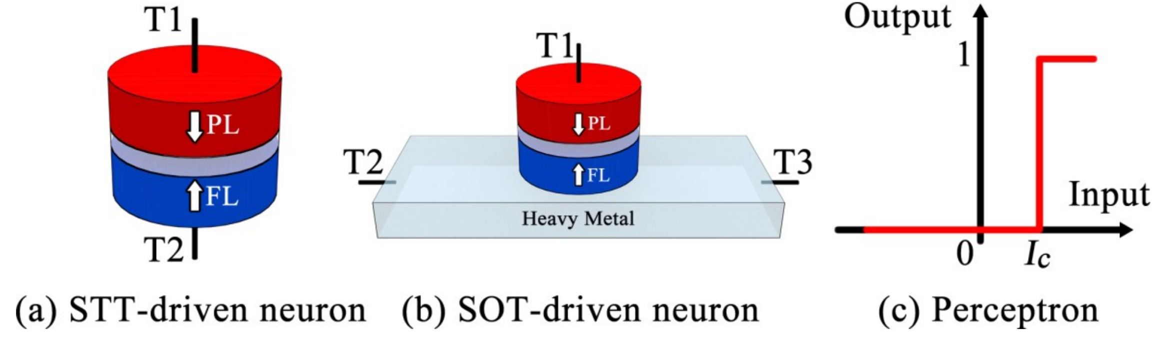

Figure 8: (a) & (b) The step transfer function behaviour can be mimicked with STT or SOT MTJs. When $I > I_c$, the MTJ switches deterministically. (c) A step

transfer function (perceptron) triggers at some threshold input I_c, also known as the critical current.

The transfer function that models a neuronal output is typically non-stepwise such as in **Figure 9** (a). In artificial neural networks, common transfer or activation functions include the sigmoid, hyperbolic tangent, or more popularly, the rectified linear unit (ReLU). To achieve beyond binary states in spintronic neuron devices, one would require multi-domain formation in the FL. Rather than existing as either one of two possible magnetization states, a multi-domain FL may form two oppositely magnetized domains separated by a DW. The relative proportions between domains can be adjusted by manipulating the DW position allowing for multiple resistance states to be exhibited in a DW neuron MTJ [62,72,73]. The DW position can be manipulated by current-induced SOT, and the resistance state of the device can be read out using an MTJ [74]. The divider circuit in **Figure 9** (b) operates such that an increase in parallel orientation of the FL domain leads to lower resistance of the DW neuron MTJ. This drives the output transistor to approximately match I_{out} and I_{in} linearly.

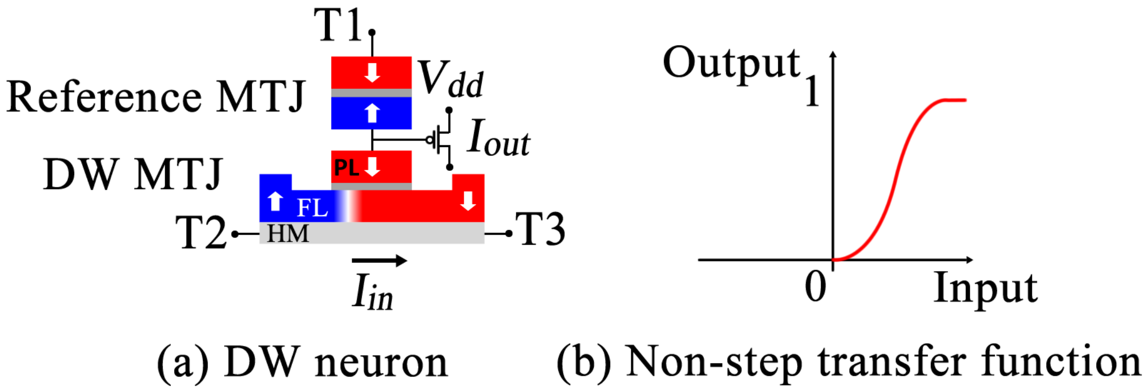

Figure 9: (a) The resistance state of the DW neuron MTJ scales with DW position. (b) A non-step transfer function.

The biological neuron receives multiple inputs from multiple unsynchronised pre-synaptic neurons. The excitatory and inhibitory inputs may not be received all at the same time, but across a span of time. These multiple

inputs trigger the neuron when a threshold is reached and describes the IF functionality. Consider a similar structure to the non-step neuron discussed earlier, with multiple short injected current pulses to move the DW across the device, as depicted in **Figure 10** (a). At a certain point, the DW would have crossed a threshold position such that the resistance state of the neuron MTJ would cause the output inverter to be triggered as shown in **Figure 10** (b). The IF functionality therefore describes the biological brain's ability to summate all inputs over time and trigger the neuron when the threshold potential is reached. However, it does not address the potential decay as observed in biological systems, which further adds time-dependence to the input stimulus.

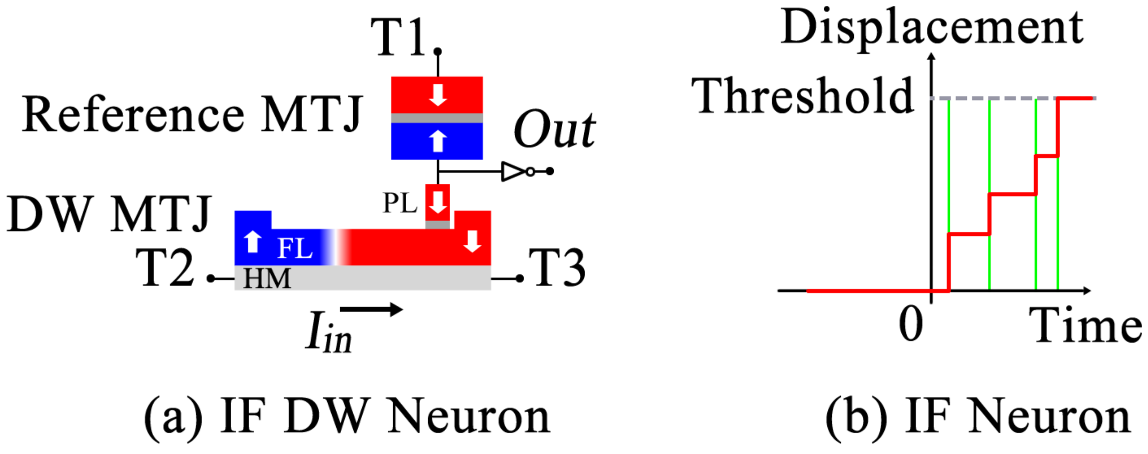

Figure 10: (a) The resistance state of the DW neuron MTJ switches only when the domain under the PL changes between up and down states. (b) DW position and displacement due to input spikes. Green lines indicate input signal spikes that incrementally drive the DW, while the red line indicates the position of the DW.

In the LIF functionality, consecutive inputs are not only summed over time, but the relative interval between inputs is also considered [75,76]. Sparsely timed excitatory inputs may fail to trigger the neuron as the individually-triggered potential spikes decay over time, while closely timed excitatory inputs allow for successive integrations to exceed the threshold. **Figure 11** (b) shows input spikes (green lines) spaced close enough in time such that the DW is successfully displaced towards the threshold. If the input spikes were timed more sparsely, the DW may require more input spikes or even fail to cross the threshold. The leaky

feature can be achieved by the simple implementation of a clocked current pulse in the opposite direction that drives the DW backwards. Alternatively, the DW can be allowed to naturally drift to leak without external stimuli by patterning a trapezoidal length of magnetic material, in which the DW would tend towards the narrower edge with lower DW energy [74,77,78]. In a similar energy-driven approach, the magnetic thin film can be grown such that the anisotropy is graded along the length within which the DW propagates as shown in **Figure 11** (a) [79]. The DW will drift towards the region of lower anisotropy in the absence of external stimuli. Similarly, skyrmions have been proposed to deliver LIF neuron functionality [75].

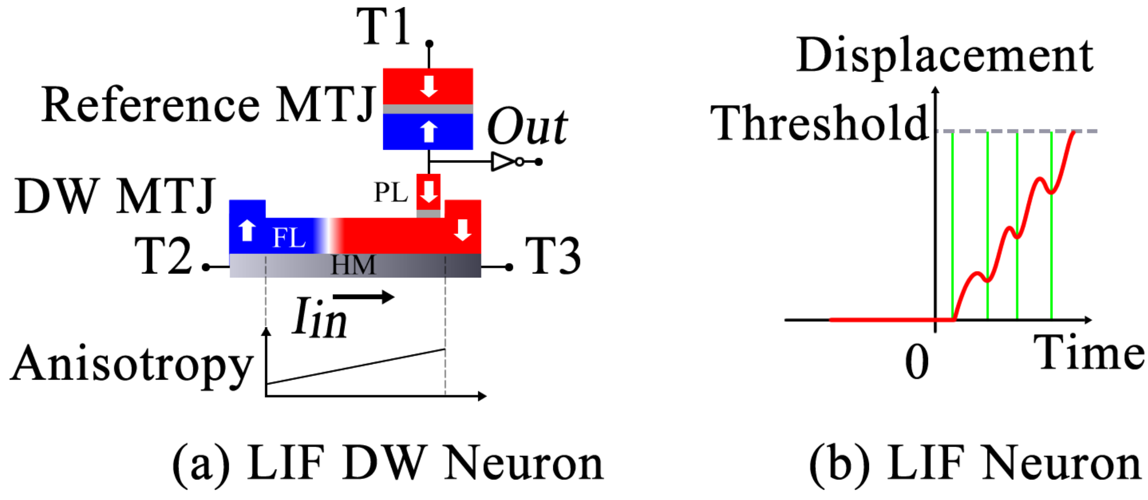

Figure 11: (a) An anisotropy gradient causes the DW to drift away from the MTJ towards the region of lower anisotropy when no input current spikes are injected. (b) DW position and displacement due to input spikes. The DW moves in the opposite direction away **from** the threshold as part of the leaky feature. Green lines indicate input signal spikes that incrementally drive the DW, while the red line indicates the position of the DW.

In the previous discussions, achieving multi-state spintronic devices require the formation of multiple domains. The resolution of the multi-states is reduced as devices scale down, resulting in fewer domains and reducing the number of useable states. Therefore, an approach to encode the necessary information would be to use the time domain of a stochastic binary MTJ. When

the energy barrier height E_B between magnetization states is reduced, such that thermal noise is able to randomly flip the FL magnetization in an MTJ between parallel and anti-parallel states, its behaviour becomes stochastic [80]. Recently, voltage-controlled stochastic MTJs were demonstrated to output a sigmoidal probability activation function for handwritten digit recognition [81].

As one of the evolutions of devices and systems proposed in the IRDS, research on emerging memory and computational technologies are critical as the CMOS fundamental limits approach. Commercial spintronic devices such as the STT-MRAM offer non-volatile, high-speed, high-endurance, power-efficient memory, and have been present in the market for several years. They have proven to be just as reliable as CMOS-based memories. Spintronic devices have been shown to demonstrate bio-plausible behaviours and characteristics. This allows spintronic devices to be used to develop a complete set of neuromorphic hardware primitives. There have been several proposals and proof-of-concepts for spintronic devices in neuromorphic engineering and computing, and new opportunities continue to be explored in developing brain-inspired spintronic neuromorphic hardware for more efficient computation. Spintronic neuromorphic devices are an encouraging approach to advancing brain-inspired computing, whether it is to mimic brain functionality for better understanding of the inner workings of the biological brain, or to develop better neuromorphic technologies for practical applications.

2.3 Spintronics for Probabilistic Computing

Rather than computing with traditional binary data represented by “1”s and “0”s, it has been proposed that information can be encoded using probabilistic bits [82]. While traditional memory is expected to be written deterministically and reliably, probabilistic bits are intended to operate stochastically using statistically random noise inputs such as thermal noise. Hardware random number generators based on such devices are important for applications such as

cryptography, as they are truly random and not based on algorithms. Furthermore, probabilistic bits also find applications in neuromorphic engineering, as the biological brain does not operate deterministically with clear distinctions or thresholds, and noise in the brain helps with decision making [83].

While most spintronic memory elements rely on the deterministic behaviour of nanomagnets and magnetization states, probabilistic characteristics can be achieved through careful tuning of geometric and material parameters to induce auto-oscillations [30,84-86]. Using these spintronic nano-oscillators, hardware for neuromorphic applications such as vowel recognition, signal processing, and edge detection have been proposed and demonstrated [30,31,33]. More recently, probabilistic bits (or p-bits) were introduced using low-barrier magnets or magnets with weak anisotropy [87]. The concept of using stochastic MTJs was implemented to demonstrate integer factorization [88]. In addition to thermally-induced magnetization switching of the low-barrier magnet, a bias can be used to tune the tendency for the magnetization to be in the up or down state. Due to the ultrafast dynamics of the magnetization, the average magnetization state probed over an interval gives the probability which can be used as an analogue-like output. We further discuss on probabilistic spintronic devices, in particular the stochastic MTJ as a multistate device, in **8.2 Future Works**.

Chapter 3
Magnetism and Spintronics

In this chapter, we discuss the fundamental principles and theoretical background of the various phenomena that will be used in this thesis. We begin with basic magnetism and magnetic energies that are used to approximate the magnetization dynamics. Subsequently, we build the foundation necessary for understanding spintronic device fundamentals.

3.1 Orbital and Spin Angular Momentum

Aside from the electronic charge, an electron also possesses an intrinsic spin. The spin of an electron was first evident in an experiment by two German physicists, Otto Stern and Walther Gerlach, in the Stern-Gerlach experiment in 1922 [89]. The Stern-Gerlach experiment showed that a beam of silver vapour passing through an inhomogeneous magnetic field splits into two discrete and distinct regions on the detector screen. This was due to an internal magnetic moment afforded by an uncompensated single electron of the electrically neutral silver atoms [90]. This additional degree of freedom differentiates spintronics from conventional charge-based electronics.

The orbital motion of an electron about an atomic nucleus as well as its intrinsic spin contributes to the magnetic properties of materials. When an electron orbits an atomic nucleus, is it analogous to a current loop I flowing in a closed loop of area $\vec{A}$, which gives rise to a magnetic moment $\vec{\mu}$:

$$\mu_l = IA \tag{1}$$

where the direction of the vector $\vec{A}$ is normal to the area enclosed by the current loop. The orbital angular momentum of the electron is given by $\vec{l} = \vec{r} \times \vec{p}$, where

$\vec{r}$ and $\vec{p}$ are the position and momentum of the electron, respectively. Then, the orbital moment can be calculated using equation (1) by substituting $I = -\frac{e}{\tau} = -e/(2\pi r/v)$ and $A = \pi r^2$:

$$\begin{aligned} \mu_l &= IA \\ &= -\frac{e}{2m_e} l \end{aligned} \quad (2)$$

where $e = 1.6 \times 10^{-19}$ C is the elementary charge, m_e is the electronic mass. Since the z-component of the orbital angular momentum l_z is quantized in $\hbar$,

$$l_z = m_l \hbar \quad (3)$$

where $\hbar$ is the reduced Planck's constant and m_l is the magnetic quantum number. Thus, the z-component of the orbital moment μ_{lz} is then:

$$\begin{aligned} \mu_{lz} &= -\frac{e\hbar}{2m_e} m_l \\ &= -\mu_B m_l \end{aligned} \quad (4)$$

where the Bohr magneton μ_B has been defined as $\mu_B = e\hbar/2m_e = 9.724 \times 10^{-24}$ Am^2. The electron also has a spin magnetic moment $\vec{\mu}_s$ due to its intrinsic spin $\vec{S}$ which is given by:

$$\begin{aligned} \vec{\mu}_s &= -\frac{e}{m_e} \vec{S} \\ &= \gamma \vec{S} \end{aligned} \quad (5)$$

where the gyromagnetic ratio $\gamma \approx 1.760 \times 10^{11}$ s^{-1}T^{-1}. γ is an important quantity that describes the sub-nanosecond dynamics of spins due to torques exerted on it such as by an external magnetic field or by current-induced spin-orbit torques.

3.2 Magnetic Interactions, Energies, and Fields

The torques experienced by the magnetization can be attributed to an effective magnetic field $\vec{H}_{eff}$ acting on it. In energy terms, this effective field can be a conglomeration of various contributions including demagnetization, anisotropy, Zeeman, exchange and Dzyaloshinskii-Moriya interactions.

3.2.1 Symmetric Exchange Interaction

Magnetic moments tend to align parallel in FM materials and anti-parallel in AFM materials, as shown in **Figure 12**. The parallel or anti-parallel alignment of magnetization originates from the Heisenberg exchange coupling, and the energy of the system is due to this symmetric exchange given by:

$$E_H = -\sum J_{ij} \cdot (S_i \cdot S_j) \tag{6}$$

where J_{ij} is the coupling between neighbouring spins S_i and S_j. The energy is minimized when magnetization is aligned parallel for the case of FM materials with $J_{ij} > 0$, and anti-parallel for the case of AFM materials with $J_{ij} < 0$.

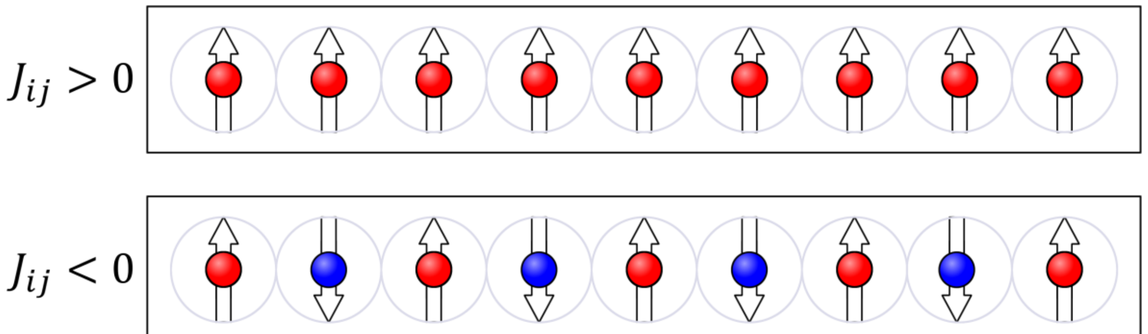

Figure 12: Parallel alignment of magnetization for $J_{ij} > 0$, and anti-parallel alignment of magnetization for $J_{ij} < 0$.

3.2.2 Asymmetric Exchange Interaction (Dzyaloshinskii-Moriya Interaction)

An asymmetric exchange also known as Dzyaloshinskii-Moriya interaction (DMI) which results in stable CW or CCW magnetization chirality, is shown in **Figure 13**.

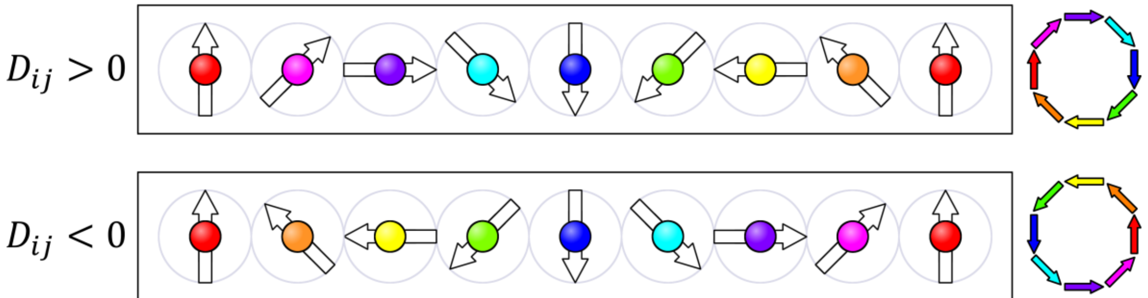

Figure 13: (a) Clockwise chirality for $D_{ij} > 0$. (b) Counter-clockwise chirality for $D_{ij} < 0$.

Dzyaloshinskii first constructed a model to describe "weak" ferromagnetism in AFMs [91]. Moriya subsequently correlated the interaction mechanism in part to SOC [92]. The DMI is an anisotropic exchange interaction that manifests due to inversion asymmetry in a crystal lattice. It influences the formation of magnetic textures such as skyrmions and chiral DWs, and has been of great interest in spintronic devices. DMI exists in bulk materials such as MnSi, as well as at the interfaces of HM/FM. The interfacial DMI as illustrated in **Figure 14** is mainly discussed here as the work presented in this thesis is primarily on ultrathin films and multilayers. Due to the SOI, the relationship between DMI and other magnetic parameters such as exchange stiffness A, saturation magnetization M_s, and uniaxial anisotropy K_u, have been discussed in several works [93-96]. The Hamiltonian that describes the DMI can be written as the resulting interaction between an atom with large SOC and two neighbouring spins.

$$E_{DMI} = -\vec{D}_{ij} \cdot (\vec{S}_i \times \vec{S}_j) \quad (7)$$

where $\vec{D}_{ij}$ is the DMI interaction vector acting on neighbouring spins $\vec{S}_i$ and $\vec{S}_j$. If the vector joining two spins $R_{ij} \perp D_{ij}$, then the energy is minimized as $\vec{S}_i$ and $\vec{S}_j$ cant away from each other [97].

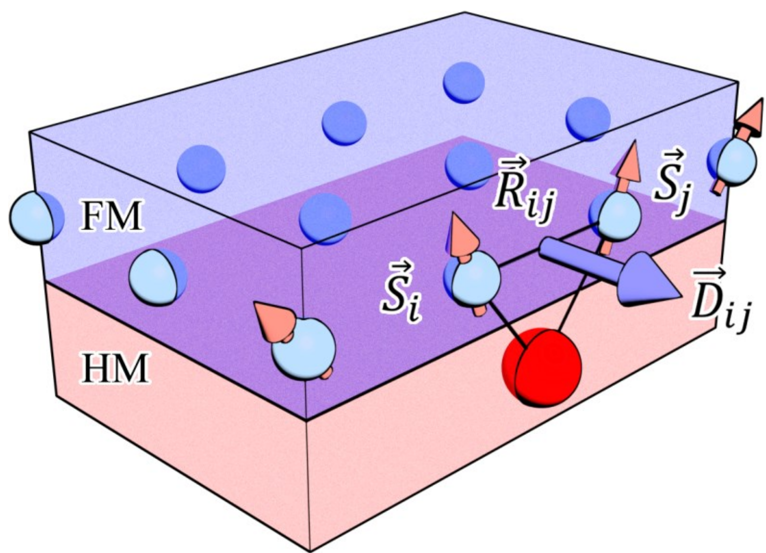

Figure 14: Spin (blue spheres) canting in the ferromagnetic layer due to interfacial DMI from an adjacent HM atom (red sphere).

3.2.3 Zeeman Energy

In the presence of an external magnetic field $\vec{H}_{ext}$, a system with magnetization $\vec{M}$ has an energy that is dependent on the relative angles between them, and is represented by the statistical average over a volume:

$$E_{Zeeman} = -\mu_0 \int_V \vec{M} \cdot \vec{H}_{ext} \, dV \quad (8)$$

The Zeeman energy E_{Zeeman} is minimized when the magnetization and external field vectors are coaxial.

3.2.4 Anisotropy Energy

The magnetic anisotropy of a material is the tendency of the magnetization to align along one or more preferential directions or planes. Anisotropy can be induced by the geometry and structure of the material which

leads to shape anisotropy, or a result of spin-orbit interaction which leads to magnetocrystalline anisotropy and interfacial anisotropy. The shape anisotropy is a result of dipolar interaction. For ferromagnetic films with in-plane anisotropy, the magnetization prefers to lie in the plane of the film (xy-plane). Due to the demagnetizing field H_{demag}, the geometric shape influences the anisotropy axis. The magnetocrystalline anisotropy is due the crystal axes of a ferromagnetic material, requiring less energy to align the magnetization along a more favourable easy axis that typically coincides with the principal axes of the crystal lattice, such as by having a cubic or hexagonal crystal system [98]. The anisotropy of a thin film can also be influenced by interfacing dissimilar materials such as the MgO/CoFeB bilayer [96,99]. The interfacial anisotropy can be improved and optimized through annealing processes, which allows the thin films to form a more ordered crystal structure. If there is one axis of anisotropy, it is said that the system has uniaxial anisotropy or an easy axis. The uniaxial anisotropy energy can be expressed as:

$$E_{uniaxial} = -K_u \cos^2 \theta \tag{9}$$

where K_u is the anisotropy energy density, θ is the angle between the magnetization and the anisotropy axis. $E_{uniaxial}$ is minimized when the magnetization lies along the axis of anisotropy.

3.2.5 Demagnetization Energy

The magnetic moments abruptly stop at the surface of magnetic elements, resulting in a demagnetization field due to the divergence of $\vec{M}$.

$$\nabla \cdot \vec{H} = -\nabla \cdot \vec{M} \tag{10}$$

The demagnetizing field for arbitrarily shaped objects is not straightforward to calculate. However, if the magnetic element can be approximated to an ellipsoid, then the demagnetizing field can be similarly

approximated using a geometry-dependent demagnetizing factor. Gauss's law for magnetism states that the magnetic field $\vec{B}$ has zero divergence, given by:

$$\nabla \cdot \vec{B} = 0 \quad (11)$$

The magnetic field and flux density are related by:

$$\vec{B} = \mu_0(\vec{M} + \vec{H}) \quad (12)$$

where μ_0 is the vacuum permeability, $\vec{H}$ is the demagnetizing field, and $\vec{M}$ is the magnetization. The demagnetizing energy can then be calculated by:

$$E_{demag} = -\frac{\mu_0}{2}\int \left(N_x M_x^2 + N_y M_y^2 + N_z M_z^2\right) dV \quad (13)$$

where N_i $(i = x, y, z)$ are known as the demagnetizing factors and $\sum_i N_i = 1$. The shape of the specimen determines the values of N_i. $N_x = N_y = N_z = 1/3$ for a sphere, while $N_x = N_y = 1/2$, $N_z = 0$ for an infinitely long rod lying along the z-axis [100]. Thin films can be approximated by an oblate ellipsoid with $N_z \gg N_x, N_y$, then $N_z \cong 1$ and $N_x, N_y \cong 0$ and:

$$E_{demag} \cong \text{const.} - \frac{1}{2\mu_0} M^2 V \cos^2\theta \quad (14)$$

3.3 Stoner-Wohlfarth Model

The Stoner-Wohlfarth (SW) model developed by E. C. Stoner and E. P. Wolfarth in 1948 can analytically model the coherent rotation of a single domain ferromagnetic particle [101]. It describes the magnetic hysteresis of a ferromagnetic particle, as its magnetization vector $\vec{M}$ rotates in a sweeping external magnetic field vector $\vec{H}$ whose magnitude is varied along one axis. Effects due to domains and inhomogeneities are neglected, $\vec{M}$ is restricted to a

two-dimensional space, and the amount of magnetization M_s does not vary in the ferromagnet.

We can model the behaviour of a single domain magnet using the SW model. The magnetization of a ferromagnet changes when a magnetic field is applied. These changes can be understood by sweeping an externally applied magnetic field $\vec{H}_{ex}$ and plotting the magnetization $\vec{M}$ projected on to the direction of $\vec{H}$, which results in an $M - H$ hysteresis loop. There are several characteristics of a hysteresis loop: (i) The saturation magnetization $M_s = |\vec{M}|$ which is the largest value of magnetization when all the magnetic moments align along one direction, (ii) the remanent magnetization M_r which is the remaining magnetization when $\vec{H} = 0$ and describes the non-volatility of the ferromagnet, (iii) the coercivity or coercive field H_c at $\vec{M} = 0$, and the anisotropy field H_k. For simple systems with uniaxial anisotropy, an easy axis or anisotropy axis can be identified when the hysteresis loop closely approximates a square shape, and the squareness is close to unity ($M_r/M_s \approx 1$).

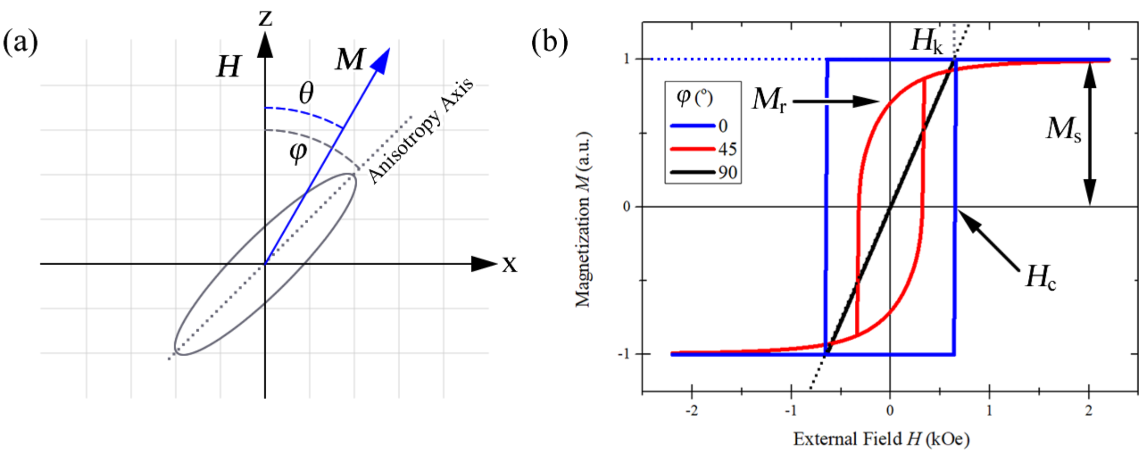

Figure 15: (a) Stoner-Wohlfarth particle with anisotropy axis along the xz plane. (b) $M - H$ hysteresis loops of the Stoner-Wohlfarth particle with anisotropy axis along $\varphi = 0°$ (blue), 45° (red), and 90° (black).

Figure 15 (a) is a schematic of a SW particle. The externally applied field $\vec{H}$ in this convention points along the z-axis. θ and φ are the angles of $\vec{M}$ and the

uniaxial anisotropy axis with respect to $\vec{H}$, respectively. In the absence of an external magnetic field, $\vec{M}$ points in either opposite directions along the anisotropy axis. $\vec{M}$ is therefore in competition between the anisotropy energy $E_a = -K_\mathrm{u}\cos^2\varphi$ and the Zeeman energy $E_\mathrm{z} = -\vec{M}\cdot\vec{H}$. The total energy per unit volume is then:

$$
\begin{aligned}
E = E_a + E_z &= -K_\mathrm{u}\cos^2\varphi - \vec{M}\cdot\vec{H} \\
&= -K_\mathrm{u}\cos^2\varphi - HM_s\cos(\theta)
\end{aligned}
\qquad (15)
$$

In the case where $\varphi = 0^\circ$, the anisotropy and external field share the same axis such that the external field is swept along the particle's easy axis. This results in the square blue hysteresis in **Figure 15** (b). The intercept at $M = 0$ is the magnitude of $\vec{H}$ required to overcome the particle's anisotropy known as the coercivity H_c. The magnetization at the extremes of the $\vec{H}$ is known as the saturation magnetization M_s. The amount of magnetization at $\vec{H} = 0$ Oe is the remanence M_r. When $\vec{H}$ is orthogonal to the anisotropy axis of the particle, $\varphi = 90^\circ$ and the field oriented along the hard axis. The hard axis hysteresis is plotted in black and shows a linear response with no coercivity or remanence. From this hysteresis loop, the anisotropy field H_k of the particle can be obtained by integrating the area indicated in orange and using the relationship:

$$
K_u = \frac{1}{2}\mu_0 M_s H_k \qquad (16)
$$

The hysteresis loop at an intermediate angle of $\varphi = 45^\circ$ is plotted in red.

3.4 Dynamic Equation

The dynamics of local magnetization $\vec{M}(\vec{r})$ within a solid can be modelled using the Landau-Lifshitz-Gilbert (LLG) equation of motion:

$$\frac{d\vec{M}}{dt} = -\gamma\mu_0 \vec{M} \times \vec{H}_{\text{eff}} + \frac{\alpha}{M_s} \vec{M} \times \frac{d\vec{M}}{dt} \tag{17}$$

where γ is the electron's gyromagnetic ratio, μ_0 is the permeability of free space, $\vec{H}_{eff}$ comprises of contributions such as the external magnetic field H_{ext}, anisotropy field H_{aniso}, demagnetizing field H_{demag}, α is the Gilbert damping constant, and M_s is the saturation magnetization. The first and second terms on the RHS of equation (17) are the precession and damping terms, respectively. If we assume that the solid behaves as a single SW particle, then the magnetization at every point in the solid precesses coherently without and with damping as shown in **Figure 16** (a) and (b), respectively, and we can ignore the formation of magnetic domains, i.e. $\vec{M}(\vec{r}) \rightarrow \vec{M}$. This macrospin approximation simplifies solving a singular LLG equation and allows for a qualitative understanding of magnetization dynamics. A more realistic model would involve *N* interacting spins or domains.

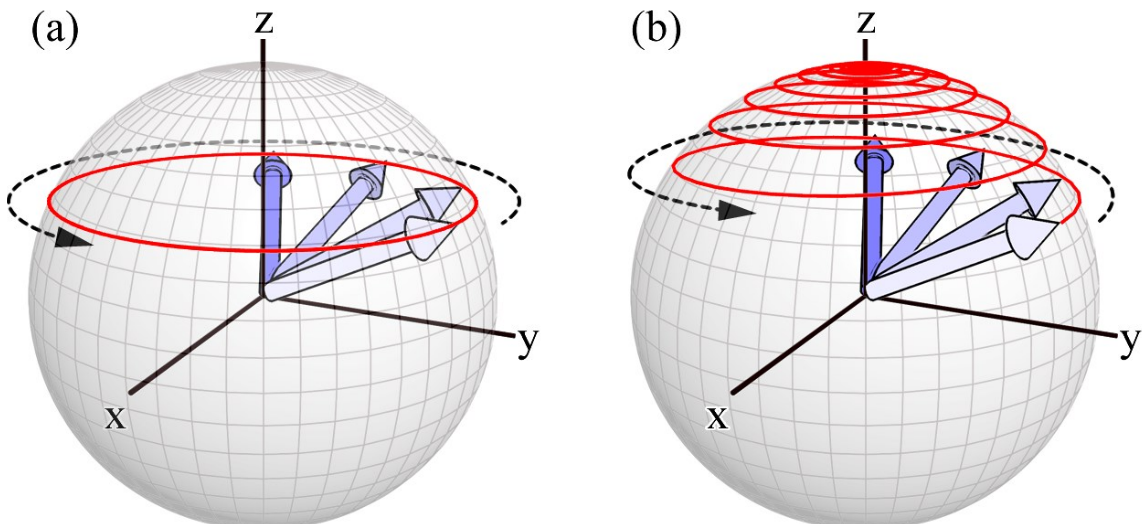

Figure 16: (a) Precession of a spin without damping. (b) Precession of a spin with non-zero damping.

Equation (17) can be transformed into a dimensionless equation of motion for a unit magnetization by dividing both sides of the equation by M_s:

$$\frac{\mathrm{d}\vec{m}}{\mathrm{dt}} = -\gamma\mu_0\vec{m} \times \vec{H}_{\mathrm{eff}} + \alpha\vec{m} \times \frac{\mathrm{d}\vec{m}}{\mathrm{dt}} \tag{18}$$

where the dimensionless unit magnetization is given by $\vec{m} = \frac{\vec{M}}{M_s}$.

The LLG equation discussed thus far has been implicit in form. An explicit form can be obtained by taking the cross product of $\vec{m}$ on both sides of equation (18).

$$\begin{aligned} \vec{m} \times \frac{\mathrm{d}\vec{m}}{\mathrm{dt}} &= -\gamma\mu_0\vec{\mathrm{m}} \times (\vec{m} \times \vec{H}_{\mathrm{eff}}) + \alpha\vec{m} \times (\vec{m} \times \frac{\mathrm{d}\vec{m}}{\mathrm{dt}}) \\ &= -\gamma\mu_0\vec{m} \times (\vec{m} \times \vec{H}_{\mathrm{eff}}) + \alpha\vec{m}(\vec{m} \cdot \frac{\mathrm{d}\vec{m}}{\mathrm{dt}}) \\ &- \alpha|\vec{m}|^2 \frac{\mathrm{d}\vec{m}}{\mathrm{dt}} = -\gamma\mu_0\vec{m} \times (\vec{m} \times \vec{H}_{\mathrm{eff}}) - \alpha\frac{\mathrm{d}\vec{m}}{\mathrm{dt}} \end{aligned} \tag{19}$$

Substituting equation (19) into equation (18):

$$\frac{\mathrm{d}\vec{m}}{\mathrm{dt}} = -\gamma\mu_0\vec{m} \times \vec{H}_{\mathrm{eff}} + \alpha(-\gamma\mu_0\vec{m} \times (\vec{m} \times \vec{H}_{\mathrm{eff}}) - \alpha\frac{\mathrm{d}\vec{m}}{\mathrm{dt}}) \tag{20}$$

When solving the LLG equation, the magnitude of magnetization is conserved throughout the motion of $\vec{M}$, such that $|\vec{m}(t)| = |\vec{m}(0)| = 1$.

Polarized electrons injected into a ferromagnet can exert torque on the local magnetization and lead to magnetization reversal, and the dynamics of the local magnetization can be described by a modified Landau-Lifshitz-Gilbert equation [102].

$$\frac{\mathrm{d}\vec{m}}{\mathrm{dt}} = -\gamma\mu_0\vec{m} \times (H_{\mathrm{eff}} + \mathrm{b}\vec{\sigma}) + \alpha\vec{m} \times \frac{\mathrm{d}\vec{m}}{\mathrm{dt}} + \gamma\vec{m} \times (\vec{m} \times \mathrm{a}\vec{\sigma}) \tag{21}$$

where $\vec{m}$ is the unit magnetization, $\vec{H}_{eff}$ is the effective field, and $\vec{\sigma}$ is the injected spin polarization orientation.

3.5 Spin Tranport

The intrinsic spin of electrons can be polarised, as was demonstrated in the Stern-Gerlach experiment in which a beam of silver atoms was passed through an inhomogeneous magnetic field. The particles were deflected due to the magnetic field gradient. Silver, being a massive neutral atom with an unpaired electron, did not deflect due to its neutral charge. The patterned formed when the beam of silver atoms struck a detector screen suggesting that the silver atoms had two discrete values of magnetic moment along the direction of the field. This was convincing evidence of the quantization of angular momentum of the atoms 'spin up' and 'spin down'. Typically, the spins of electrons are randomly polarized. However, when these randomly polarized electrons conduct through FM materials, momentum transfer occurs between the local magnetization and itinerant electrons. Alternatively, passing charge current through a HM with large SOC leads to preferentially polarized spin accumulation on the lateral surfaces of the HM conductor. Typically, the spins are described as up or down, indicating the majority presence of one or the other.

3.5.1 Spin Currents

A spin current can be defined as a flow of angular momentum. It is typical to describe spin current densities in up and down states, $J_\uparrow$ and $J_\downarrow$, based on some defined quantization axis. The charge and spin current densities, J_c and J_s, can then be described as:

$$J_c = J_\uparrow + J_\downarrow$$
$$J_s = J_\uparrow - J_\downarrow \tag{22}$$

For a flow of electrons with up and down spins along a conductor, the charge current density J_c is simply the total current density $J_\uparrow + J_\downarrow$, while the spin current density J_s is the net difference between the up and down spin electrons $J_\uparrow - J_\downarrow$. Three scenarios of charge and spin current flow can yield from this, as

illustrated in **Figure 17** (a) to (c). For a pure charge current, a net charge flows along the conductor, but the net spin polarization is zero. For a pure spin current, there is no net charge flow, but there is a non-zero spin current flow. For a spin-polarized current, there is both non-zero charge and spin current flow.

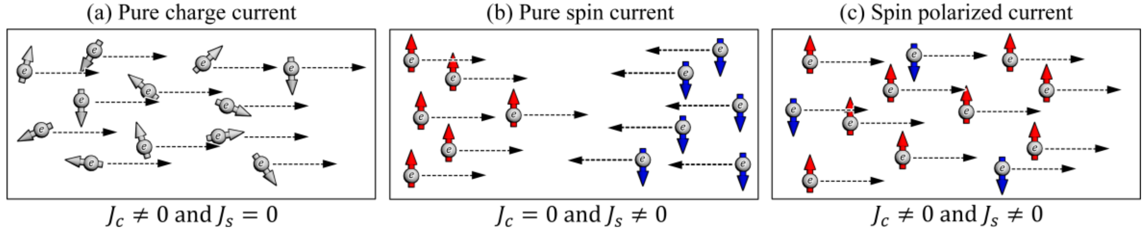

Figure 17: (a) Pure charge current with randomly oriented spins. (b) A pure spin current has no net electronic charge flow, but a non-zero spin current flow. (c) A spin polarized current with non-zero charge and spin current flow.

3.5.2 Characteristic Lengths

When electrons move inside a conductive medium, they experience scattering due to impurities, defects, and thermal noise. The mean distance an electron travels between scattering events is known as the mean free path λ of the electron, given by

$$\lambda = v_F \tau \tag{23}$$

where v_F is the Fermi velocity, and τ is the mean free time between collisions. In general, scattering gives rise to the electrical resistivity of the material, however, such scattering events can also result in the flipping of the electron spin. This results in the loss of spin information as the electron changes spin orientation. The mean spin flip length is given by:

$$\lambda_{sf} = v_F \tau_{sf} \tag{24}$$

where τ_{sf} is the mean time between spin flip collisions. λ_{sf} is characteristic of the material, its purity, as well as the temperature. Spin flipping also occurs when electrons cross interfaces between two different materials.

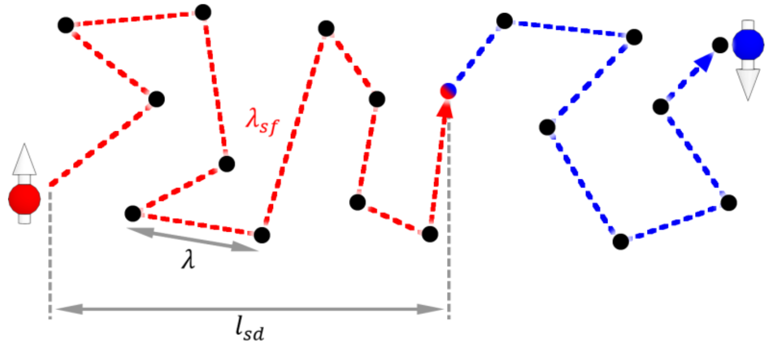

Figure 18: Representation of an electron and characteristic lengths.

We now describe the mean distance in the direction of electron flow (in a normal metal) between spin-flip collisions as the spin diffusion length, given as the geometric mean of λ and λ_{sf} shown in **Figure 18** as per equation (24):

$$l_{sd} = \sqrt{(1/3)\lambda\lambda_{sf}} \tag{25}$$

The $\sqrt{1/3}$ pre-factor accounts for the three-dimensional scattering mechanism. Spin diffusion lengths vary with material properties and impurities that are present. Materials with large SOC such as Pt and Ta have short spin diffusion lengths [103,104].

3.5.3 Two-Channel Model

The two-channel model is used to account for the electron spin as a charge current travels through a conductor. Due to the spin-flip process, a spin-up electron can transition to the spin-down state, and vice versa. While there are different methods to model the mechanism of electron transport, the spin diffusion equations formulated here are modelled based on room-temperature approximations in which the spin transport is diffusive. This is in contrast with low-temperature systems in which quantum effects must be taken into

consideration. **Figure 19** (a) and (b) shows a distributed transmission line representation [105].

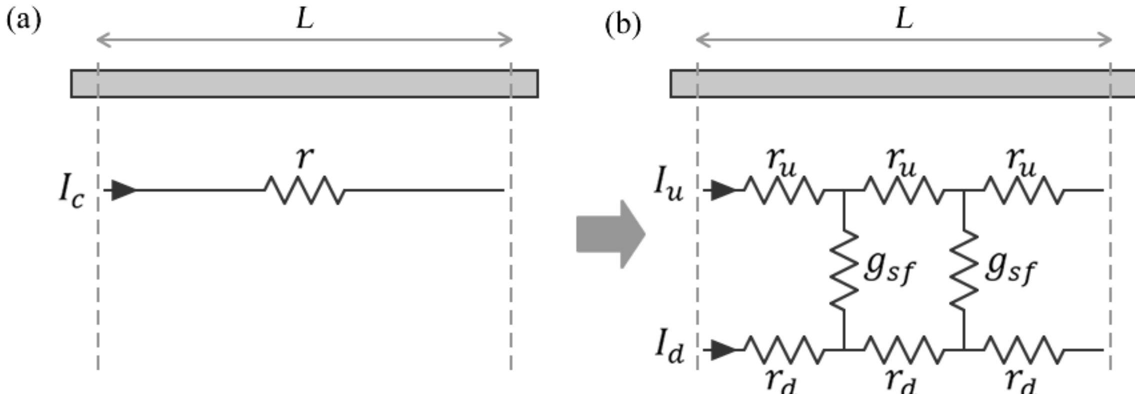

Figure 19: Transmission line representation for (a) charge current I_c through a resistive load of length l and resistance r, and (b) two-channel model accounting for spin-up and spin-down electrons, and intermittent spin-flip conductances g_{sf} bridging up and down spin current lines.

The one-dimensional transport of charge current can be separated into up and down spin currents propagating along separate conducting channels with respective distributed resistances r_u and r_d. Intermittently, the up and down spin current channels are connected to each other by spin-flip conductances g_{sf}. The spin currents are driven by voltages $V_{u(d)}$ defined by up(down) spin chemical potentials $\mu_{u(d)}$.

$$V_{u(d)} = \frac{\mu_{u(d)}}{e} \quad (26)$$

The spin-dependent electron current for one-dimensional transport can then be written as:

$$r_{u(d)} I_{u(d)} = -\frac{d}{dx} V_{u(d)} = -\frac{d}{dx}\left(\frac{\mu_{u(d)}}{e}\right) \quad (27)$$

where $r_{u(d)}$ is the resistance per unit length along the up(down) spin channel. The rate at which the two spin channels equalize is proportional to the difference in chemical potentials between the two channels.

$$\frac{dI_{u(d)}}{dx} = \frac{g_{sf}}{e}\left(\mu_{u(d)} - \mu_{d(u)}\right) = g_{sf}\left(V_{u(d)} - V_{d(u)}\right) \tag{28}$$

At steady state, the charge current given by $I_c = I_u + I_d$ is constant in the system and does not vary across the length of the conductor.

$$\frac{d}{dx}(I_u + I_d) = 0 \Rightarrow \frac{dI_u}{dx} = -\frac{dI_d}{dx} \tag{29}$$

3.5.4 Decoupling of the Charge and Spin Quantities

Writing these equations in matrix form:

$$\frac{d}{dx}\begin{bmatrix} V_u \\ V_d \end{bmatrix} = -\begin{bmatrix} r_u & 0 \\ 0 & r_d \end{bmatrix}\begin{bmatrix} I_u \\ I_d \end{bmatrix} \tag{30}$$

$$\frac{d}{dx}\begin{bmatrix} I_u \\ I_d \end{bmatrix} = -g_{sf}\begin{bmatrix} 1 & -1 \\ -1 & 1 \end{bmatrix}\begin{bmatrix} V_u \\ V_d \end{bmatrix} \tag{31}$$

Now, the charge and spin quantities can be represented as,

$$V_c = \frac{V_u + V_d}{2}, \qquad I_c = I_u + I_d \tag{32}$$

$$V_s = \frac{V_u - V_d}{2}, \qquad I_s = I_u - I_d \tag{33}$$

Substituting equations (32) and (33) into (30) and (31) results in:

$$\frac{d}{dx}\begin{bmatrix} V_c \\ V_s \end{bmatrix} = -\frac{1}{4}\begin{bmatrix} r_+ & -r_- \\ -r_- & r_+ \end{bmatrix}\begin{bmatrix} I_c \\ I_s \end{bmatrix} \tag{34}$$

$$\frac{d}{dx}\begin{bmatrix} I_c \\ I_s \end{bmatrix} = \begin{bmatrix} 0 & 0 \\ 0 & -4g_{sf} \end{bmatrix}\begin{bmatrix} V_c \\ V_s \end{bmatrix} \tag{35}$$

where $r_{\pm} = r_d \pm r_u$. Subsequently, the voltage and current equations for charge can be separated:

$$\frac{d}{dx}V_c = -\frac{r_u}{2}I_c \tag{36}$$

$$\frac{d}{dx}I_c = 0 \tag{37}$$

Equation (36) describes Ohm's law for the two-channel model having an effective resistance of $r_u/2$ assuming $r_u = r_d$. Equation (37) describes the steady-state condition where current flow is uniform across space.

Similarly, the voltage and current equations for spin are:

$$\frac{d}{dx}V_s = -\frac{r_u}{2}I_s \tag{38}$$

$$\frac{d}{dx}I_s = -4g_{sf}V_s \tag{39}$$

Equation (38) is Ohm's law for the spin current, which shares the same effective resistance $r_u/2$ as with the charge current. However, equation (39) includes spin-flip conductance g_{sf} which causes attenuation of the spin current I_s along the conductor of length L. The charge current, however, is not affected by spin-flip processes.

3.5.5 Diffusion Equations

The diffusion equations govern the motion of charge and spin based on the two-channel model. Differentiating equation (35) results in:

$$\frac{d^2}{dx^2}\begin{bmatrix} V_c \\ V_s \end{bmatrix} = -\frac{1}{4}\begin{bmatrix} r_+ & -r_- \\ -r_- & r_+ \end{bmatrix}\frac{d}{dx}\begin{bmatrix} I_c \\ I_s \end{bmatrix}$$
$$= -\frac{1}{4}\begin{bmatrix} r_+ & -r_- \\ -r_- & r_+ \end{bmatrix}\begin{bmatrix} 0 & 0 \\ 0 & -4g_{sf} \end{bmatrix}\begin{bmatrix} V_c \\ V_s \end{bmatrix} \quad (40)$$
$$= \begin{bmatrix} 0 & -r_- g_{sf} \\ 0 & r_+ g_{sf} \end{bmatrix}\begin{bmatrix} V_c \\ V_s \end{bmatrix}$$

where equation (35) was substituted for the first derivative of the charge and spin currents with respect to x. For non-magnetic conductors, $r_d = r_u$ and $r_- = r_d - r_u = 0$, therefore the diffusion equations now become:

$$\frac{d^2}{dx^2}\begin{bmatrix} V_c \\ V_s \end{bmatrix} = \begin{bmatrix} 0 \\ V_s(r_+ g_{sf}) \end{bmatrix} = \begin{bmatrix} 0 \\ V_s/\lambda_{sd}^2 \end{bmatrix} \quad (41)$$

where we have defined the characteristic length scale for spin diffusion $\lambda_{sd}^2 = (r_+ g_{sf})^{-1}$.

3.6 Spin Transfer Torque

STT magnetization switching is a technique that utilises the momentum transfer between the itinerant spin of an electron and the local magnetization. In this technique, randomly polarized electrons are injected through a fixed layer with strong anisotropy. This causes the electronic spins to align along the fixed layer magnetization. When the now-polarized electrons are injected into a second softer magnetic FL, angular momentum can be transferred from the itinerant spin to the local FL magnetization, subsequently changing the magnetization orientation. STT is used in MTJs as a means of switching magnetization in spintronic memory devices known as STT-MRAM. The torques due to STT can be decomposed into anti-damping and field-like torques. The anti-damping torque is dependent on the magnetization, which relaxes the magnetization towards the direction of the polarized spin. The field-like torque is independent of the magnetization, and precesses the magnetization about an exchange field.

While STT has been demonstrated to be a powerful technique for magnetization switching, several drawbacks have led to the development of alternative magnetization switching methods. Firstly, in order to perform reading and writing of the MTJ magnetization states, current is delivered along the same path through the MTJ. This leads to perturbation and unintentional magnetization switching due to the read process, also known as read-write disturb. The oxide tunnel barrier of the MTJ is also required to be made very thin in order to reduce the resistance-area product for low-voltage operation. This makes the thin oxide tunnel barrier prone to dielectric breakdown over the course of read-write operations.

3.7 Spin Orbit Coupling

The SOI or SOC can lead to phenomena such as magnetocrystalline anisotropy, anisotropic magnetoresistance (AMR), spin-dependent scattering in SHE, anomalous Hall effect (AHE), Dzyaloshinskii-Moriya interaction (DMI), Rashba effect, and Dresselhaus effect. SOC can be understood by considering an electron orbiting a positively charged nucleus $+Ze$ with linear velocity $\vec{v}$ in the nucleus' rest frame S. In the electron's frame of reference S', the nucleus orbits the electron, giving rise to an effective magnetic field experienced by the electron that interacts with its spin moment. These two inertial frames (S, S') are described by Lorentz transformations. In their respective reference frame, the electric and magnetic fields are $(\vec{E}, \vec{B})$ and $(\vec{E}', \vec{B}')$. The Lorentz transformation for $\vec{E}$ and $\vec{B}$ parallel and transverse to $\vec{v}$ are given by:

$$\begin{aligned} \vec{E}'_{\parallel} &= \vec{E}_{\parallel} \\ \vec{B}'_{\parallel} &= \vec{B}_{\parallel} \\ \vec{E}'_{\perp} &= \gamma(\vec{E}_{\perp} + \vec{v} \times \vec{B}) \\ \vec{B}'_{\perp} &= \gamma(\vec{B}_{\perp} - \frac{\vec{v}}{c^2} \times \vec{E}) \end{aligned} \tag{42}$$

where $\gamma = \frac{1}{\sqrt{1-v^2/c^2}}$ is the Lorentz factor and c is the speed of light. From equation (42), the $\vec{B}$-field can now be written as $\vec{B}'(\vec{v}) = \frac{1}{2c^2}\vec{E} \times \vec{v}$ where the $\frac{1}{2}$ factor is the relativistic Thomas factor due to the non-inertial frame [98]. The SOC field then gives rise to the Hamiltonian for the Zeeman energy given by [106]

$$H_{SOC} = \frac{\mu_B}{2c^2}\vec{\sigma} \cdot \left(\vec{E} \times \vec{v}\right) = \mu_B \vec{\sigma} \cdot \vec{B} \tag{43}$$

where $\vec{\sigma}$ is the vector of Pauli matrices. The SOC can manifest in various effects such as the spin Hall effect (SHE), Rashba effect, anomalous Hall effect, and magnetocrystalline anisotropy.

3.7.1 Spin Hall Effect

The SHE was first predicted by Dyakonov and Perel in 1971 [107,108]. A direct effect of the SHE is a charge-to-spin conversion, whereas the inverse effect can lead to spin-to-charge conversion [109]. The name itself was introduced by Hirsch as an analogue to the ordinary Hall effect [28]. As charge current flows through a HM, spins accumulate at the lateral edges, as depicted in **Figure 20**. In comparison with the classical Hall effect in which the presence of a magnetic field deflects the electron trajectory due to the Lorentz force, no magnetic field is necessary for the SHE. Instead, SHE originates from spin-dependent scattering as electrons flow through the sample. Over three decades after its first prediction, the SHE was experimentally observed in semiconductors [110,111], and subsequently detected in metals such as Pt and Al [112,113].

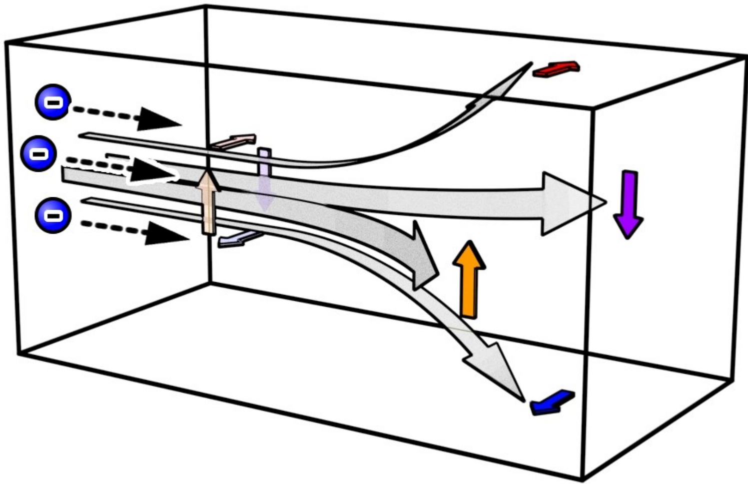

Figure 20: Charge current flow through a non-magnetic conductor leading to spin accumulation at the lateral interfaces due to the SHE.

The origin of the SHE can be attributed to intrinsic and extrinsic mechanisms. The intrinsic effect occurs in the absence of impurities within the material from which scattering can take place and is solely due to the band structure. Electrons flowing through the material experience a spin-dependent deflection of opposite directions in the presence of an electric field due to the atom's nucleus. There are two proposed extrinsic mechanisms in which an electron can undergo scattering due to impurities as illustrated in **Figure 21** (a) and (b).

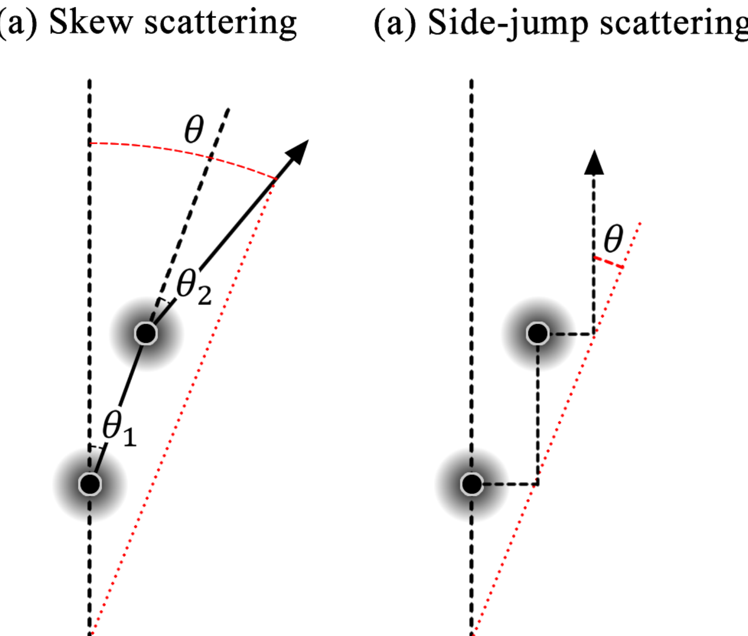

Figure 21: (a) Skew scattering and (b) side-jump scattering events.

When the concentration of impurities increases, the electrons will experience an increase in scattering events. In skew scattering, polarized electrons with linear velocity $\vec{v}$ are scattered by an electric field $\vec{E}$ from an impurity site with strong SOI as depicted. Due to the radial electric field from the nucleus, $\vec{E}$ and the emerging $\vec{B}'$-field is stronger closer to the nucleus. In the frame of the polarized electron, it experiences a magnetic field $\vec{B}\sim(\vec{v}\times\vec{E})$ perpendicular to the plane of the electron trajectory. If the electron spin is not aligned parallel or anti-parallel to $\vec{B}$, it will precess around $\vec{B}$. Mott scattering is also dependent on the spin orientation of the electron, and opposite electron spins will scatter in opposite directions:

$$\vec{F} = \vec{\nabla}(\vec{\mu}_s \cdot \vec{B}) \tag{44}$$

The side-jump scattering mechanism was introduced by Berger, and is so-called due to the finite lateral displacement of the centre of mass of a wave packet upon scattering against impurities as shown in **Figure 21** (b) [114]. It is therefore an extrinsic effect. However, it is independent on the impurity concentration and

therefore intrinsically contributes to the spin Hall effect. The spin-dependent scattering event results in opposite spins deflecting in opposite directions, and the wave packet leaves the impurity in the same direction and constant velocity.

The decay of the population of polarized spins is a result of spin flip scattering, which limits the lifetime in which a spin can maintain its orientation [115]. Spin flip scattering is a process in which the spin orientation is not conserved, as conduction electrons scatter from an impurity potential, leading to a decay in the population of spin polarized electrons.

3.7.2 Rashba Effect

The Rashba effect is an interfacial effect that manifests due to the broken crystal symmetry along the interface of two crystals with different crystal potentials. An electric field $\vec{E}$ forms along the z direction at the crystal interface. An electron traversing along the x direction with velocity $\vec{v}$ experiences this electric field, and the Rashba Hamiltonian is given as:

$$H_R = \frac{\alpha_R m}{\hbar} \vec{\sigma} \cdot (\hat{z} \times \vec{v}) \tag{45}$$

where α_R is the Rashba coupling parameter, and $\vec{\sigma} = (\sigma_x, \sigma_y, \sigma_z)$ is the vector of Pauli spin matrices.

3.7.3 Spin Orbit Torque

SOT magnetization switching allows for the separation of read and write current paths. Instead of electron polarization by momentum transfer between itinerant spin and local magnetization, SOT relies on spin polarization due to spin-orbit coupling in HMs such as Pt and Ta. The polarized spins accumulate along the lateral interface of the HM, accumulate at the HM/FM interface, and diffuse into the FM layer [28]. **Figure 22** shows the spin accumulation at the opposite interfaces of a HM/FM bilayer due to a current density J.

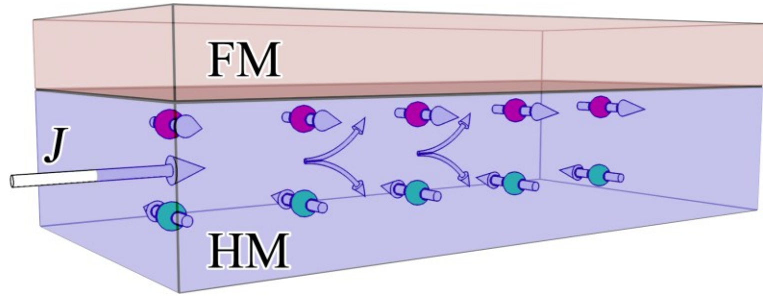

Figure 22: Spin accumulation at opposite interfaces of the HM/FM bilayer due to current density J.

The SOT can also be approximated as a current-induced out-of-plane effective field acting on a spin [116]. SOT has been demonstrated in systems with structural inversion asymmetry to induce fast DW motion [117-122], as well as magnetization switching [26,123-125]. The origin of SOT has been attributed to the SHE and the Rashba effect. Similarly, the SOT acting on the magnetization can be decomposed into anti-damping and field-like components through electrical characterization techniques such as the adiabatic harmonic Hall measurement [126-130].

3.7.4 Anomalous Hall Effect

In the ordinary Hall effect, an externally applied magnetic field $H(\hat{z})$ perpendicular to a charge current $I(\hat{x})$ flowing within a conductor results in a potential difference $V(\hat{y})$ transverse to the charge current flow. This potential difference is known as the ordinary Hall voltage. However, in FM materials, an analogous potential difference exists in the absence of any externally applied magnetic field. This Hall effect in FM materials (and in the absence of external magnetic fields) is referred to as the anomalous Hall effect (AHE). The transverse Hall voltage comprising the ordinary and anomalous Hall effects is then [131]:

$$V_H = I(R_o H_z + R_{AHE} M_z) \tag{46}$$

where R_o and R_{AHE} are the ordinary and anomalous Hall effect coefficients, respectively. H_z and M_z are the OOP components of the external magnetic field

and the magnetization in the FM layer, respectively. In FM materials, $R_A > R_o$, and the ordinary Hall effect is typically neglected.

Chapter 4
Fabrication and Characterization Techniques

In this chapter, the processes for thin film growth and device fabrication as well as equipment setup for measurement are described. Certain experimental techniques discussed in the later chapters are also introduced.

4.1 Device Fabrication

In order to form device structures, an SiO_2 substrate is first prepared by cleaning it using ultrasonication in acetone, followed by ultrasonication in isopropanol (IPA), before being thoroughly dried using a clean nitrogen jet. The substrate is visually inspected for particulate debris, scratches, or stains, and the cleaning process may be repeated until satisfactory. Subsequently, thin film deposition is performed in an ultra-high vacuum (UHV) chamber. The sputter-deposited substrate then undergoes lithography in order to pattern structural features. The electron beam lithography (EBL) process patterns structures or features for subsequent ion beam etching (IBE) or deposition processes. The process repeats for as many features and layers required for the completed device to be measured and characterized.

The process for device fabrication follows the process flow illustrated in **Figure 23**. The thin film sputtering, device patterning, and ion beam etching processes may be repeated or follow a different order to meet the final device requirements.

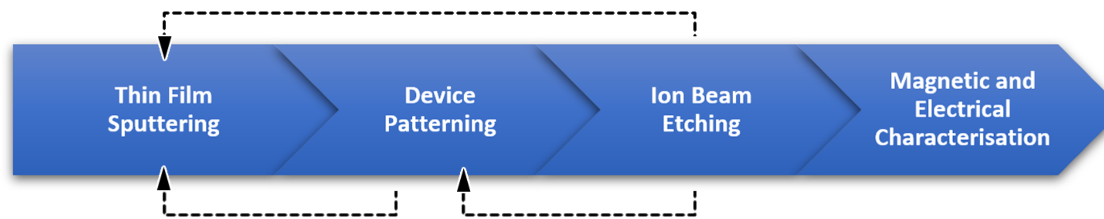

Figure 23: Process flow for device fabrication from bare Si wafer to fabricated device, ready for measurement and characterization. The order may be adjusted and repeated to meet the required end result.

4.1.1 Thin Film Sputtering

Sputtering is a PVD technique used for depositing thin films. It is a process commonly used in the industry for manufacturing semiconductor devices, display panels, as well as for optical coatings. The material to be sputtered comes in the form of a sputter target and is made by sintering or casting high-purity materials such as Ta, Au, Cu, MgO, CoFeB, NiFe, and others with varying stoichiometry. In the sputtering process, the target is ablated by accelerated atoms of a high-purity noble gas such as argon, krypton, or xenon. These process gases are used as they do not react with the target material unlike Oxygen or Nitrogen. The atoms ejected from the target then travel ballistically towards the substrate, depositing layer upon layer of the material film. High purity reactive gases such as O_2 and N_2 can be mixed in partial pressure to form oxides and nitrides, respectively. Conductive targets are typically sputtered using DC power, but may also be RF sputtered in certain cases such as to reduce the sputter deposition rate typically measured in $\mathrm{nm \cdot s^{-1}}$ or $\mathrm{Å \cdot s^{-1}}$. During the sputter process, a glow discharge would form just beyond the surface of the sputter target, indicative of successful sputtering process. Dielectric targets however must be sputtered using RF power, due to charges accumulating on the target surface which results in the collapsing of the plasma.

The sputter system used is the AJA Orion with 8 sources in the sputter-up configuration. A picture of the system is shown in **Figure 24** (a). The sources for

this system accept 2 inch diameter targets up to a total thickness of 6 mm, inclusive of any oxygen-free high-conductivity (OFHC) copper backing plates. Magnetic materials are limited to 3 mm thickness, and a special iron slug in place of the central magnet is required. The magnet pack creates an electron trap just beyond the surface of the target in order to increase the sputter rate efficiency and reduce the process pressure, parameters which can affect the way in which the deposited material forms on the substrate. The system can reach a base pressure of better than 1×10^{-8} Torr by means of a CTI cryopump. Seven confocal sources align at an oblique angle toward the substrate, and a central source directly faces the substrate. **Figure 24** (b) shows the plasma discharge from two confocal sources and one central source in a co-sputtering process. The target-to-substrate distance is adjustable from approximately 70 mm to 150 mm. The furthest target-to-substrate distance is typically used for most sputter processes to achieve uniformity under 5% across a 3-inch diameter substrate. The sputter parameters typically used are 20 sccm of Ar at 2 mTorr sputter pressure, or the lowest possible stable sputter pressure. The power delivered to each target depends on their thermal conductivity. MgO and other dielectrics with low thermal conductivity are typically indium-bonded to 3 mm thick OFHC copper backing plates, with up to 20 W/in^2 power density applied. Ramping the power up slowly prevents the target from cracking due to thermal expansion. Thermally conductive materials like most metals can afford a higher power density, but for fine control of the sputter rate and reliable growth of nominal thicknesses under 1 nm, 30 W to 100 W for 2 inch diameter targets are typically used.

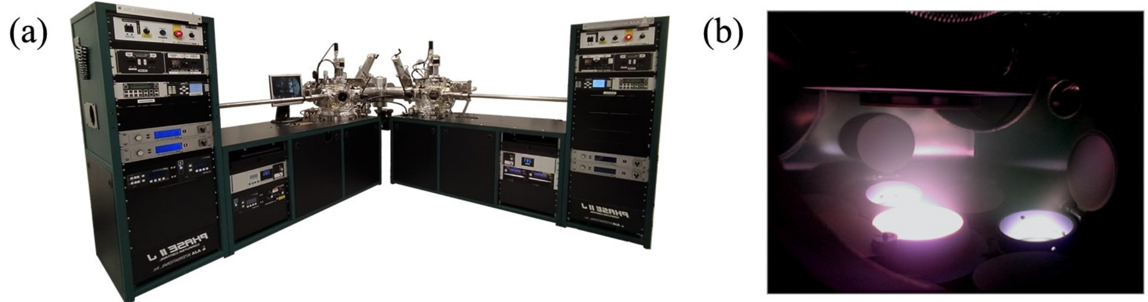

Figure 24: (a) AJA Orion sputter system. (b) Co-sputtering with two confocal and one central source within the UHV chamber.

The nominal sputter rate can be calibrated by depositing each material for a prescribed amount of time, and differs between materials. First, a resist is used to form a small mask on the substrate. The material is then sputter deposited across the substrate. An appropriate, prescribed resist remover is then used to remove the underlying resist, forming a distinct step structure of the sputter deposited material. The step height between sputtered material and substrate is then measured using atomic force microscopy (AFM) to determine the nominal sputter rate. If all the necessary target materials are available within the chamber, consecutive multilayers of thin films can be deposited without breaking vacuum, ensuring minimal oxidation and forming contiguous interfaces of each layer. The co-sputtering of more than one target material can also be performed as shown in **Figure 24** (b).

4.1.2 Electron Beam Lithography

Electron beam lithography (EBL) is a patterning process that makes use of chemical resists that undergo energy absorption processes upon exposure to an electron beam. This changes the solubility of the resist depending on whether a negative or positive tone resist is used. The samples are then developed in solvent to selectively remove the exposed or unexposed regions, leaving behind structures and features. EBL can achieve smaller critical dimensions and omits the need for a mask as compared to ultra-violet lithography (UVL). However, the much greater pattern design flexibility with EBL comes with a caveat: the

throughput is much slower since exposure is performed by raster scanning in small write fields of about 200 µm by 200 µm or smaller.

The EBL system used is the Raith e-Line as shown in **Figure 25**. The system utilises a thermal field emission electron gun for generating and emitting electrons. Up to 30kV can be used to accelerate the electrons down the optics column and focused to pattern the resist-coated substrate. The EBL system also functions as a secondary electron microscope (SEM) for taking nanoscale images.

Figure 25: Raith eLine electron beam lithography system.

4.1.3 Resist Spin Coating

The process for resist spin coating is illustrated in **Figure 26**. Preparing a substrate for EBL begins with resist spin-coating of a cleaned substrate. An adequate amount of resist is dispensed, and the spin cycle is performed. The spin speed and acceleration parameters depend on the resist and final thickness required, and can be referenced from the specific resist datasheet. Baking the

spin-coated substrate removes volatile solvents and compounds, and leaves behind a uniformly flat layer of resist. The substrate is then ready to be loaded in to the Raith e-Line load-lock before transferring it into the main process chamber. The structure pattern to transfer is prepared using a graphic design/data system (GDSII) editor, similar to 2D computer aided design (CAD) software. Orientation corrections and optimized exposure parameters not limited to dose rate, dwell time, and acceleration voltage can be set in order to meet feature requirements. The EBL system writes the patterns in smaller jobs using write fields, in which the electron beam is deflected across the substrate plane in a raster scan.

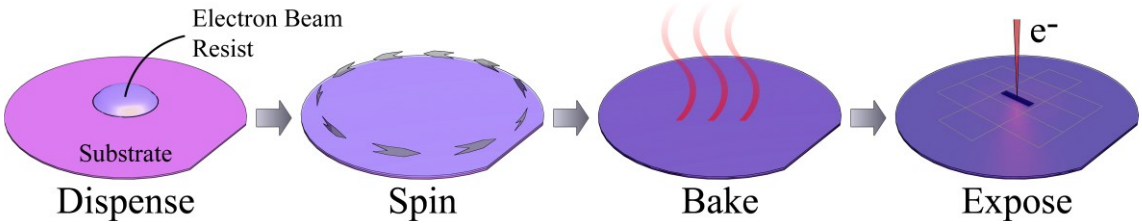

Figure 26: Process for the preparation of spin-coated substrates prior to lithography.

The patterned substrate is then developed using an appropriate developer for an optimized development time. Under-developing leaves resist residue behind, while over-developing results in unintended excess removal of resists. Consistent and gentle agitation of the substrate in a pool of developer solution is essential to ensure that the resist interface is always in contact with fresh developer. Negative and positive tone resists react differently upon exposure, and the development outcome is shown in **Figure 27**.

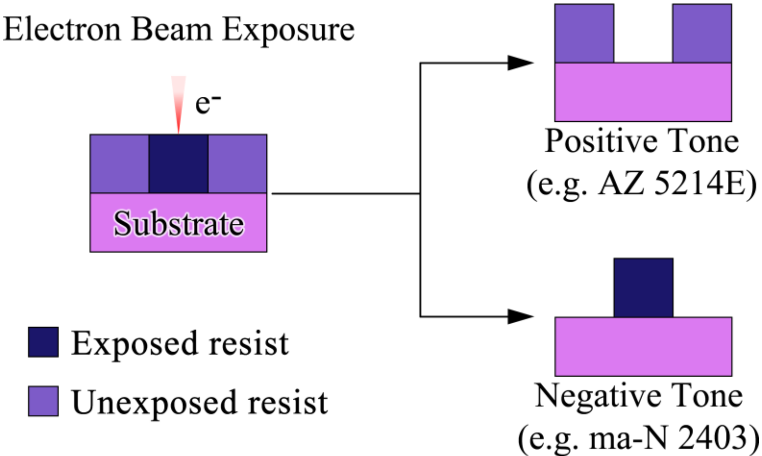

Figure 27: Positive and negative tone resist after electron beam exposure and development.

Resists are typically identified by their product code and can come in various sensitivities, viscosities, and tones. The resist manufacturer's datasheets provide information on optimal process parameters, but a general description for positive and negative tone electron beam resists will be described here. After developing, the resultant features can be checked under the optical microsope, AFM, or SEM to ensure that the dimensions meet expectations. The substrate can then proceed with subsequent processes such as sputtering or ion beam etching (IBE). Stripping or removal of the resist can be performed by soaking the substrate with an appropriate remover solution. Occasionally, the resist can harden due to high temperature processes. However, in general, a warm remover solution bath with intermittent ultrasonic agitation can help improve the removal of the remaining hardened resist.

4.1.4 Ion Beam Etching

Removal of material can be performed using an IBE tool (also known as ion milling). IBE is an anisotropic etching technique with similarities to sputtering. Both processes involve accelerated Ar ions used to ablate material off a surface. The IBE system used is the AJA IBE system as shown in **Figure 28**.

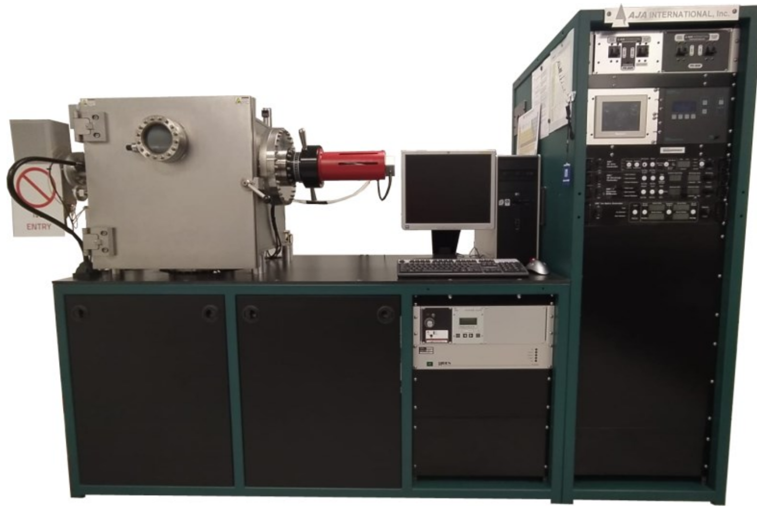

Figure 28: AJA ion beam etching system with a secondary ion mass spectrometer (SIMS) end point detector.

The system uses a Kaufman & Robinson RF-ICP ion source to ionize a high-purity Ar supply, and accelerate the Ar ions through a graphite grid, as illustrated in **Figure 29**. Accelerated Ar atoms ablate the substrate surface to remove material non-selectively. Surfaces exposed to the accelerated Ar flux will be removed, and sacrificial layers such as the relatively thicker EBL-patterned resist are used to protect the underlayers. The ion beam angle of incidence can be adjusted and is typically angled at least 10 degrees off-normal in order to minimize redeposition by gently etching the side-walls. The water-cooled sample stage dissipates heat build-up due to the process, and allows constant sample rotation to ensure that the angle of attack is uniform on all sides of the feature to prevent shadowing effects.

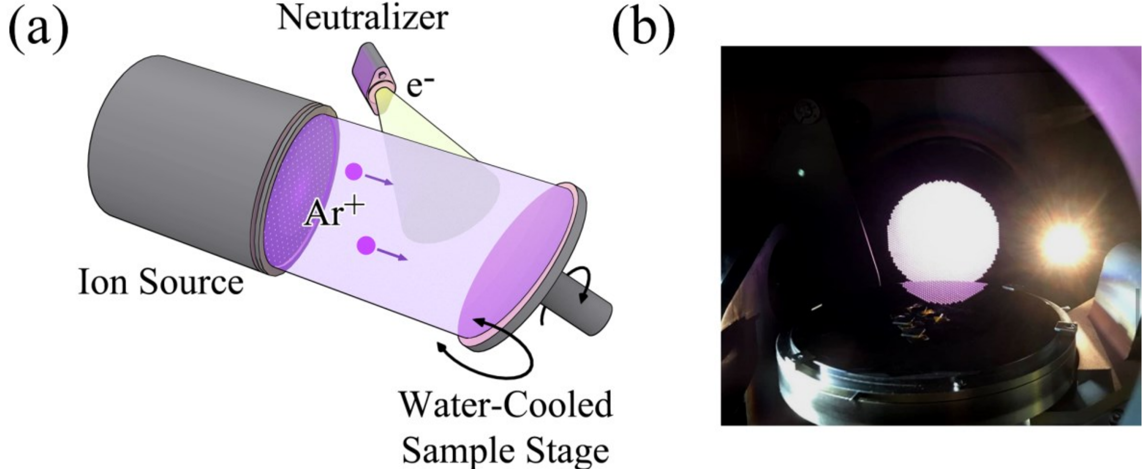

Figure 29: (a) Directional Ar ion beam incident on a tilted and rotating water-cooled sample stage. A neutralizer eliminates charge build up on the substrate surface. (b) Active Kaufman and Robinson Ar ion source straight-on with neutralizer (bright glow on the right).

Within the chamber, a secondary ion mass spectrometer end point detector (SIMS-EPD) is used to detect etched materials. The SIMS-EPD cycles through a user-specified range of atomic mass units and plots a graph of the intensity of detected elements over time. Using this detection method, the IBE process can be stopped when a specific layer is reach. The IBE process is completed when the required materials are removed. Residual resist is then stripped off using an appropriate remover.

4.2 Characterization Techniques

Several magnetic and electrical characterization techniques on blanket films and devices are discussed in this section. Measurement is typically automated and controlled using LabVIEW.

4.2.1 Surface Resistance and Resistivity

The surface (sheet) resistance and resistivity of thin films provide a way of determining how electric currents shunt along multilayers comprising different materials with different electrical properties. The surface resistivity can be measured on continuous blanket thin films without the need for device patterning

by using an in-line four-point probe, as shown in **Figure 30** (a). The set up uses pogo pins to provide Ohmic point contacts with the thin film surface. The four-point probe is custom built, with probe pins equally spaced by $s = 2$ mm apart. The outer pin pair sources current and the inner pin pair measures the potential difference ΔV between them. The four-probe set up is used to negate the effects of wire and contact resistance, so that ΔV across the inner two probes are entirely due to potential difference within the sample. The four-probe measurement set up uses a Keithley 2400 series source-measure unit.

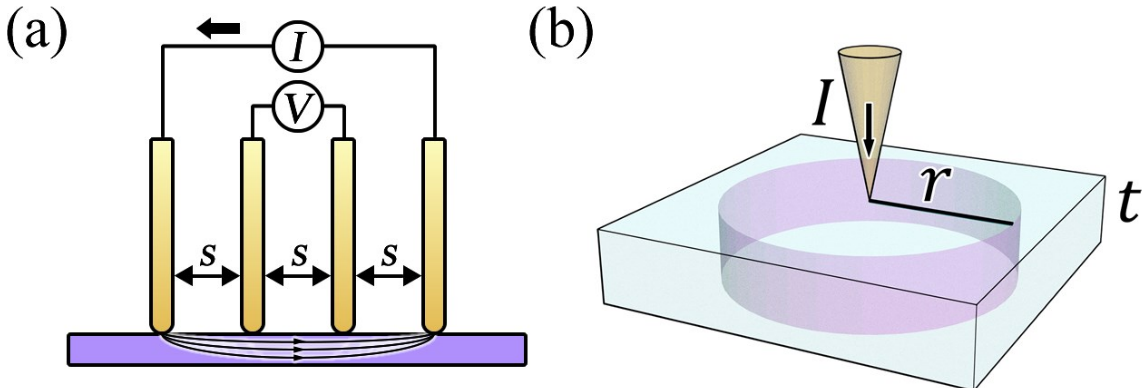

Figure 30: (a) Schematic of four-point probe configuration on a thin conductive layer. (b) Current injection from a probe into a thin conductive layer.

There are several requisites for measuring sheet resistance across a blanket film reliably and without the need for geometrical correction factors: i) The probe pins are at the centre of the film, ii) the length and width of the thin film is significantly larger by at least 40 times than the probe spacing, and ii) the film is no thicker than 40% of the probe spacing. The first two requisites ensure that the current paths are not limited by the proximity to the sample edges that can lead to overestimation of the sheet resistance. The last requisite will be used to approximate the current injection in the thin film as a cylinder, rather than a hemisphere.

The measurements cannot simply be extracted from the measurement tool. In the case of thin films with thickness t, an arbitrarily sharp probe tip

injecting current through Ohmic contact with the thin film is illustrated in **Figure 30** (b). The current density is then $J = I/2\pi rt$. Applying Ohm's law where the electric field across each cylindrical shell is given by $E = \Delta V/\Delta R = \rho J$, where ρ is the material resistivity, we obtain the following relation:

$$\frac{dV}{dr} = -\rho(\frac{I}{2\pi rt}) \tag{47}$$

Integrating from r to r'

$$V - V' = \frac{IR_s}{2\pi}(\ln r' - \ln r) \tag{48}$$

With $t \ll s$, the potential difference between the inner probe pair is then

$$\Delta V = \frac{IR_s}{2\pi}(2\ln 2s - 2\ln s) = \frac{IR_s}{\pi}\ln 2 \tag{49}$$

The sheet resistance in Ω/□ is then

$$R_s = \frac{\pi}{\ln 2}\frac{\Delta V}{I} \approx 4.532\frac{\Delta V}{I} \tag{50}$$

4.2.2 Vibrating Sample Magnetometer

The LakeShore 8604 vibrating sample magnetometer (VSM) shown in **Figure 31** is used to characterize the magnetic properties of magnetic materials, from which information such as coercivity, remanence, anisotropy field, and saturation magnetization can be extracted. It comprises of a model 643 bipolar magnet power supply capable of delivering up to ± 70 A to the EM-4V electromagnet. Both the power supply and electromagnet are water-cooled to keep the system at a safe operating temperature. The pole diameter is 100 mm and the pole cap face diameter is 50 mm, providing a uniform field across the device. With a pole gap distance of 16 mm, a maximum field of about 2 T can be achieved. The sensitivity of a VSM is particularly dependent on several factors

related to the electronics, pick-up coils, mechanical drives, the environment, and other sources of noise.

A VSM operates by vibrating a sample vertically at a constant frequency. The sample is adhered to the end of a non-magnetic rod, and the rod is positioned such that the sample oscillates in between pole pieces of an electromagnet. The sample vibrating in the magnetic field causes variations in the magnetic flux, and consequently induces an AC voltage in the pickup coils due to Faraday's law. The vibrating frequency is also fed to a lock-in amplifier as reference, in order to detect and measure the induced voltage that is proportional to the magnetic moment of the sample. The correlation between the induced voltage and magnetization is calibrated using a reference Ni sphere rated 6.92 emu at 5 kOe. A maximum field of about 2 T can be achieved with a pole gap distance of 16 mm.

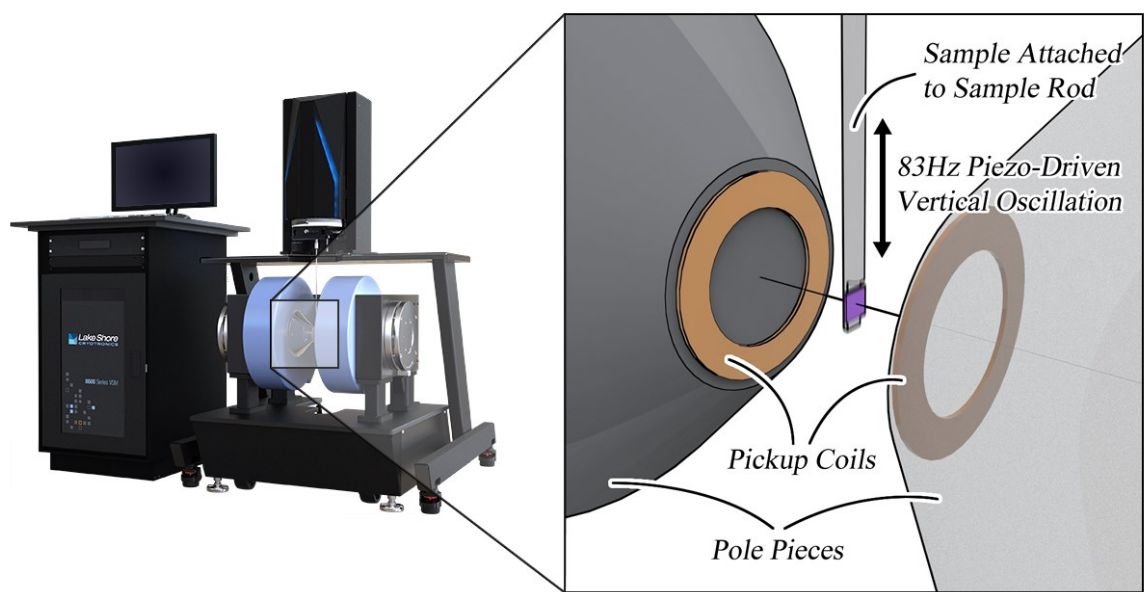

Figure 31: Vibrating sample magnetometer with close up illustration of vibrating sample-mounted rod between pick-up coils mounted on each pole face.

4.2.3 DC Measurements

DC measurements can be performed using a source-measure unit (SMU) such as the Keithley 2400 series in one of two modes: (i) 2-wire sensing and (ii)

4-wire sensing. In 2-wire sensing, sourcing current I_{dc} and measurement take place along the same circuit shown by the red wire connecting the two points of the device under test (DUT) as illustrated in **Figure 32**(a) and (b). The voltage and resistance measured are referred to as $V_{xx} = I_{dc}R_{xx}$, where the subscript indicates the source and measure axes. The 2-wire sense method is used to measure the device resistance including any contact and wire resistance as well as anisotropic magnetoresistance (AMR).

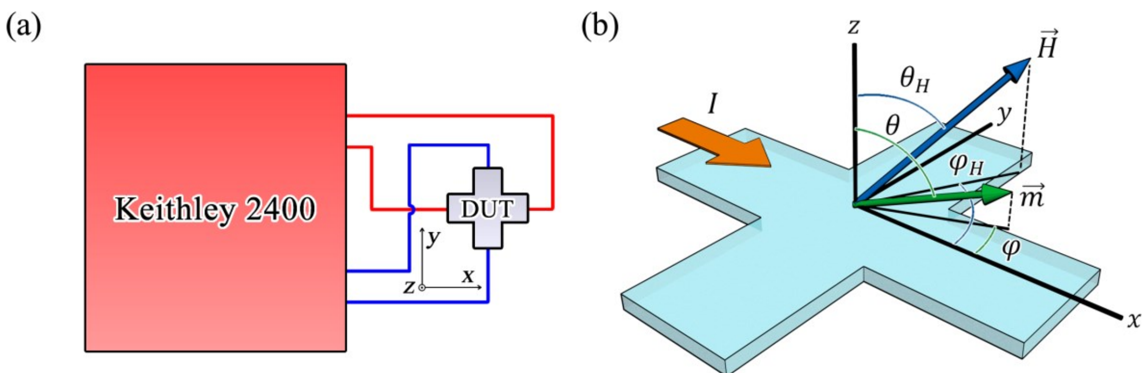

Figure 32: (a) Measurement set up with a Keithley 2400 series source-measure unit. (b) Schematic of device with polar θ and azimuthal φ angles of magnetization $\vec{m}$, and polar θ_H and azimuthal φ_H angles of effective field $\vec{H}$. I represents the flow of current along x-axis.

In 4-wire sensing, current I_{dc} is sourced from the unit along the red wire and delivered along the device in the x direction, and the potential difference measured along the blue wire connected to the transverse conductor in the y direction given by $V_{xy} = I_{dc}R_{xy}$. Here, the subscript represents the source and transverse measures axes. The 4-wire sense negates any contact resistance, and purely measures the potential difference across the points of contact. It is also used to accurately measure the resistivity of thin films using the in-line four-point probe method. In a magnetic sample, the anomalous Hall resistance can be measured across the transverse Hall bar due to the anomalous Hall effect. DC Hall measurements are useful for electrically probing the magnetization state in perpendicularly magnetized Hall cross devices. The anomalous Hall voltage V_H

measures the perpendicular component of the magnetization $m_z = \frac{\vec{m}}{M_s}\cos\theta$, where θ is the magnetization polar, and is given by:

$$V_H = I_{dc}\Delta R_H \cos\theta \tag{51}$$

Figure 33 shows the plot of R_H in a sweeping IP (H_x) and OOP (H_z) field using the single domain Stoner-Wohlfarth model and the following parameters for a perpendicularly magnetized thin film such as in the MgO/CoFeB bilayer [132]: saturation magnetization $M_s = 1200\ \text{emu/cc}$, OOP uniaxial anisotropy $k_1 = 4.2 \times 10^5\ \text{J/m}^3$.

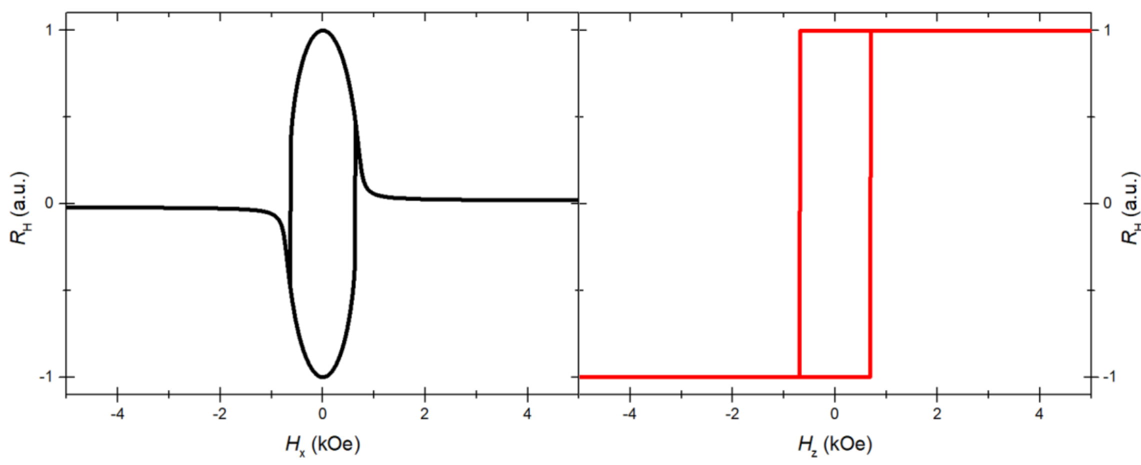

Figure 33: Exemplary plots of anomalous Hall resistance $\boldsymbol{R_H}$ in a device with PMA (a) in a sweeping IP field $\boldsymbol{H_x}$, (b) and a sweeping OOP field $\boldsymbol{H_z}$.

Where angular dependent measurements are required, a custom-made Arduino-controlled stepper mount is used to reliably and repeatably rotate the sample for θ-dependent or φ-dependent measurements.

4.2.4 Harmonic Hall Measurement

The harmonic measurement technique is used to quantitively determine the SOT efficiency. The harmonic measurement set-up and device schematic is shown in **Figure 34** (a) and (b), respectively. The adiabatic AC current is provided by a Keithley 6221 AC/DC, and a Signal Recover 7265 lock-in amplifier measures both first and second harmonics simultaneously. Aside from

these two pieces of equipment, an external magnetic field is provided by a LakeShore EM4 electromagnet, a custom-made aluminium air-core electromagnet, and other supporting custom-made tools such as a stepper-mounted sample holder for automating angular-dependent measurements. The magnetic field near the sample is measured using a Hirst GM08 gaussmeter. All the equipment are connected to a Windows computer via GPIB or USB, and the measurement operates using LabVIEW. The analytical derivation for harmonic measurement is discussed in **Appendix A**.

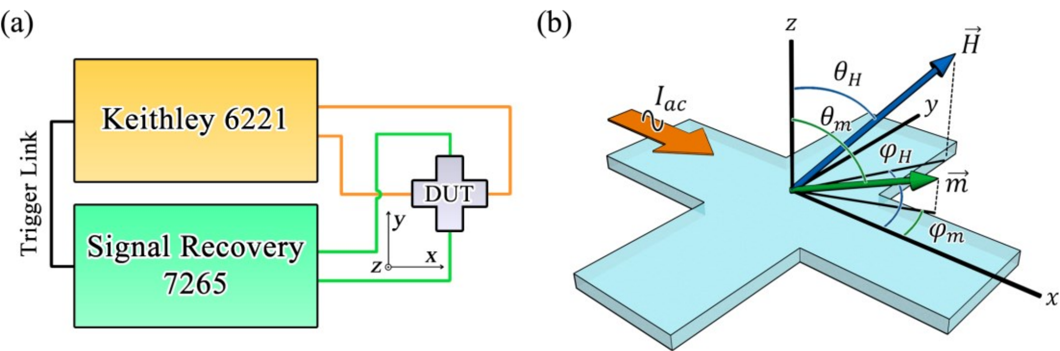

Figure 34: (a) Harmonic measurement set-up comprising an AC/DC source and a lock-in amplifier. (b) Device schematics with magnetization and field polar and azimuthal angles.

The AHE (or EHE) is a magnetotransport effect, commonly used to measure the degree of perpendicular magnetization in a device with Hall cross geometry. R_{xx} is the longitudinal resistance when measured along the same arm as the current flow, and R_{xy} is the transverse resistance when measured along the arm perpendicular to the current flow, such that

$$R_{xy} = \frac{V_{xy}}{I} = R_0 H + R_{AHE} M_z \quad (52)$$

where V_{xy} is the transverse (Hall) voltage that comprises of the ordinary Hall and anomalous Hall contributions, R_0 is the ordinary Hall effect coefficient, and R_{AHE} is the AHE coefficient. The AHE is a consequence of SOC, and originates from

two types of scattering mechanisms – skew scattering and side-jump [133,134]. The Hall voltage is related to a Hall electric field by

$$V_{xy} = E_{xy}\ell = \rho_{xy} l j \tag{53}$$

The longitudinal voltage is

$$V_{xx} = \rho_{xx} L j \tag{54}$$

The ratio between V_{xy} and V_{xx} then gives

$$\frac{V_{xy}}{V_{xx}} = \frac{\rho_{xy}}{\rho_{xx}}\frac{\ell}{L} = \theta_{SH}\frac{\ell}{L} \tag{55}$$

where θ_{SH} is a dimensionless parameter called the spin Hall angle, and describes the percentage of electrons that deviate from the longitudinal electric field due to the material property.

4.2.5 Kerr Microscopy

In order to visually observe the magnetization and spin structures and patterns in magnetic thin films and devices, the MagVision Kerr microscope as shown in **Figure 35** (a) is used. The system utilises the Kerr effect and is able to resolve sub-micron features. In the Kerr effect, the polarization of light reflecting off a magnetic surface is rotated. By passing the reflected light through a polarizer, the degree of rotation of polarization can be detected. While the system is not used to quantify the magnetization in the sample as would a VSM, it can be used to measure the magnetic hysteresis loop as well as image magnetic domains.

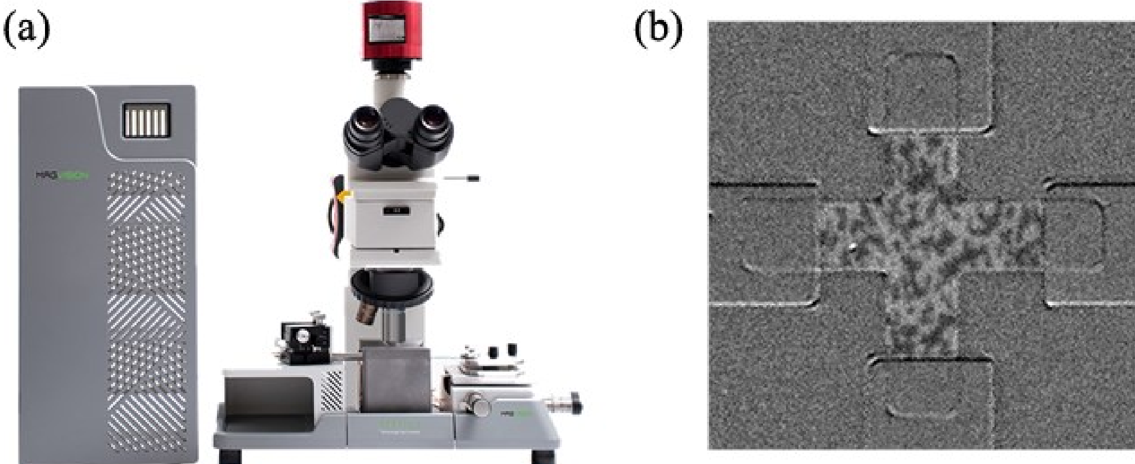

Figure 35: (a) MagVision Kerr microscopy system. (b) Kerr image of the Demagnetized state of a magnetic sample.

In order to capture the magnetization state in a magnetic thin film or device, differential imaging technique is used. In this technique, the magnetization is first saturated in one direction using an external magnetic field, and an image of this reference state is captured. The difference between subsequent images and the reference image is then used to generate a high-contrast Kerr microscopy image such as that shown in **Figure 35** (b). The setup comprises of in-plane or out-of-plane electromagnets, and a custom-made sample holder for wire-bonding devices that enable *in situ* electrical measurements.

Chapter 5

Spin-Orbit Torque Induced Multi-State Magnetization Switching in Hall Cross Structure at Elevated Temperatures

In practical device applications, spintronic devices such as the 1T1MTJ STT-MRAM are subjected to thermal effects due to heat dissipation from adjacent transistor operations as well as due to the ambient temperature. An increase in operating device temperature can lead to lower TMR, reduced critical switching current, and shrinking read margin that allows the circuitry to distinguish between high and low resistance states. With devices that exhibit an analogue-like response or multi-state behaviour, more than one bit can be stored in each cell. However, thermal effects become more critical in device operation. In this chapter, we explore the effect of elevated temperature on a spin-orbit torque driven Hall cross device with multi-state behaviour. Parts of this chapter have been published in **Journal of Magnetism and Magnetic Materials** [135].

5.1 Motivation

There has been a lot of attention given to the generation of spin current for SOT driven magnetization switching in HM/FM heterostructures recently, both for the understanding of the underlying physics as well as for device applications. Spintronic devices that rely on SOT for magnetization switching have the advantage of omitting an additional ferromagnetic layer for spin polarization of conduction electrons as required in the conventional STT effect. The origin of SOT is due to the strong SOC via the SHE [107,124], and/or the Rashba effect in HM [136-142]. The effective SOT acting on local magnetization in a FM is dependent on structural inversion asymmetry (SIA), and can be

achieved by sandwiching the FM between layers of dissimilar materials or thicknesses. Since its discovery, magnetization manipulation by SOT has been of great interest for fast domain wall propagation [143-145], efficient magnetization switching [124,129,142], as well as for sustaining steady state excitation in ferromagnetic nanostructures [146,147].

Recently, Kurenkov *et al*. have reported magnetization manipulation in devices using current-driven SOT, with analogue switching behaviour characterised by the intermediate resistance states, for device dimensions larger than the magnetic domain size [70]. Such SOT devices show promise in applications of neuromorphic engineering due to their non-volatile analogue-like behaviour [30,148-151]. When integrated with CMOS, spintronic devices will be subjected to thermal effects due to thermal dissipation from electronic transistor operations. While binary MTJs can afford large read and write margins [152,153], the impact of elevated operating temperature on SOT-driven devices with multi-state behaviour remains unexplored.

In this chapter, we demonstrate the analogue-like, multi-state characteristics in a Co/Pt multilayer Hall cross device. Using *in-situ* Kerr microscopy, the intermediate resistance states due to the formation of magnetic domains across the device are captured. The multi-state behaviour is shown to be attributed to an inhomogeneous current density profile across the device junction. The effects of current-induced SOT magnetization switching from room temperature (RT = 295 K) to 360 K on the change in Hall resistance ΔR_H across varying IP bias fields H_x are summarised in switching phase diagrams.

5.2 Experimental Details

A multilayer comprising Ta (5)/Pt (3)/[Co (0.6)/Pt (0.6)]$_4$/Co (0.6)/Ta (5) was sputter-deposited on to thermally oxidised Si substrates. Numbers in parenthesis indicate nominal film thicknesses in nanometers, and the subscript represents the number of [Co/Pt] bilayer repeats. Vibrating sample magnetometry

measurements on a 5 mm by 5 mm blanket film in out-of-plane (OOP; red curve) and in-plane (IP; black curve) sweeping fields show that the multilayer film exhibited perpendicular magnetic anisotropy (PMA) as plotted in **Figure 36** (a). The inset shows the blanket film OOP hysteresis loop with coercivity $H_c \approx$ 300 Oe. Subsequently, Hall crosses of 50 μm by 5 μm wires were patterned using electron beam lithography and Ar ion beam etching techniques. Electrical contacts were patterned and deposited over the ends of each wire as shown in **Figure 36** (b). The device channel along the x direction is distinguished from the transverse Hall bar along the y direction.

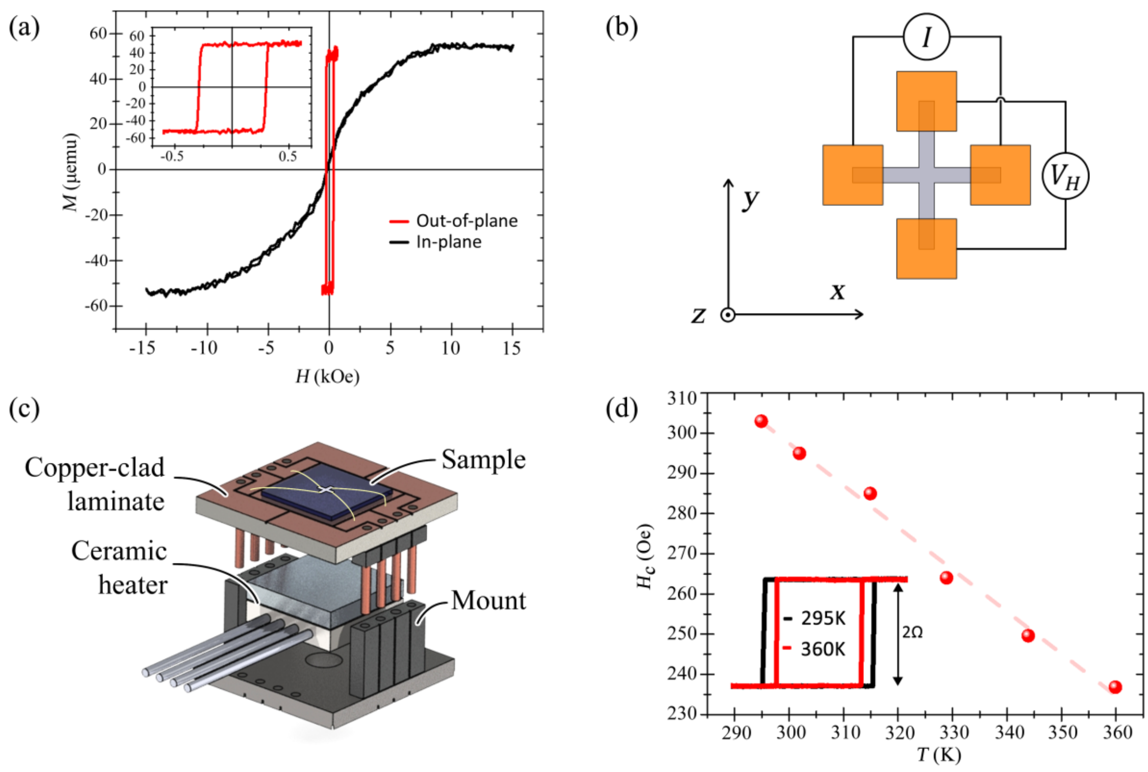

Figure 36: (a) In-plane and out-of-plane hysteresis loops obtained via vibrating sample magnetometry. Inset shows the zoomed-in out-of-plane hysteresis loop. (b) Device schematic with current delivery along the $\boldsymbol{x}$ direction, and Hall voltage measurement along the $\boldsymbol{y}$ direction. (c) Sample mount for in-situ temperature control. (d) Device coercivity from 290 K to 360 K.

Sample heating was achieved using a custom-made mount as illustrated in **Figure 36** (c). A square ceramic heater of width 12 mm with built-in thermocouple was connected to a PID controller to regulate the power and heater

temperature. A copper-clad laminate (CCL) on to which the substrate was mounted, contacted the exposed aluminium surface from the underside. For calibration, a separate thermocouple was placed on a mounted dummy Si substrate. The heater and substrate surface temperatures were correlated to map the temperature values. The time required to reach steady-state temperature at the substrate surface was accounted for. Using this custom mount, electrical characterization of the device can be performed under varying device temperatures. The device magnetization was measured by applying a non-perturbing probing current $I_{probe} = 200$ µA along the wire in the x-axis, and measuring the anomalous Hall resistance $R_H = V_H/I_{probe}$ along the Hall bar transverse to the current flow. The anomalous Hall resistance R_H is a measure of OOP magnetization. The coercivity H_c from 295 K to 360 K is plotted in **Figure 36** (d) and shows a monotonic decrease in H_c with increasing device temperature T. The inset shows the hysteresis loops at both extremes of the temperature range. While it is expected for the saturation magnetization M_s to decrease with increasing temperature, there was no discernible decrease in R_H for device temperatures from 295 K to 360 K.

5.3 Multi-State Behaviour by Current-Induced Spin-Orbit Torque Magnetization Switching

In order to study the magnetization switching due to current-induced SOT, R_H is plotted against write pulse current amplitude I_{ch} along the device channel. Each measurement loop begins with an initialization pulse $I_{init} = -24$ mA to set a reference magnetization state. Subsequently, 1 ms write pulses I_{ch} up to $+24$ mA in steps of 1 mA are delivered. Between each write pulse, the magnetization state of the device is probed using a non-perturbing probing current $I_{probe} = 200$ µA, and the transverse Hall voltage $V_H = R_H/I_{probe}$ is measured. Throughout the entire write-and-measure sequence, the device is subjected to a static IP field $H_x = 1$ kOe along the x direction and parallel to the current flow.

The IP field H_x serves to break the switching symmetry required for deterministic SOT switching in devices with perpendicular magnetic anisotropy [154].

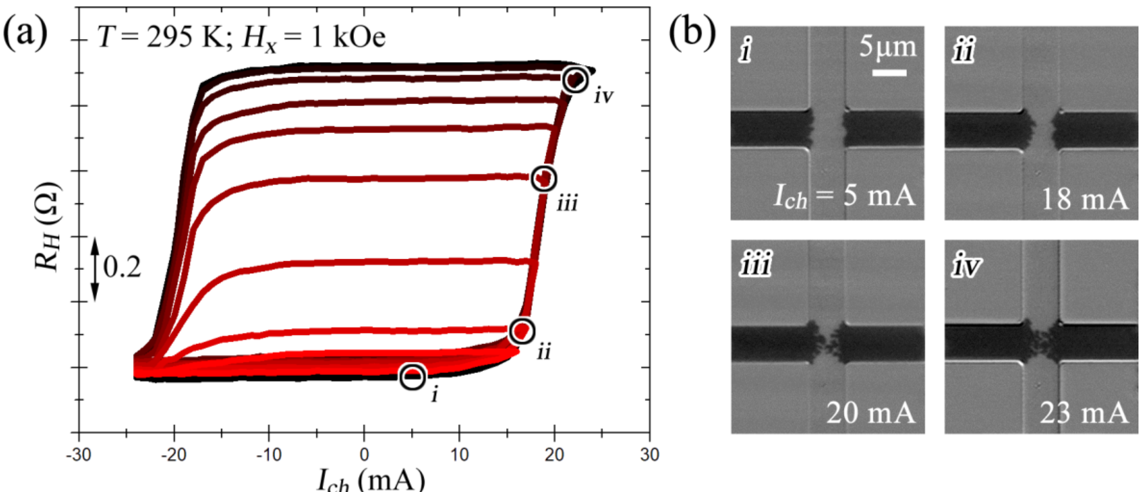

Figure 37: a) $R_H - I_{ch}$ loops at RT (295 K), showing intermediate resistance states, and (b) in-situ Kerr microscopy images of the device magnetization configurations at various I_{ch} corresponding to respective Hall resistances R_H.

Figure 37 (a) shows the $R_H - I_{ch}$ loops up to varying current amplitudes measured at RT (295 K). From approximately $I_{ch} = 10$ mA, intermediate Hall resistance states can be achieved, and the device exhibits multi-state behaviour. The Hall resistance R_H appears to saturate at $I_{ch} = I_{sat} = \pm 24$ mA. **Figure 37** (b) shows the *in-situ* Kerr microscopy images, revealing the device magnetization configurations at current amplitudes of 5 mA, 8 mA, 20 mA, and 23 mA. It is also observed that the change in Hall resistance ΔR_H for current-induced SOT switching is smaller than that as compared to the OOP field H_z swept hysteresis loop, which can be attributed to partial magnetization switching at the device junction in the former case.

Due to the geometry of the Hall cross device, the multi-state switching behaviour may be a result of inhomogeneity of the current-induced SOT across the device. In order to obtain an accurate current density profile across the device, finite element simulation was used to model current flow along the Hall cross channel. **Figure 38** (a) shows the inhomogeneous current density profile across

the Hall cross device due to a current I_{ch} along the device channel of width 5 μm. A 0.5 μm fillet at the junction corners mimic the rounded corners of the patterned device. Current shunting across the junction is a result of the device geometry.

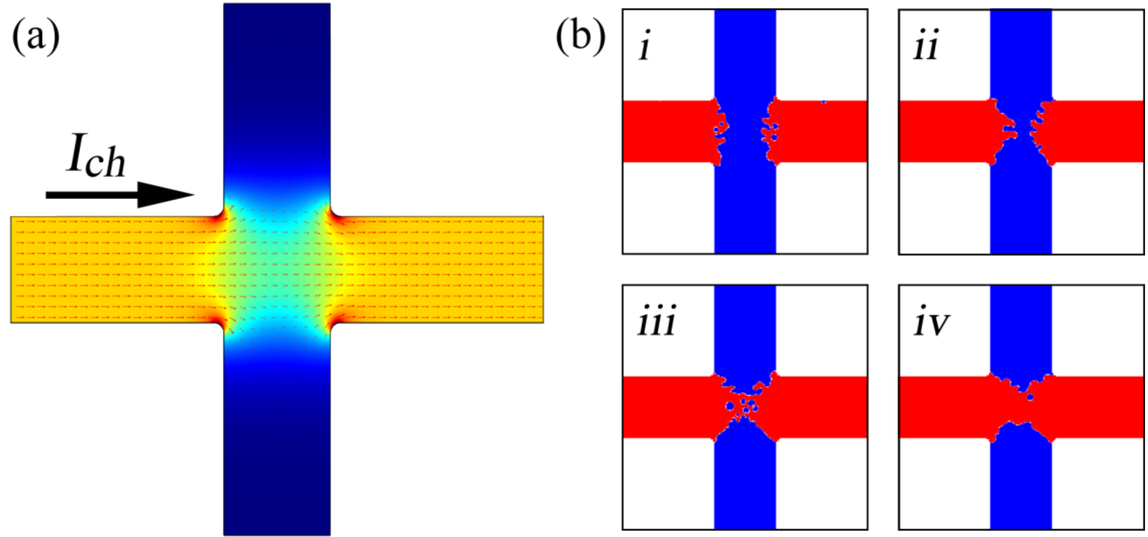

Figure 38: (a) Current density profile across a Hall cross due to current I_{ch} along the device channel. Lateral shunting of the current at the device junction results in an inhomogeneous current density. (b) Magnetization configuration across the device with increasing effective out-of-plane magnetic field.

The progression of magnetization switching in a Hall cross structure was then simulated in Mumax3 using the current density profile [155]. The magnetic material parameters used are $M_s = 7.6 \times 10^5$ A m^{-1}, $K_u = 3.8 \times 10^5$ J m^{-3}, and $A_{ex} = 1.5 \times 10^{-11}$ J m^{-1} [156-158]. By mapping the current density profile as an effective OOP field $H_{z,eff}$, similar magnetization switching behaviour was observed. Snap shots for increasing current density and corresponding magnetization configurations are shown in **Figure 38** (b).

5.4 Effect of Elevated Device Temperature on Reading and Writing

It is critical to understand how thermal effects can affect magnetization switching due to current-induced SOT, as well as the temperature-dependent magnetic properties of materials and devices. To study the temperature-dependence of ΔR_H due to CIMS, the $R_H - I_{ch}$ measurement sequence was

repeated at varying temperatures up to 360 K. **Figure 39** (a) shows ΔR_H and critical switching current I_{sw} from RT to 360 K in the presence of IP field $H_x =$ 2.8 kOe. Here, I_{sw} is defined as the current at which ΔR_H changes by 50%. At room temperature, I_{sw} is 24 mA and drops to 18 mA when the device temperature is increased up to 360 K. While the device shows monotonic decrease in I_{sw} with increasing temperatures, ΔR_H is observed to increase up to 340 K due to weakened anisotropy, lowering the energy barrier between states and resulting in thermally-assisted current-induced SOT switching. Further increase in temperature beyond 340 K results in a decrease in ΔR_H, revealing that some of the magnetic domains may have substantially weakened anisotropy to the point where much of the perpendicular magnetization is not sustained under the IP field. By varying both H_x and T, a phase diagram describing the switching behaviour of the devices is obtained as shown in **Figure 39** (b). The polarity of I_{ch} and H_x results in LRS-to-HRS or HRS-to-LRS loops. A large H_x is required for CIMS in highly anisotropic Co/Pt multilayer systems and can be observed in the region of red of the phase diagrams where the largest ΔR_H is achieved. For $H_x < 0.28$ T, ΔR_H generally increases with T. Throughout the T-dependent measurements, $R_H - H_z$ loops were performed to confirm that there were no irreversible changes to the magnetic properties of the device due to the combined effects of thermal and Joule heating.

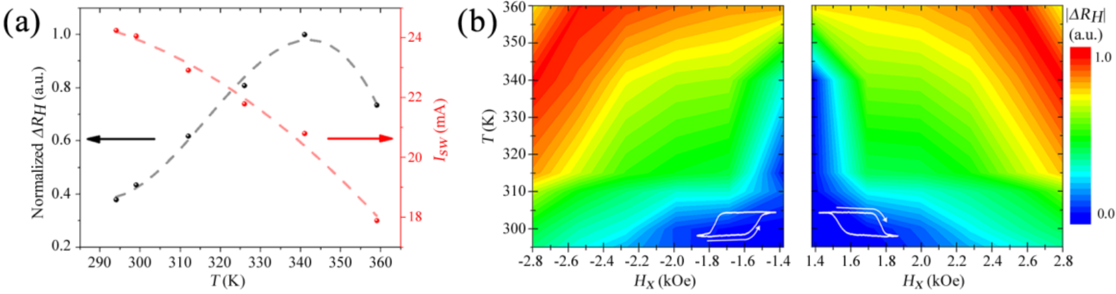

Figure 39: (a) Thermally-assisted switching at 2.8 kOe results in monotonic decrease in switching current I_{sw} with increasing temperature T. The change in Hall resistance ΔR_H peaks at 340 K as the reduced anisotropy is unable to sustain a fully OOP magnetization above that temperature. (b) Phase diagrams across

varying IP fields show ΔR_H due to 1 ms write pulses across varying IP bias field H_x.

5.5 Effective Out-Of-Plane Field Due to Current-Induced Spin-Orbit Torque at Elevated Temperature

To quantify the SOT efficiency of the device at room and peak T, the $H_{z,eff}$ due to I_{ch} at RT and 360 K was determined. For this measurement, a calibrated air-core electromagnet was used to provide a sweeping H_z field are shown in the schematic **Figure 40** (a). The sample was located at the centre of the air-core electromagnet during measurement. The Hall resistance R_H in a scanning OOP field H_z was measured at varying channel currents I_{ch} and IP field H_x. The loop shifts for $I_{ch} = \pm 12$ mA with their loop centres displaced due to opposite current polarities is shown in **Figure 40** (b). The vertical offsets are for clarity. **Figure 40** (c) shows the depinning fields for down-to-up (blue dots) and up-to-down (red dots) switching transitions across a range of I_{ch} from −12 mA to +12 mA. The loop shift (black dots) determined from the depinning fields (zero-crossing) is defined to be the effective field $H_{z,eff}$ at the respective H_x. The set of loop shifts at $H_x = \pm 10$ mT clearly shows that the loop shift is dependent on the current polarity as shown in **Figure 40** (d). Here, a linear fit approximates the efficiency χ. This measurement is performed across $H_x = \pm 1$ kOe at RT and 360 K. The χ versus H_x is plotted in **Figure 40** (e) and (f) for RT and 360 K, respectively. At RT, $\chi_{sat}(\mathrm{RT}) \approx 74\ \mathrm{Oe}/10^{11}\ \mathrm{A\,m^{-2}}$, comparable to reported values in single Pt/Co and Pt/CoFeB stacks [116]. At $T = 360$ K, the value of $\chi_{sat}(360\ K) \approx 55\ \mathrm{Oe}/10^{11}\mathrm{Am^{-2}}$. The relationship between χ and the SHA θ_{SH} of the HM layers is given by $\chi_{sat} = \frac{\pi}{2}\frac{\theta_{SH}\hbar}{2eM_s t_{FM}}$, where ħ, e, M_s and t_{FM} are the Planck's constant, electron charge, saturation magnetization, and FM layer thickness, respectively [159]. The SHA of Pt θ_{SH}^{Pt} has been reported to be largely invariant with temperature up to 400 K [160-163]. However, the damping-like

efficiency of Ta ξ_{DL}^{Ta} has been reported to decrease monotonically with increasing temperature from 300 K [164]. The damping-like efficiency ξ_{DL}, spin Hall angle θ_{SH}, and SOT efficiency χ_{sat} are figures of merit that scale with each other [116,162]. Therefore, the decrease of χ_{sat} by 26 % from 295 K and 360 K can be attributed to the corresponding decrease in ξ_{DL}^{Ta} and θ_{SH}^{Ta} at higher device temperatures.

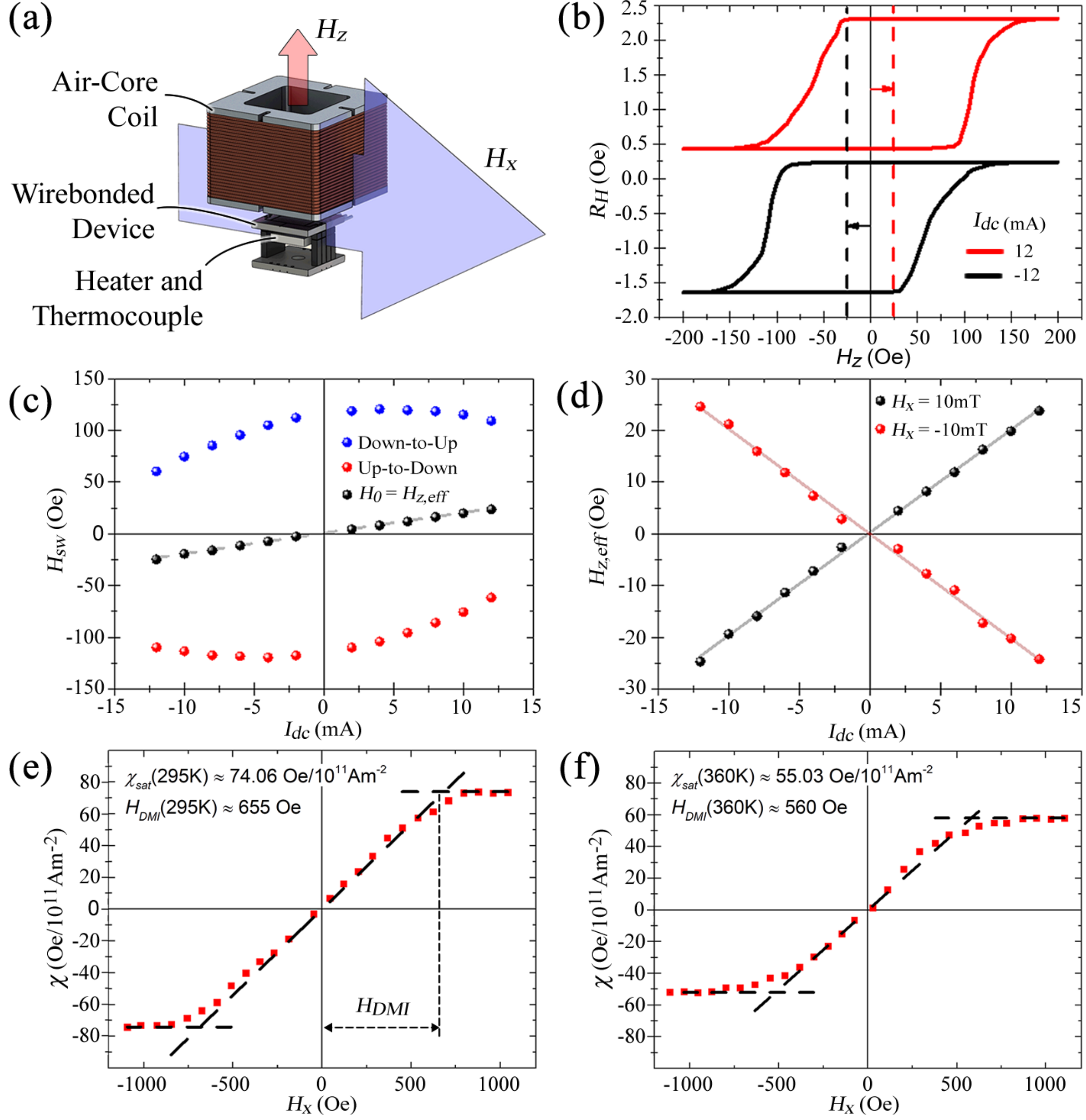

Figure 40: (a) Schematic of measurement set-up showing heater with integrated thermocouple, and air-core coil providing an OOP magnetic field H_z. A larger electromagnet (not shown) provides an IP H_x field. (b) $R_H - H_z$ loop at RT for $H_x = 0.1$ T and $I_{probe} = \pm 12$ mA showing shifts in loop centers. Vertical offset

is for clarity. (c) Loop shift (black dots) due to I_{probe}. (d) Loop shifts due to bias fields of opposite polarity. Effective field χ for (e) $T = RT$ and (f) $T = 360$ K.

Figure 40 (e) and (f) show that $|\chi|$ first increases with $|H_x|$ before saturating. This can be described by a current-driven DW propagation model [116,165], in which chiral Néel DWs are stabilized in such PMA multilayer structures in the absence of an external field as illustrated in **Figure 41** (a). However, the application of a spin current due to SHE leads to effective fields $H_{z,eff}$ acting in opposite directions on such homochiral Néel DWs, resulting in shifting DWs but not domain expansion. An external field H_x is required to break the chirality of the DWs in order to promote domain expansion as illustrated in **Figure 41** (b). When the external field is large enough to overcome the effective field due to the DMI, H_{DMI} can be determined.

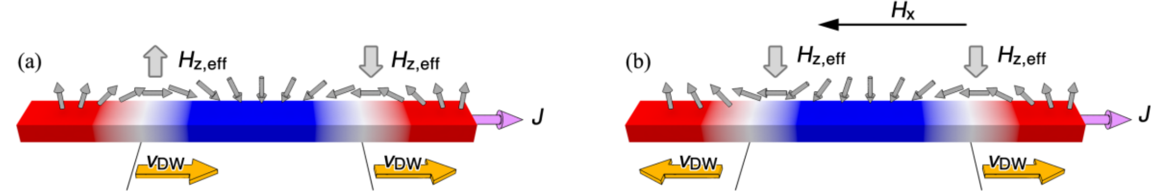

Figure 41: (a) Current-induced effective fields $H_{z,eff}$ acting on chiral Néel domain walls in the absence of an external in-plane magnetic field. (b) Breaking of the DMI-induced DW chirality by applying an external magnetic field H_x. The current-induced effective field $H_{z,eff}$ acts to expand and contract domains.

At both ends of the temperature range, $H_{DMI}(RT) \approx 655$ Oe and $H_{DMI}(360\text{ K}) \approx 560$ Oe. The decrease in H_{DMI} and weakening of DMI strength with increasing T is due to greater thermal disorder [93,166]. The chiral magnetization canting due to DMI can be overcome with smaller IP bias field H_x at higher temperature T.

Multilayer Stack	$\|H_{DMI}\|$ **(Oe)**	**Reference**
Pt (4)/Co (1.2)/Ir (1)	655	Durga Khadka, *et al.* [167]
Pt (4)/Co (1.2)/Ir (2)	813	
Pt (4)/Co (1)/Ir (1)	1300	

Pt (4)/Co (1)/Ru (2)	1404	
Pt (4)/Co (0.8)/Ru (2)	2120	
Pt (4)/Co (0.8)/Ru (3)	2180	
Pt (4)/Co (0.8)/Ru (4)	2386	
Pt (3)/[Pt (1)/Co (0.8)/Ru (1.3)]$_2$	2200	
Pt (4)/Co (1)/MgO (2)	2800	Chi-Feng Pai, *et al.* [116]
Ta (6)/CoFeB (1)/MgO (2)	250	
Ta (3)/CoFeB (1.3)/MgO (1)/Ta (1)	300	Jiangwei Cao, *et al.* [132]
Pt (3)/[Co (0.6)/Pt (0.6)]$_4$/Co (0.6)/Ta (5)	655 (RT = 295 K); 560 (360 K)	This work

Table 2: Comparison table of H_{DMI} values obtained from similar measurement methods. Values of H_{DMI} obtained in this and other works using similar measurement methods of determining χ.

Table 2 compares the H_{DMI} values obtained from other works using the same current-induced loop shift technique [116,132,167]. The [Co/Pt]$_4$/Co multilayer in this work suggests that opposing DMI at the interfaces of each Co layer would interfere. Therefore, the H_{DMI} determined from this measurement method describes only the net effect from the entire multilayer stack.

The intermediate magnetization states are persistent and therefore non-volatile with successive read operations. Bipolar pulse switching followed by successive reads at varying temperatures from RT to 360 K is performed to demonstrate this. At each temperature setpoint, alternating polarities of current pulses are delivered in the presence of an external magnetic field of $H_x = +1$ kOe as shown in **Figure 42** (a). The write pulses are each followed by successive read operations in the absence of the external magnetic field. ΔR_H for each current amplitude at varying temperatures is described in the phase diagram as shown in **Figure 42** (b). At $T =$ RT, more intermediate resistance states are accessible, as indicated by the broadening of the colour map at increasing fields. Elevated temperatures result in a reduction of field required for switching to achieve the same resistance state at $T = RT$ as indicated by the eroding dark blue region.

Even though switching occurs across the range of temperatures, receding red regions indicate that the degree of magnetization switching deteriorates at elevated temperatures.

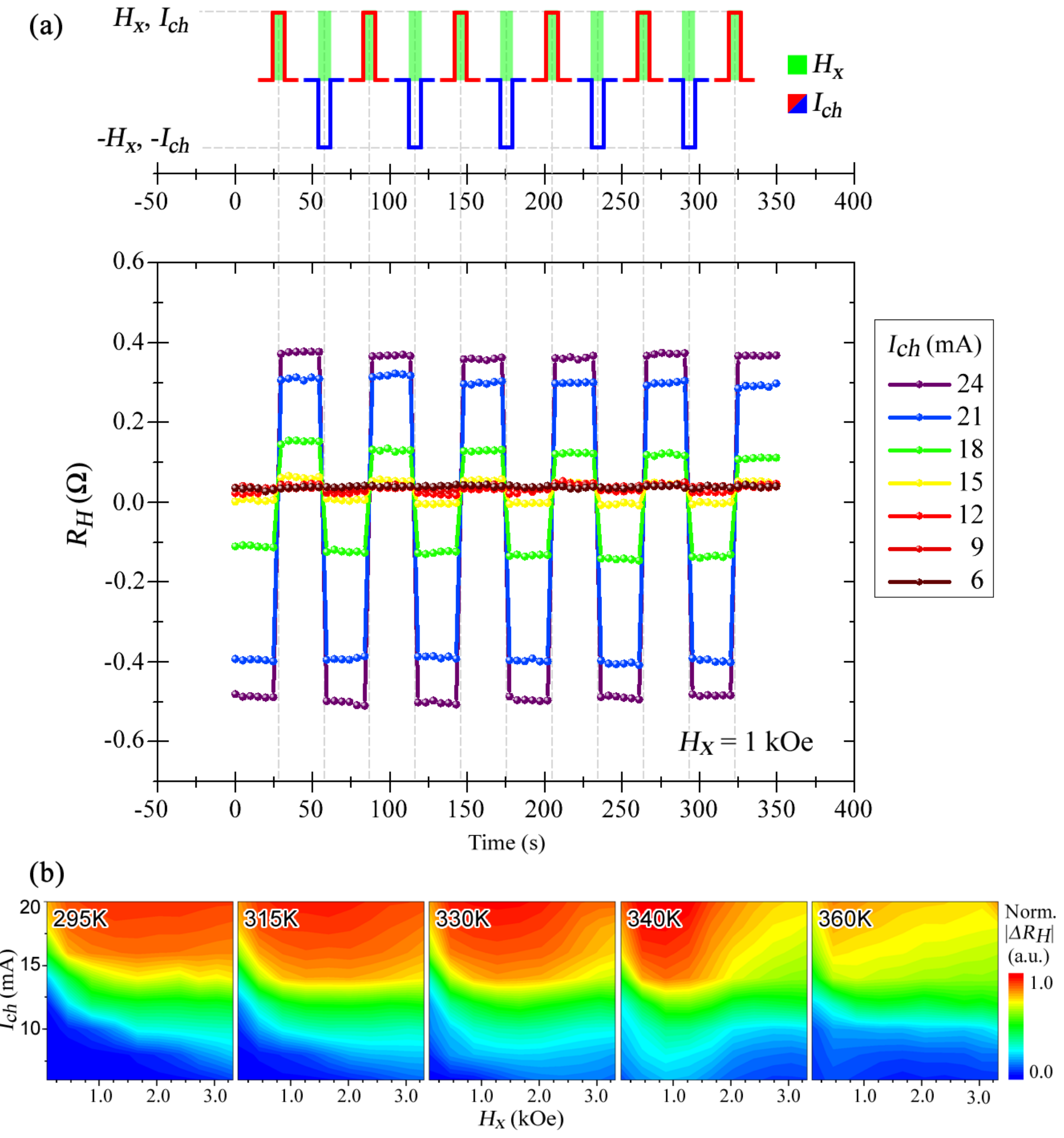

Figure 42: (a) Procedure for multistate write and read involves applying a write pulse I_{ch} in the presence of an IP field H_x. The resistance state is probed with a non-perturbing $I_{probe} = 200$ μA. The procedure is repeated with alternating polarities and amplitudes of I_{ch}. (b) Phase diagram for multistate write and read across varying temperatures T and IP bias field H_x.

The effect of temperature on the reliability of writing and reading a multi-state resistance device may pose a challenge. However, this can be resolved by

using a variation sensing circuit to compensate for a change in device temperature, and perform corrected write and read operations accordingly [153,168,169]. On the other hand, the device can serve as a temperature sensor by utilizing its temperature sensitivity [170]. Under certain write currents, different magnetization states can result from different device temperatures. A threshold used to differentiate between temperature ranges and boundaries can be implemented.

5.6 Conclusion

In summary, SOT-driven multi-state magnetization switching in Co/Pt Hall cross devices were demonstrated for devices operating from RT to 360 K. The multilayer shows strong as-deposited perpendicular magnetic anisotropy. The anomalous Hall resistance scales with current amplitude, and the multi-state characteristic of a current-induced SOT switched device was shown to be due to a geometrically imparted, inhomogeneous current density distribution across the device junction. The current-induced SOT switching was simulated by mapping the current density profile across the device to an effective OOP field. The simulation results closely mimic the device magnetization states as observed through *in-situ* Kerr microscopy imaging at various pulse current amplitudes. When the device was subjected to the temperature range from RT to 360 K, the switching amplitude derived from the change in Hall resistance first increases up to about 340 K before decreasing. While the switching current I_{sw} is inversely proportional to device temperature, the change in high and low resistance states ΔR_H is greatest at 340 K. The effective OOP field per unit current density χ was quantified at RT ($\chi_{sat}(RT) \approx 74\,\mathrm{Oe}/10^{11}\mathrm{Am}^{-2}$) and 360 K ($\chi_{sat}(360\,K) \approx 59\,\mathrm{Oe}/10^{11}\mathrm{Am}^{-2}$). The efficiency, saturation field, and IP field required to overcome the DMI field are reduced at elevated temperatures due to increase in thermal disorder. This work gives additional insight on the effect of elevated temperature on SOT-driven multi-state devices. The challenges imposed by the

temperature sensitivity of multi-state write and read can be resolved with appropriate sensing circuits to monitor and compensate for the temperature variation. Alternatively, the device can serve as a temperature sensor, by exploiting the temperature-dependent current-induced SOT switching.

Chapter 6

Effect of Seed and Interlayer Pt on SOT Efficiency

In this chapter, the SOT efficiency of Ta/Pt/[Co/Pt]$_3$/Co/Pt multilayers with varying seed and interlayer Pt thicknesses are quantified using the adiabatic harmonic Hall measurement technique. The resistivities of the HM layers and corrections for the planar Hall effect are accounted for. The corrected SOT efficiencies show that the SHE is the dominant source of SOT, and that thicker Pt seed layers effectively screen spin current originating from the bottom β-Ta layer. Parts of this chapter have been published in **Journal of Physics D: Applied Physics** [171].

6.1 Motivation

Current-induced SOT magnetization switching has been demonstrated in bilayer systems comprising ultrathin ferromagnet/heavy metal (FM/HM) bilayers such as in Co/Pt systems [172]. A good Pt seed layer with (111) crystallinity allows low lattice mismatch with Co, necessary to achieve as-deposited perpendicular magnetic anisotropy (PMA) with large effective magnetic anisotropy K_u [99,173-176]. These factors favour device scalability and thermal stability $\Delta = K_u V / k_B T$, where V is the magnetic volume, k_B is the Boltzmann constant, and T is the temperature. When a current flows along the bilayer device structure, torques are generated and act on the magnetization, leading to highly efficient magnetization switching [118,172]. As such, current-induced magnetization switching shows great prospects for low-power spintronic memory and logic applications [177,178].

The torques that arise from such structures with inversion asymmetry are due to the spin current originating from the SHE and the effective magnetic field due to the Rashba effect. The sources of SOT and quantification of its efficiency have been studied in various HM/FM bilayer structures [24,124,179]. A parameter used to represent the SOT efficiency is the spin Hall angle θ_{SH}, which represents the ratio of spin current density J_s to charge current density J_c. The HM Pt has been reported to have $\theta_{SH}^{Pt} \approx +0.07$ while Ta has a comparatively larger spin Hall angle with opposite polarity of up to $|\theta_{SH}^{Ta}| = 0.15$ [24,124,179]. HMs with opposite θ_{SH} have also been implemented within multilayer structures. By sandwiching a FM layer with dissimilar HM layers, an increase in the overall SOT efficiency has been demonstrated [180,181]. Current-induced SOT switching is also not limited to a single FM layer. The magnetic volume V can be increased by repeating the [Co/Pt] bilayers without sacrificing PMA [182]. The interaction between SOT and the FM/HM multilayer (ML) is also expected to be commensurate with structural complexity.

In this work, we investigate the effects of seed t_{seed} and interlayer $t_{interlayer}$ Pt thicknesses in Ta/Pt (t_{Seed})/[Co/Pt ($t_{interlayer}$)]$_3$/Co/Ta ML. The interlayer Pt thickness can be used to tune the magnetic anisotropy. Using the adiabatic harmonic Hall lock-in technique, we measure the SOT efficiencies across varying t_{Seed} and $t_{interlayer}$. The [Co/Pt]$_3$/Co is treated as a single FM unit layer, and the current density shunting through the thicker HM layers as well as the planar Hall effect (PHE) contribution is accounted for in quantifying the SOT efficiency. We find that for this stack structure, a thicker Pt layer promotes PMA but screens spin current originating from the bottom Ta layer. Consequently, tuning t_{Seed} and $t_{interlayer}$ is a compromise between PMA and SOT efficiency.

6.2 Experimental Details

Multilayer stacks of Ta (5)/Pt (t_{Seed})/[Co (0.6)/Pt($t_{interlayer}$)]$_3$/Co (0.6)/Ta (5) (nominal layer thicknesses in nanometers) were deposited at room temperature on to thermally oxidized Si wafers with oxide thickness of 300 nm using magnetron sputtering at a base pressure of better than 1.0×10^{-8} Torr. The thickness of the thin films is expected to be relatively uniform based on the deposition system sputter uniformity of better than 3% across a 3-inch diameter substrate. The numerical subscript represents the number of [Co/Pt] bilayer repeats. t_{seed} is the Pt seed thickness from 2 nm to 5 nm in 1 nm intervals, while $t_{interlayer}$ is the Pt interlayer thickness from 0.36 nm to 0.60 nm in 0.12 nm intervals. After deposition, the blanket films were patterned into Hall crosses comprising wires of 5 µm width and 20 µm length using electron beam lithography. Contact pads of Ta (5)/Cu (100)/Ta (5) were deposited for transport measurements.

To characterize the device, the transverse anomalous Hall resistance R_{xy} was measured across a sweeping IP H_x and OOP H_z external magnetic field, using a dc probing current $I_{dc} = 200$ µA along the x axis while measuring the anomalous Hall voltage V_{xy} formed across the y axis. V_{xy} and R_{xy} are related by $R_{xy} = V_{xy}/I_{dc}$. As R_{xy} is proportional to the out-of-plane magnetization component $M_z = \vec{M}\cos\theta$, where $\vec{M}$ is the magnetization vector and θ is the magnetization polar angle, all samples showed square hysteresis in a sweeping H_z indicating PMA [183]. However, in a sweeping H_x, certain devices show the in-plane to out-of-plane remanence R_{xy}^{IP}/R_{xy}^{OOP} at $H_x = 0$ Oe to be below unity. For comparison, the IP hysteresis curves for ($t_{interlayer}$ = 0.36 nm, t_{Seed} = 2 nm) and ($t_{interlayer}$ = 0.36 nm, t_{Seed} = 3 nm) are plotted in **Figure 43** (a) and (b), respectively.

In-situ Kerr microscopy images show that for devices with remanence below unity, dark(bright) domains in an oppositely contrasted magnetic background exist at $H_x = 0$ Oe, indicating a mix of up(down) magnetized domains. For devices with remanence close to unity, Kerr microscopy images show a more homogenous dark or bright contrast across the magnetic material of the devices. Generally, remanence approaches unity with thicker Pt seed layers, which can be attributed to reduced roughness, an improvement to the (111) texture, and subsequent reduction in Co/Pt interfacial roughness [184,185]. **Figure 43** (c) shows R_{xy}^{OOP} for all devices. As the Pt seed layer thickness t_{Seed} increases, its resistance decreases, and more current can shunt through it. This results in less current flowing through the [Co/Pt] multilayer [186]. Furthermore, R_{xy} across devices with $t_{interlayer} = 0.36$ nm and 0.60 nm are almost identical, while devices with $t_{interlayer} = 0.48$ nm have a smaller R_{xy}^{OOP}.

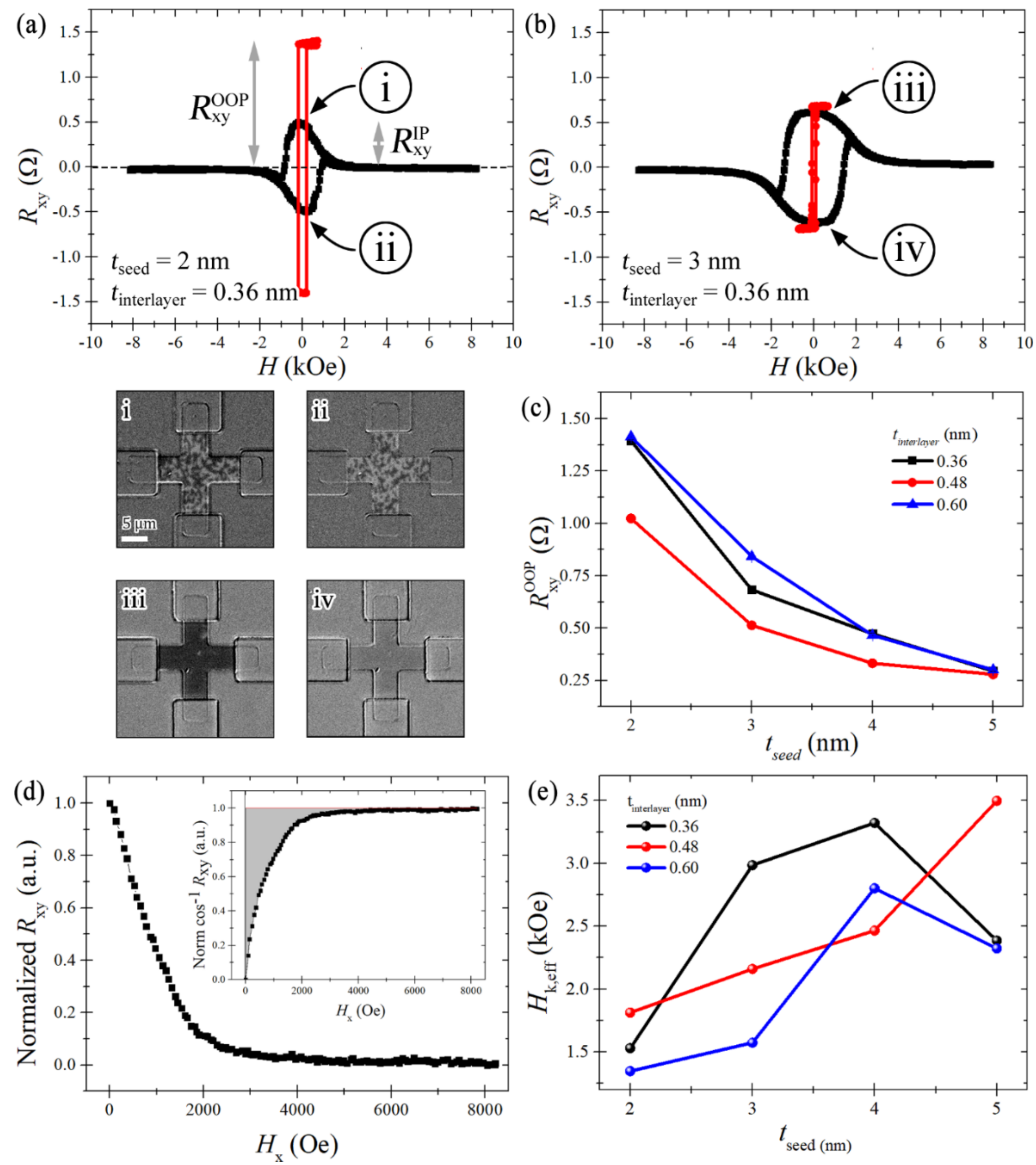

Figure 43: (a) and (b) Anomalous Hall resistance R_{xy} in a sweeping in-plane field H_x (black) and out-of-plane field H_z (red) across varying t_{seed} and $t_{interlayer}$. All devices show PMA with square hysteresis loops in H_z. Kerr images (i) – (iv) show the respective remanent z-magnetization state at $H_x = 0$ Oe. (c) R_{xy} across all devices from the OOP field sweep measurement. (d) The normalised R_{xy}^{IP} in the $+H_x \rightarrow 0$ Oe quadrant is converted to $\cos^{-1} R_{xy}^{IP}$ to determine the device anisotropy. (e) The effective anisotropy field is then determined from the effective anisotropy energy $K_{u,eff}$ shown in the integrated area shaded in grey. (e) Effective anisotropy field $H_{k,eff}$ across devices with varying t_{seed} and $t_{interlayer}$ thicknesses.

Devices with $t_{interlayer}$ = 0.48 nm show that $H_{k,eff}$ scales with t_{seed}, while that of $t_{interlayer}$ = 0.36 nm and 0.60 nm show peak $H_{k,eff}$ at t_{seed} = 4 nm. The $H_{k,eff}$ for each multilayer stack was determined using the normalised R_{xy}^{IP} from the $+H_x \rightarrow 0$ Oe quadrant as shown in the exemplary curve in **Figure 43** (d). The inset shows the conversion to normalised $\cos^{-1} R_{xy}^{IP}$ and the shaded region represents the effective anisotropy $K_{u,eff}$. $H_{k,eff}$ was then determined for all the devices and summarized in **Figure 43** (e). The $H_{k,eff}$ peaks at t_{seed} = 4 nm with the exception of devices with $t_{interlayer}$ = 0.48 nm which exhibited monotonic increase with t_{seed}. In general, a thicker Pt seed layer t_{seed} would yield [Co/Pt] multilayers with stronger PMA [187]. However, the effective anisotropy field $H_{k,eff}$ peaks at t_{seed} = 4 nm and noticeably decreases for t_{seed} = 5 nm as a result of increased surface and interface roughness with increasing t_{seed} [188]. The roughness is exacerbated for subsequently deposited layers of Co and Pt, and can lead to undesirable "orange-peel" coupling, leading to the decrease in $H_{k,eff}$ observed for devices with $t_{interlayer}$ =0.36 and 0.60 nm [189].

6.3 Current Shunting Due to Varying Seed and Interlayer Pt Thicknesses

When performing electrical measurements, the various thin film layers will conduct fractional current densities J due to their individual electrical resistivities and thicknesses. Assuming four resistors in parallel for each layer i = Ta (adhesion), Pt, FM, Ta (cap), we approximate the current shunting through each layer, having width w and length l, by noting that the conductance of the entire device G_{device} is the sum of all individual layer conductances G_i,

$$G_{device} = \sum G_i = \sum \frac{t_i w}{\rho_i l} \tag{56}$$

where t_i is the thickness, and ρ_i is the resistivity of layer i. Here, we treat the $[Co/Pt]_3/Co$ multilayer as one perpendicularly magnetized ferromagnetic (FM)

layer and assume that the voltage across each layer i is the same. The individual device resistances were measured and plotted in **Figure 44** (a). The inset illustrates the circuit for each device with each layer having its own conductance values G_i. From this information, we can account for the current density through the HMs. The current density through layer i can be determined from the ratio of conductance $r_i = G_i/\Sigma G_i$, so that the current density through each layer scales as $J_i = r_i J$.

Subsequently, in order to determine the resistivities of the HM layers, we deposited varying thicknesses of Ta and Pt on to thermally oxidised Si substrate. The sheet resistances for Ta and Pt were measured using the in-line four-point probe method and plotted in **Figure 44** (b). The resistivities ρ scale approximately as a reciprocal to film thickness t, with values close to those reported elsewhere [190-192]. The sputtered Ta films are noticeably resistive, indicating that they form the tetragonal β-Ta phase that has strong SOC [129,190]. In comparison, the blue dashed line indicates the resistivity of α-Ta of about $13\ \mu\Omega-\text{cm}$ [190,193]. We use the measured β-Ta resistivity for the adhesion and capping Ta layers [24,194]. As t_{seed} increases in thickness, more current is permitted to flow through the HM layer. The ratio r of current flowing through the HM layers that contribute to the SOT is determined and plotted in **Figure 44** (c). More current is shunted through the HM layers with a thicker t_{seed} or a thinner $t_{interlayer}$.

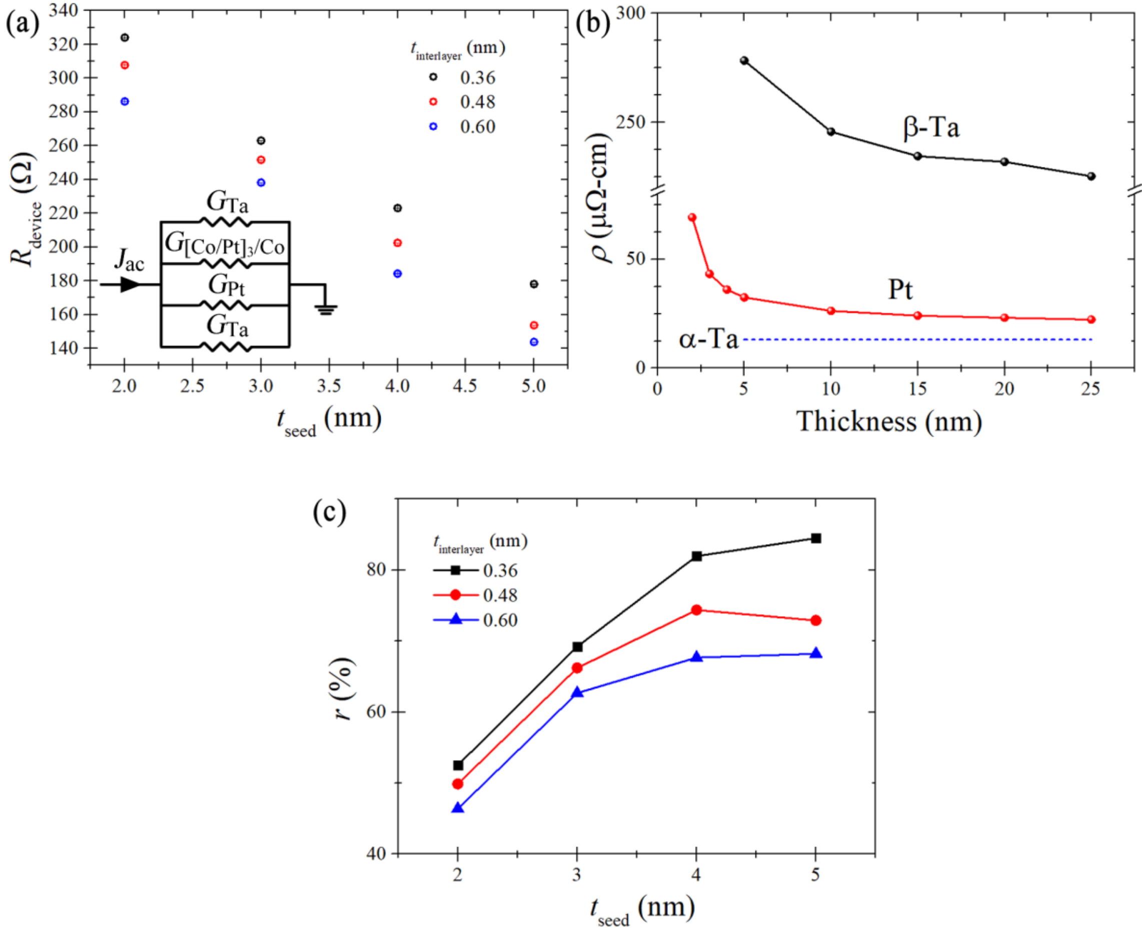

Figure 44: (a) Resistances of measured devices showing monotonic decrease in resistance as $\boldsymbol{t_{seed}}$ and $\boldsymbol{t_{interlayer}}$ increases. Inset shows a circuit schematic of four-resistor approximation with respective conductance G_i, where i represents the Ta adhesion layer, Pt seed layer, [Co/Pt]3/Co multilayer, and the Ta cap layer. (b) Resistivities ρ of Ta and Pt of varying thicknesses deposited on thermally oxidised Si substrate. α-Ta resistivity is shown for comparison [54]. (c) Ratio r of current through the Pt and Ta layers sandwiching the [Co/Pt]3/Co multilayer.

6.4 Quantification of SOT Efficiency

Next, we quantify the SOT damping-like (longitudinal) H_L and field-like (transverse) H_T effective fields for varying t_{seed} and $t_{interlayer}$ using the harmonic lock-in technique [126,195]. A Keithley 6221 was used to source an AC current density with amplitude ranging from 8×10^8 to 8×10^9 A/m^2 in intervals of 1×10^8 A/m^2. A Signal Recovery 7265 lock-in amplifier was used to detect the first and second harmonic Hall voltages simultaneously. A small bias field of 400 Oe in the z-direction was present to prevent the formation of domains.

The measurement set-up is illustrated in **Figure 45** (a). When an in-plane current is injected along the x-axis, a transverse spin current from the HM layers diffuses into the FM multilayer. Due to the opposite spin Hall angles of Pt and Ta and the structural inversion asymmetry, a net spin torque acts on the FM. Using a sinusoidal current to adiabatically oscillate the magnetization, we measure the first V_{ω} and second $V_{2\omega}$ harmonic Hall voltages across a range of current densities J_{ac} as a function of external longitudinal and transverse fields H_x and H_y, respectively.

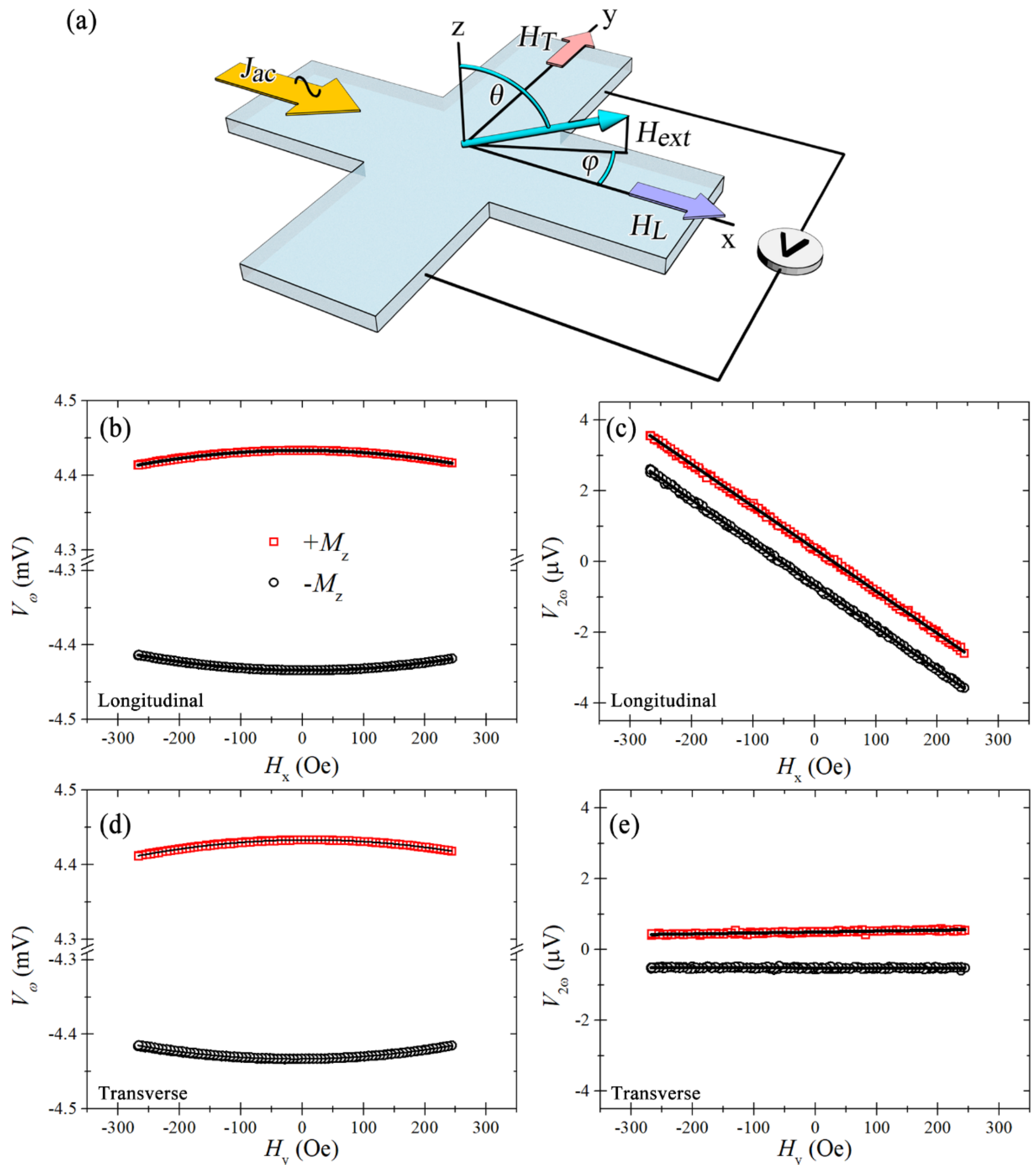

Figure 45: (a) Schematic set up for harmonic lock-in measurement of a Hall cross structure with coordinate system, where θ and φ are the polar and azimuthal angles, respectively. (b) and (d) First harmonics V_ω measurements in the longitudinal and transverse schemes, respectively, (c) and (e) Second harmonics $V_{2\omega}$ measurement in the longitudinal and transverse schemes, respectively, for the sample with $t_{seed} = 3$ nm and $t_{interlayer} = 0.36$ nm.

Exemplary curves of the longitudinal and transverse V_ω and $V_{2\omega}$ for the sample with $t_{seed} = 3$ nm and $t_{interlayer} = 0.36$ nm are shown in **Figure 45** (b) to (e). Both longitudinal and transverse V_ω measurements show similar parabolic

characteristics. However, the longitudinal and transverse $V_{2\omega}$ have different linear behaviour, as shown in **Figure 45** (d) and (f). The substantially larger longitudinal $V_{2\omega}$ is indicative of a dominant SHE, while the significantly smaller slope of the transverse $V_{2\omega}$ is indicative of negligible Rashba contribution [196]. The longitudinal $V_{2\omega}$ have negative slopes for up and down magnetized states $\pm M_z$. In contrast, the transverse $V_{2\omega}$ have different slopes and relatively smaller magnitude for up and down magnetized states $\pm M_z$. V_ω and $V_{2\omega}$ are fitted using quadratic and linear fitting functions, respectively. The following relation is then used to determine H_L and H_T:

$$H_{\mathrm{L(T)}} = -2\frac{\partial V_{2\omega}}{\partial H_{x(y)}} / \frac{\partial^2 V_\omega}{\partial H_{x(y)}^2} \tag{57}$$

In order to account for the in-plane magnetic field Hall resistance i.e. planar Hall effect (PHE), φ-dependent ($\theta \approx 90°$) measurements were performed using an in-plane field $H_{IP} = 4$ kOe. The Hall resistance can be expressed as:

$$R_{xy} = R_A \cos\theta + R_P \sin^2\theta \sin 2\varphi \tag{58}$$

where R_A and R_P are the anomalous and planar Hall resistances, respectively. The individual curves are then fitted to obtain R_P and the PHE/AHE ratio $\xi = R_P/R_A$, which is then used to determine the modified, PHE-corrected SOT efficiencies $H'_{L(T)}$ given by [127]:

$$H'_{L(T)} = \frac{H_{L(T)} \pm 2\xi H_{T(L)}}{1 - 4\xi^2} \tag{59}$$

Due to imperfect alignment between the sample plane and the field, a small OOP field component is present as the sample rotates about the z-axis. This is resolved by averaging the planar Hall resistance at θ and $\theta + \pi$ as shown in the φ-dependent R_{xy} curves plotted and fitted using equation (51) in the **Figure 46** (a) for devices with $t_{seed} = 2$ nm.

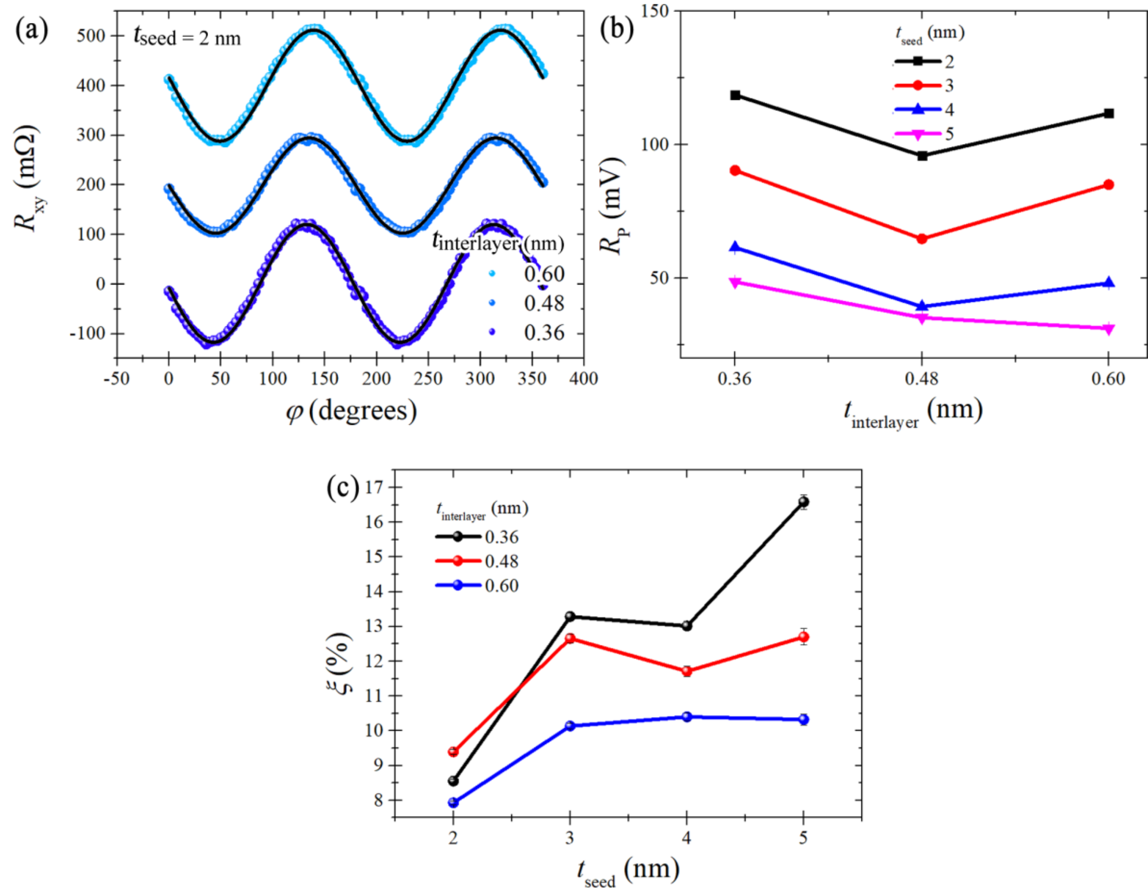

Figure 46: (a) φ-dependent (θ ≈ 90°) R_{xy} curves fitted with equation (57) for t_{seed} = 2 nm. (b) R_P and (d) $\xi = R_P/R_A$ across all devices with t_{seed} and $t_{interlayer}$.

The PHE- and current-corrected $H'_{L(T)}/J_{ac}$ are shown in **Figure 47**. We find that after accounting for both corrections, $H'_{L(T)}/J_{ac}$ are several times larger as compared to their uncorrected values. The magnitude of H'_L/J_{ac} is greater than that of H'_T/J_{ac}, indicating that the SOT is predominantly due to the SHE mechanism [197,198]. At its thinnest range of t_{seed} = 2 nm, the film stacks demonstrate R^{IP}_{xy}/R^{OOP}_{xy} below unity at H_x = 0 Oe. In particular, the measured SOT efficiency for the device with t_{seed} = 2 nm and $t_{interlayer}$ = 0.36 nm shows an anomalous SOT efficiency. This is attributed to ineffective (111) texturing of Co by the thin Pt seed layers, as thicker t_{seed} and $t_{interlayer}$ generally

improved the in-plane and out-of-plane remanence ratio $R_{xy}^{IP}/R_{xy}^{OOP} \approx 1$ so that the magnetization completely returns to one of the bistable (up or down) states at $H_x = 0$ Oe [199]. From our measurements, we observe that the damping- and field-like efficiencies are inversely related to t_{seed} and $t_{interlayer}$. The high-resistivity β-Ta layer generates substantial SOT [200,201]. Due to the opposite spin Hall angle with respect to the adjacent Pt seed layer [163], spin current from the β-Ta layer gets screened. Consequently, the net spin current from the opposite contributions of the β-Ta/PT HM bilayer decreases with increasing Pt seed layer thickness t_{seed}. Similarly, thicker $t_{interlayer}$ leads to greater spin scattering across the multilayers [104,202,203]. From the damping-like field efficiency $|H_L/J_{ac}|$ plot, the seed and interlayer Pt layers can be observed to screen the spin current from the bottom Ta layer as t_{seed} and $t_{interlayer}$ increase in thickness. However, there is no appreciable correlation between the already small transverse field efficiency $|H_T/J_{ac}|$.

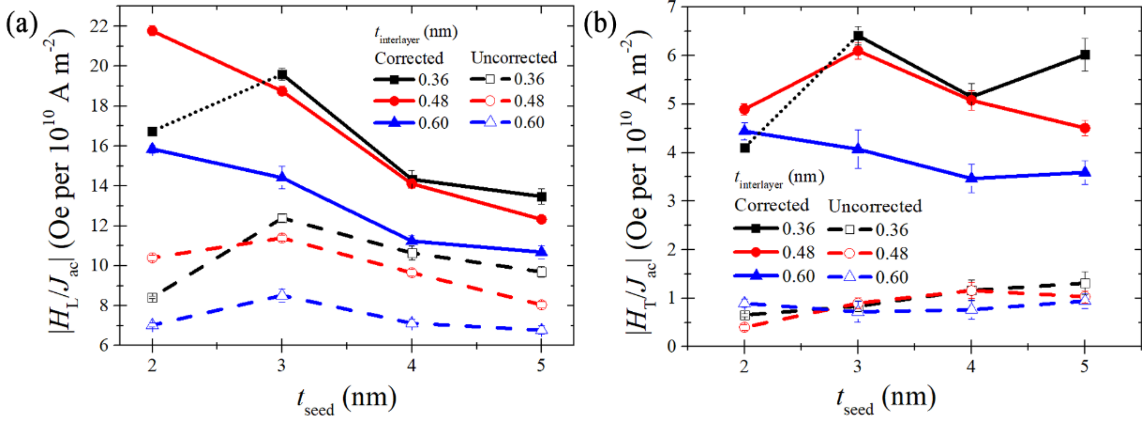

Figure 47: Uncorrected SOT efficiencies (dashed lines) accompanied by current-density and PHE-corrected SOT efficiencies for (a) longitudinal and (b) transverse efficiencies. The corrections result in efficiencies several times larger than uncorrected values.

6.5 Conclusion

In this work, we have studied perpendicularly magnetized multilayers of Ta/Pt/[Co/Pt]$_3$/Co/Ta with varying Pt seed and interlayer thicknesses. The Pt

interlayer thickness influences the interlayer exchange coupling between the Co layers. Consequently, this affects the Pt seed thickness dependence on the anisotropy. It was determined from R_{xy}-H_x measurements that $t_{seed} \geq 3$ nm was necessary to achieve remanence close to unity. *In-situ* Kerr microscopy images confirm this observation. The SOT efficiencies for all devices were then measured with current density and PHE-correction taken into account. The damping-like efficiency scales inversely with Pt seed and interlayer thicknesses, indicating that the spin current from the bottom Ta layer gets screened from both. As such, there is a compromise between PMA and SOT efficiency, as the SOT efficiencies decrease with increasing t_{seed} and $t_{interlayer}$ thicknesses.

Chapter 7

Programmable Spin-Orbit Torque Logic Device with Integrated Bipolar Bias Field for Chirality Control

In this chapter, we demonstrate logical operations using an SOT-driven double Hall cross device. An integrated bias field line is implemented and allows for the generation of a local bias field necessary for chirality control in magnetization switching. A SPICE circuit model founded on formalisms developed by Bonhomme and Hong is also presented [204,205]. The SPICE model is then used to demonstrate a half-adder circuit using the experimentally demonstrated reconfigurable SOT-driven logic device. The development of the SPICE models and circuits are described in the Appendix. Parts of this chapter have been published in **Advanced Electronic Materials** [178].

7.1 Motivation

Modern day computers rely on densely packed transistors that form the basis of components such as the processor, random access memory (RAM), and certain classes of solid-state memories. This separation of processing and memory units form a part of the von Neumann architecture. While simple in design, the von Neumann architecture faces limitations to the performance of the system due to the shared bus, preventing concurrent instruction fetch and data operation processes. This limitation is referred to as the von Neumann bottleneck. Foundries continue to find new ways of shrinking transistors so that they can be more densely packed into integrated circuits. A trend in which transistor count was observed to approximately double every 18 months was recognised and posited by Gordon Moore. This trend is dubbed Moore's law [206]. However,

source-to-drain leakage and limited material options pose physical limitations to transistor scaling, and Moore's law is not expected to continue along its trajectory indefinitely. Driven by the need to address both the von Neumann bottleneck and scaling limits predicted by Moore's law, spintronic devices have been shown to be strong contenders for logic-in-memory applications, in which processing and memory are no longer separate entities.

Spintronic devices exploit the spin degree of freedom of electrons. This has enabled the development of non-volatile, high-speed, ultra-low energy dissipation, and scalable spin-based sensors and memory devices. These devices utilize the spin property of the electron rather than relying on electronic charge alone as a state variable, and address device level issues such as high dynamic and standby power dissipation due to leakage current, and heat dissipation inherent to conventional silicon-based complementary metal-oxide-semiconductor (CMOS) technology [206]. Several spintronic logic devices have been proposed, such as all-spin logic in which non-local spin currents are used to switch nanomagnets [207,208], and STT-driven MTJ-based logic devices [209,210]. SOT-driven spintronic devices are a particularly attractive alternative to STT-driven devices, due to their separate read-write scheme and high efficiency. However, their operation typically requires additional initialization or reset pulses, the exchange-coupled canted spins reduce both anomalous Hall sign-to-noise ratio as well as thermal stability of the ferromagnetic layer, and device-to-device variation in exchange coupling strength is expected [211,212].

In this work, a SOT-driven logic device using a double Hall cross structure is experimentally demonstrated. The reconfigurability feature takes advantage of the switching symmetry breaking in-plane field by means of an integrated bias field line, allowing for the generation of a local bias field. The on-chip bipolar bias field can be toggled to flip the SOT-induced switching chirality, and to assist with deterministic SOT magnetization switching. This allows for on-

the-fly reconfigurability of the logic device to function as one of the several possible logic gates: AND, NOR, XNOR, XOR, NIMP, and converse NIMP. Subsequently, the logic device is modelled in SPICE. Through compact-modelling and circuit simulation, the logic functionality is expanded to applications such as half-adders.

7.2 Experimental Details

Thin films with as-deposited PMA were first prepared by sputtering a multilayer stack comprising Ta (5)/Pt (3) /[Co (0.6)/Pt (0.6)]$_3$/Co (0.6)/Ta (5) on to thermally oxidised Si substrates by DC magnetron sputtering. Numbers in parenthesis indicate nominal film thicknesses in nanometers. The subscript represents the number of [Co/Pt] bilayer repeats. Electron beam lithography and Ar ion beam etching were used to pattern the logic device structure, which comprised of two Hall crosses sharing a common Hall bar. Subsequently, electrical contacts of Ti (5)/Cu (100)/ Ta (5) were deposited at the wire ends. The wires along which current is injected across are referred to as channels 1 and 2, and respectively identified in red and blue dashed boxes in **Figure 48** (a). The common Hall bar is identified with a green dashed box. A bias-tee allows for write and read currents to be delivered to each channel. The write current density used is $J_n = 1.5 \times 10^7$ A cm^{-2} and the read current $I_{dc,n} = 100$ µA through each channel n. The cumulative anomalous Hall voltage formed $V_H = V_{H,1} + V_{H,2}$ is read out across the common Hall bar as illustrated in **Figure 48** (b) and the inset diagram. As $V_H \propto I_{dc} m_z$, the anomalous Hall voltage measures the OOP magnetization component of the device.

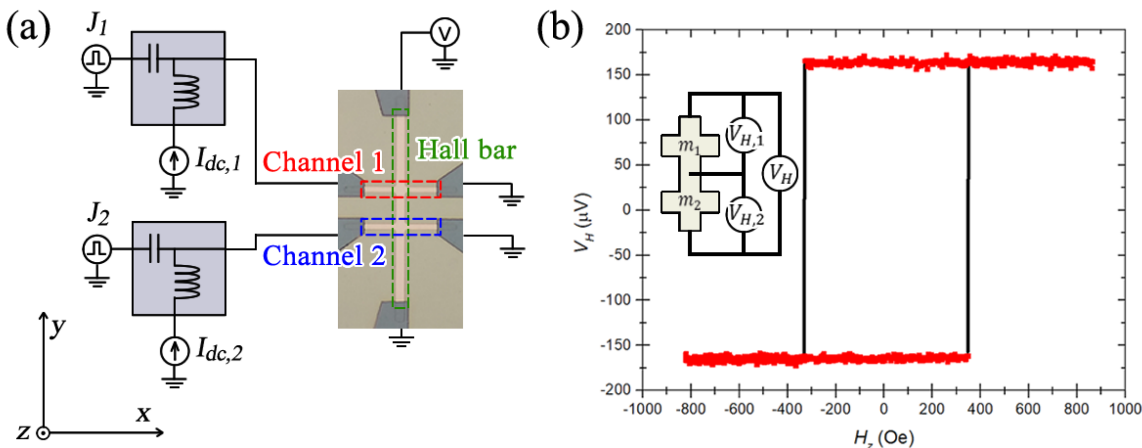

Figure 48: (a) Schematic of SOT-driven logic device. (b) Cumulative anomalous Hall voltage V_H across a sweeping OOP magnetic field H_x.

The patterned logic device was measured electrically in a sweeping OOP field H_z. The sharp switching shows that the device exhibits PMA, and the magnetization across both junctions of the device have the same coercivity $|H_c| \approx 350$ Oe. As the junctions are of the same multilayer stack with similar geometry, it can be assumed that $|V_{H,1}| \approx |V_{H,2}|$.

In the practical device, the magnetization across channels 1 and 2 should have the ability to be switched independently by electrical means. In current-induced STT devices, a fixed layer is required to polarize injected current pulses [213]. The spin polarized current then switches the FL representing the data via momentum transfer between itinerant spin and local magnetization. On the contrary, SOT-driven devices do not require such a fixed layer [154]. In a HM/FM structure, current flowing through the HM layer with large SOC leads to spin accumulation at the HM/FM interface. The accumulated spins at the interface diffuse into the FM layer and applies a torque on the magnetization, which leads to magnetization switching. For PMA devices, the magnetization needs to be canted along the $\pm x$ direction in order to produce deterministic switching. This can be achieved by applying an external field H_x, or via exchange coupling with an adjacent magnetic layer with IMA. The exchange coupling method introduces additional thin film growth challenges and is typically fixed

along an orientation induced by field annealing. Also, the magnetization canting is always present, which leads to a reduced SNR of the anomalous Hall voltage V_H. As such, an on-device solution for generating a local magnetic field that can toggle the magnetization canting on and off would overcome the challenges. The local field polarity can also be changed to allow for device reconfigurability and to achieve polymorphic logic device functionality. The integration of a bias field line in close proximity to the device will meet these requirements.

7.3 Logic Operation With a Double Hall Cross Device

The logic device is first operated using an externally applied magnetic field by mounting the device between the poles of a LakeShore EM4 electromagnet. The SOT-driven magnetization switching was performed by injecting 100 ns current pulses of $J_1, J_2 = \pm 1.5 \times 10^7$ A cm^{-2} in the presence of $|H_x| = 300$ Oe. After each write process, the magnetization state was probed using $|I_{dc,1}|, |I_{dc,2}| = 100$ μA concurrently through both channels and measuring V_H. Letting positive (negative) J represent logical inputs "T" ("F") representing "true" ("false"), **Figure 49** shows permutations of $(J_1, J_2) = (\mathrm{TT}, \mathrm{TF}, \mathrm{FT}, \mathrm{FF})$, for $\pm H_x$ probed using a fixed probing polarity $I_{dc,1}, I_{dc,2} = 100$ μA. The logic device produces a ternary output where $V_H \approx (+200, 0, -200)$ μV. The dashed line in the V_H output plot indicates a threshold for interpreting the output signal, resulting in a Boolean output. The device output now resembles that of AND and NOR logic gates, simply by changing the direction of H_x.

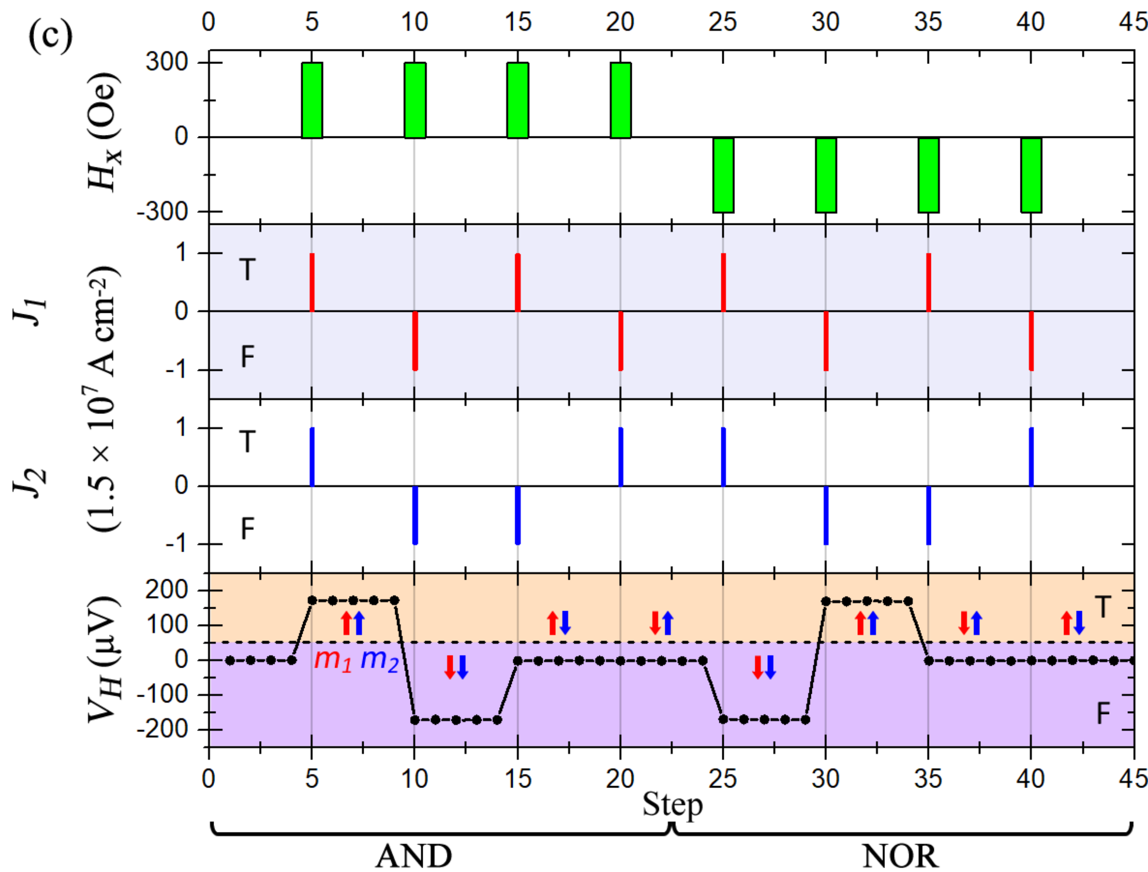

Figure 49: External field H_x, inputs J_1 and J_2, and corresponding anomalous Hall voltage output V_H of a double Hall cross logic device.

Aside from J_n and H_x, the probing currents $I_{dc,n}$ can also present themselves as another form of input. This leads to two possible operating modes of the device. In mode I described above, the device logic gate functionality is determined by the probing inputs $I_{dc,n}$, and represents the fixed quantity. The magnetization states m_1 and m_2 can be varied by means of J_1 and J_2, respectively. Depending on the nature of the application, writing device states repeatedly can be energy expensive. In mode II, the device magnetization states m_1 and m_2 become the fixed quantity. The read currents $I_{dc,n}$ then become the logical inputs, where $+I_{dc}$ ($-I_{dc}$) represent "T" ("F") logical inputs. Modes I and II are summarised in Table 3.

	Mode I	Mode II
Logic Gate (fixed parameter)	Fixed read scheme $I_{dc,1}, I_{dc,2}$	Fixed magnetization states m_1, m_2
Logical Inputs (varying parameter)	Varying magnetization states m_1, m_2	Varying read scheme $I_{dc,1}, I_{dc,2}$

Table 3: Differentiation of operating modes.

Using *in-situ* Kerr microscopy, the four possible magnetization configurations – a) Up–Up, b) Up–Down, c) Down–Up, and d) Down–Down – are shown in **Figure 50**. The dark (light) contrasts correspond to up (down) magnetization states across each channel.

Up–Up				
$I_{dc,1}$	$I_{dc,2}$	V_H	Half Rectification	Full Rectification
T	T	+200 µV	T	T
T	F	0	F	F
F	T	0	F	F
F	F	−200 µV	F	T
			AND	XNOR

Up–Down				
$I_{dc,1}$	$I_{dc,2}$	V_H	Half Rectification	Full Rectification
T	T	0	F	F
T	F	+200 µV	T	T
F	T	−200 µV	F	T
F	F	0	F	F
			NIMP	XOR

Down–Up				
$I_{dc,1}$	$I_{dc,2}$	V_H	Half Rectification	Full Rectification
T	T	0	F	T
T	F	−200 µV	F	F
F	T	+200 µV	T	F
F	F	0	F	T
			Converse NIMP	XOR

Down – Down				
$I_{dc,1}$	$I_{dc,2}$	V_H	Half Rectification	Full Rectification
T	T	−200 µV	T	T
T	F	0	F	F
F	T	0	F	F
F	F	+200 µV	F	T
			NOR	XNOR

Figure 50: Kerr microscopy images of the magnetization states in a double Hall cross logic device with channels spaced approximately 8 µm apart. Each Kerr microscopy image is accompanied by the corresponding interpretation of truth table using different read schemes and half- or full-rectification.

The devices used in the Kerr microscopy images had channels placed 8 µm apart for imaging purposes, while actual devices used in measurements had channels spaced approximately 20 µm apart to minimize current shunting. For each configuration, the probing inputs permutate between TT, TF, FT, and FF, where T and F correspond to $+I_{dc,n}$ and $-I_{dc,n}$, respectively. Further processing to half-rectify ($V_H > 0$) or full-rectify ($|V_H|$) the outputs can be implemented to

expand the range of logic to include NOR, XNOR, AND, XOR, NIMP, and converse NIMP. The outputs for mode II are also summarised in the table for all four permutations of the logic device magnetization states.

7.4 Integrated Bias Field Line for Self-Contained Chirality Control

A method to localize the switching symmetry-breaking H_x for selective logic devices would be favourable for device integration, where arrays of such logic devices are fabricated on the same substrate. One approach is to place a bias field line in close proximity to but electrically isolated from the device. Passing a current through the bias field line would generate a local Oersted field to cant the device magnetization. A 200 nm dielectric passivation layer of HfO was sputtered over a rectangular region, isolating the device from subsequent patterning and deposition of Ti (5)/Cu (100)/ Ta (5). The geometry of the bias field line was prepared such that the Oersted field would be coaxial to J, and the field itself could not switch the magnetization. By changing the magnitude and polarity of the current through the bias field line I_{FL}, the amplitude and direction of the Oersted field could be tuned. This method provides an on-chip solution to local field generation for SOT switching, without perturbing neighbouring devices. **Figure 51** (a) shows the optical microscopy image of the logic device with the integrated bias field line. A passivation layer of HfO_2 electrical separates the bias field line from the device. A cross-sectional illustration along the dissection A–A in **Figure 51** (b) shows the two possible bias field line current directions $\pm I_{FL}$ and the corresponding Oersted field in red and blue arrows. The Oersted field then cants the device magnetization towards the $\pm m_x$ direction.

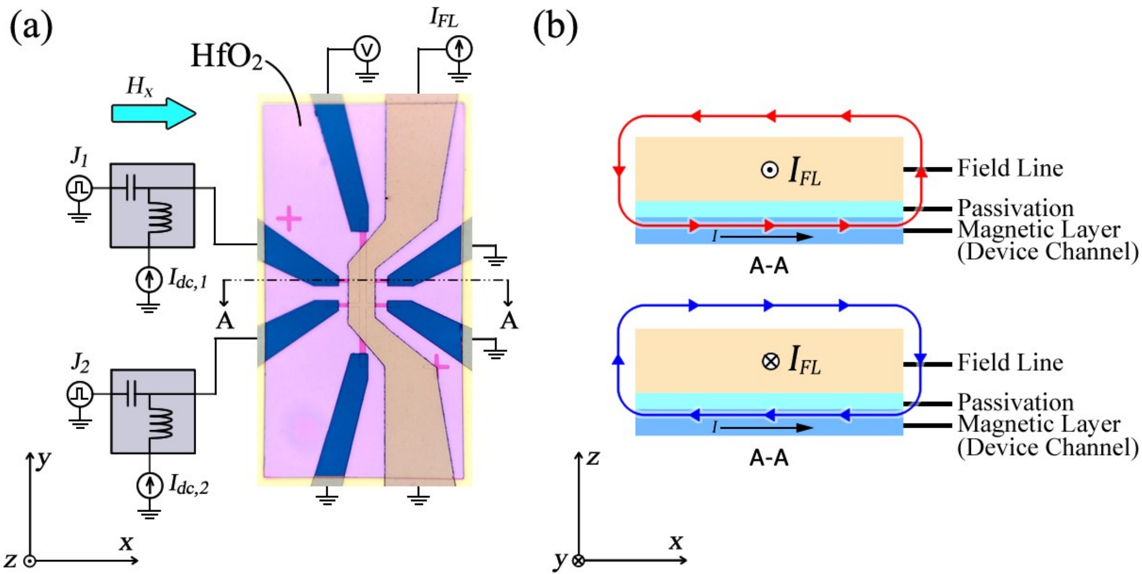

Figure 51: (a) Schematic of SOT-driven logic device with integrated bias field line. (b) Cross section of bias field line over device channel showing locally generated field line due to a field line current I_{FL}.

The reconfigurable logic functionality of the device is now demonstrated using the integrated bias field line for local Oersted field generation and magnetization canting. First, $I_{FL} = 30$ mA is applied through the bias field line. A 100 ns current pulse $J = \pm 1.5 \times 10^7$ A cm^{-2} is delivered through each channel in the four possible permutations. Then, I_{FL} is set to 0 mA to remove the local Oersted field. Probing currents of $I_{dc} = 100$ µA are delivered down each channel while the common Hall bar is probed to measure V_H. The additional energy expense for the generation of the bias field required for the magnetization switching operation can be estimated at under 1 nJ for a 100 ns pulse along a 10 Ω bias field line. The corresponding output V_H for corresponding inputs of I_{FL}, J_1 and J_2 are shown in **Figure 52**. The operating behaviour is similar to that achieved with an externally applied field. In addition, the reconfigurable logic device with integrated bias field in this work does not require initialization or reset pulses for operation.

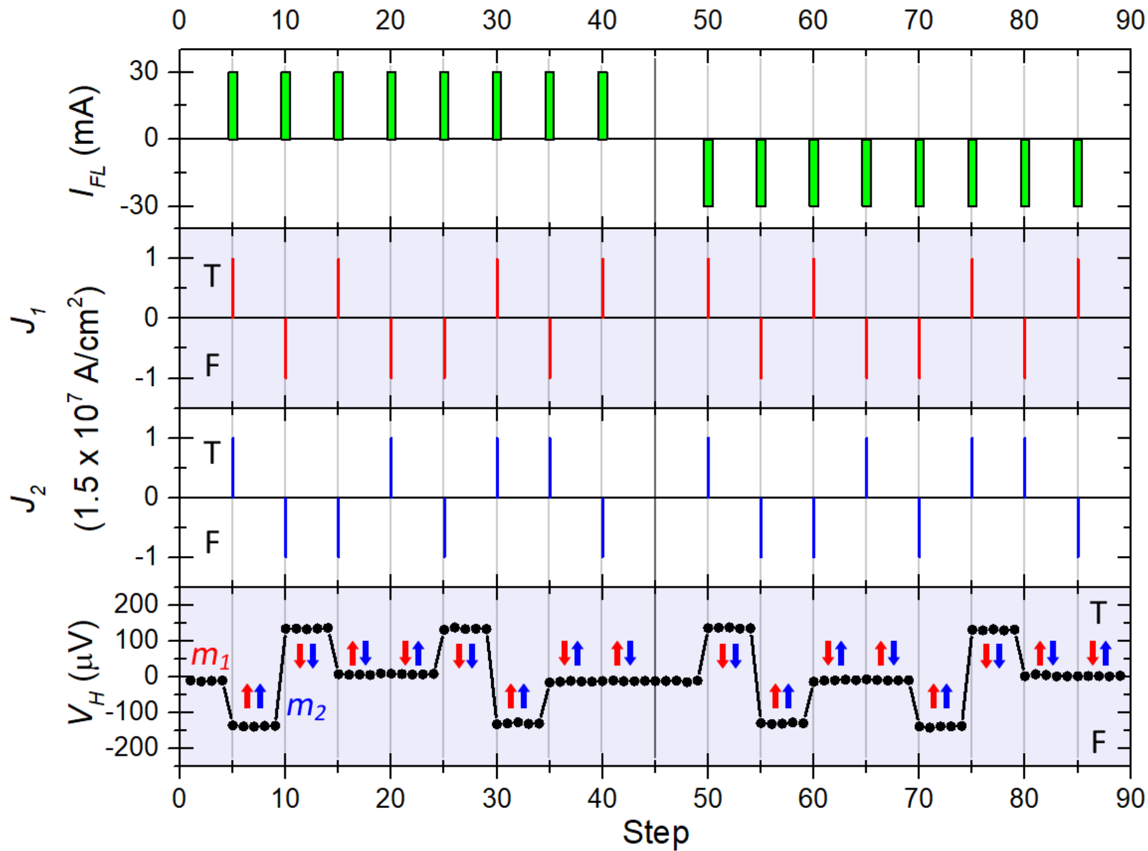

Figure 52: Field line current I_{FL}, inputs J_1 and J_2, and corresponding anomalous Hall voltage output V_H of a double Hall cross logic device with integrated bias field line.

7.5 Simulation of SOT-Driven Reconfigurable Logic Device and Half-Adder

The circuit models for SOT-driven devices are described in the Appendix. They are subsequently used to model the behaviour of the device magnetization when subjected to an external field and charge current. Parameters used in the simulation are taken from the fabricated multilayer stack illustrated in **Figure 53**. The total thickness of the multilayer is 17.2 nm. The $[Co/Pt]_3/Co$ multilayer is approximated as one FM layer. The channel and common Hall bar are 5 μm and 3 μm wide, respectively. The charge current injected along the device in the x-direction flows through the multilayer stack. Assuming the same potential difference across each layer, the multilayer stack can be modelled as four resistors

for each layer in parallel, and the current through each layer would scale inversely with the respective layer resistivity.

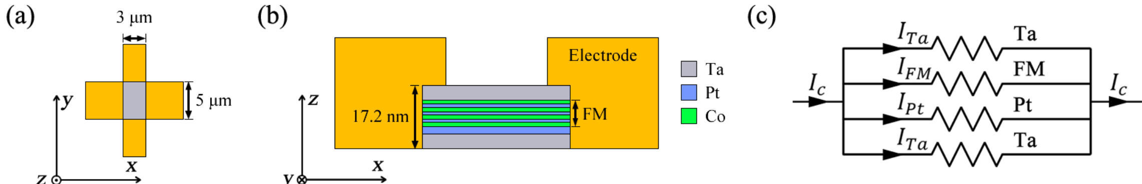

Figure 53: (a) Simulation device dimensions. (b) Cross-section of simulated device. (c) Model of simulated device showing parallel current flow across layers with different resistances and resistivities.

A current passing through both HM layers will result in spin currents diffusing through the bottom and top HM/FM interfaces. Due to the opposite spin Hall angles of Ta and Pt sandwiching the FM layer, these spin currents would complement each other. Furthermore, spin current from the bottommost Ta layer would diffuse into Pt and reduce the total effective SOT acting on the magnetization of the FM layer. These mechanisms are addressed with the SHE module for each HM layer.

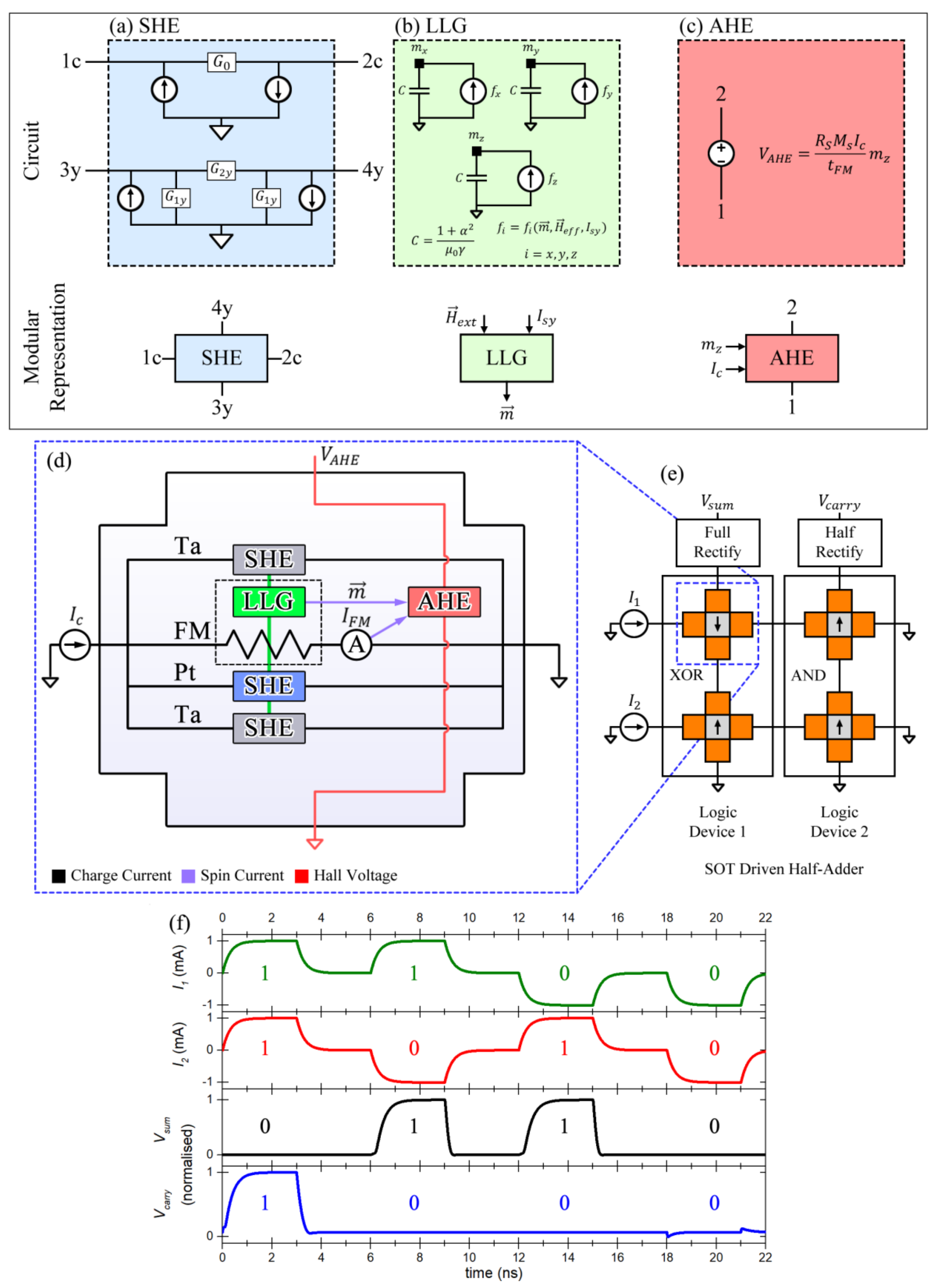

Figure 54: (a) The SHE circuit is represented by charge and spin circuits with respective conductance [24]. The charge circuit between terminals 1c and 2c contains a series conductance G_0 and two current sources I_{0c} which represent spin-to-charge conversion via the SHE. The spin circuit between terminals 3y and 4y consists of a series conductance G_{2y}, shunt conductances G_{1y} which represent

spin current attenuation via spin-flip processes, and current sources I_{0y} which represent charge-to-spin conversion by the SHE. (b) Capacitor-current source circuits which represent the LLG equation. Magnetization components m_x, m_y and m_z are represented as node voltages. (c) Voltage source circuit representation of the AHE where $V_{AHE} \propto I_c M_z$. Modular representations of the SHE, LLG, and AHE are shown under their respective circuit representations [23]. (d) Compact model of our multilayer Hall cross device. The HM layers are modelled using SHE modules while the FM layer is modelled using an LLG module and resistance R_{FM}. The AHE module accepts m_z from the LLG module and the current flowing through the FM layer I_c as inputs and outputs a transverse voltage VAHE. The correlation between the compact model to the symbolic representation is shown in blue dashed lines. Black arrows represent the magnetization state of the Hall cross, where an ↑ indicates $m_z > 0$ and ↓ indicates $m_z < 0$. (e) Design of half-adder circuit using two logic devices. Devices 1 and 2 have magnetization configurations and rectification circuits that yield the logical outputs of an XOR and AND gate respectively. Current sources are wired to the devices such that input current pulses can be delivered to both devices simultaneously. (f) Demonstration of half-adder functionality.

The SHE, LLG, and AHE modules, as well as the schematic for the compact model of a single Hall cross device are shown in **Figure 54** (a) to (d). The injected current I_c is split into four parallel resistances. The thick HM layers are represented by the charge-to-spin SHE converters, while the FM layer comprising $[Co/Pt]_3/Co$ multilayer is represented by the LLG module and accompanied by a resistor. Spin current from the HM layers diffuses into the FM layer and acts on the magnetization via the LLG module. Both the magnetization $\vec{m}$ and the current through the FM layer I_{FM} are fed into the AHE module to output the anomalous Hall voltage V_{AHE}. The material parameters for the HM layers used in the SPICE simulation are shown in Table 4.

HM	θ_{SH}	l_{SD} (nm)	ρ ($\Omega \cdot$ m)	σ ($\Omega^{-1} \cdot$ m^{-1})	t (nm)
Pt	0.1 ± 0.01	7.3	4.8×10^{-7}	2.08×10^{6}	5
Ta	-0.071 ± 0.006	1.9	2.9×10^{-6}	3.5×10^{5}	5

Table 4: Material parameters used in SPICE for the HM Pt and Ta.

The parameters for the FL layer are required in the LLG module. These are the saturation magnetization M_s, anisotropy field H_k, volume of the FM layer V, Gilbert damping constant α, and gyromagnetic ratio γ, and are shown in Table 5.

M_s ($A \cdot m^{-1}$)	$\mu_0 H_k$ (T)	V (m^3)	α	γ ($rad \cdot s^{-1} \cdot T^{-1}$)
6.75×10^{5}	1	6.3×10^{-22}	0.02	1.76×10^{11}

Table 5: Magnetic parameters used in SPICE for the ferromagnetic multilayer.

7.6 Conclusion

We have demonstrated a reconfigurable spin-orbit torque driven logic device. The logic device performs similarly with an external magnetic field generated by an electromagnet, as it would with a local Oersted field by an integrated bias field line for each logic device, demonstrating the viability of locally controlling the parameters for magnetization switching for each device. The device has also been shown to logically output AND, NOR, XNOR, XOR, NIMP, and converse NIMP, using either of two modes. The first mode is write-

and energy-intensive, and is useful for applications requiring the encoding of data for long term memory storage. The second mode is more energy-conservative, where the device states that determine the logic gate function are written once. Mode II is demonstrated in a SPICE-compatible compact modelling of the logic in a half-adder application. Spintronic-based computation by SOT switching as demonstrated in this work has the potential to lead to low power and high-speed spintronic circuit logic and computation.

Chapter 8
Conclusion and Future Works

8.1 Conclusion

We have experimentally demonstrated current-induced SOT magnetization switching in Co/Pt multilayers with as-deposited PMA and exhibiting multistate (analogue-like) properties. We show using *in-situ* differential Kerr imaging that the multistate behaviour is a result of the Hall cross geometry of the device, which leads to an inhomogeneous current-density profile across the device junction due to an injected current. The device was modelled using finite element software to obtain the current density profile across the device structure. Subsequently, micromagnetic simulation was performed using Mumax3, with the finite element derived current density profile mapped to an effective OOP field. The micromagnetic simulation results agree with the *in-situ* Kerr images of the evolving domain configuration with increasing current amplitude and corresponding effective OOP field. As the input write current and corresponding current density increased, the effective SOT field across the junction enabled gradual and progressive magnetization switching across the device junction. Using the AHE, the Hall voltage across the transverse Hall bar was demonstrated to scale with write current amplitude. As the device was subjected to elevated operating temperatures typically observed in integrated circuits, we show that the write and read operations of the device evolved accordingly with device temperature. The thermal sensitivity of the device operation showed that proper circuit sensing was necessary to reliably write and read the device. Alternatively, the temperature sensitivity showed that the multistate device has the potential to function as a thermal sensor. We also

showed that both the SOT efficiency and effective DMI field of the Co/Pt multilayer deteriorated with elevated temperature.

As the SOT efficiency of the multilayer is a critical measure in which to improve the energy efficiency of the device, the Pt seed (buffer) and interlayer thicknesses were varied. Using the adiabatic harmonic measurement technique, the first and second harmonics were measured to obtain the effective damping-like and field-like torques. The results from our multilayer stack showed that a substantial source of spin current originates from the high-resistivity β-Ta base layer. A more accurate determination of the damping-like and field-like torques was obtained by accounting for the current density through the FM multilayer and by applying the correction to the PHE contribution. The damping-like contribution to the SOT was also found to be dominant, implying that the source of spin polarized currents was due to the SHE. As the Pt seed thickness increased, the PMA of the multilayer improved, but the spin current from the β-Ta layer became increasingly screened as evident from the decrease in effective damping-like torque.

Application of the SOT-driven device was also demonstrated in the form of a double Hall cross structure. The device was patterned to resemble two Hall crosses sharing a common Hall bar. The magnetization across the two device channels could be independently written, and the cumulative Hall voltage probed to produce a trinary output. Using appropriate rectification and thresholding, the device was demonstrated to function as logic gates, subjected to the bias field, write current, and probe current directions. Subsequently, a bias field line was integrated in order to achieve a self-contained source of Oersted field, necessary for magnetization canting and deterministic SOT-induced magnetization switching. The device was demonstrated to operate as a reconfigurable logic-in-memory device. Using SPICE, the logic device was used to simulate half-adder functionality.

8.2 Future Works

Spintronic devices are promising candidates for emerging next-generation non-volatile, low-power, high-speed, and high endurance memory devices. However, there still exists an abundance of new physics to be discovered that would revolutionarily open new opportunities and overcome existing challenges. To drive spintronic logic and neuromorphic devices forward, we will need to tackle several aspects pertaining to efficiency and performance: i) The need for materials with large SOC beyond elemental HM, ii) materials for VCMA-assisted magnetization switching that would benefit parallel device operation, and iii) stochastic MTJ with multistate characteristics without compromising device density.

8.2.1 Characterization of New Materials with Large SOC for High-Efficiency Current-Induced SOT Magnetization Switching

HM and RE elements such as Ta, Pt, W, Gd, and Tb have been the most commonly used materials to enhance SOT efficiency and spin accumulation for SOT-driven magnetization switching. Furthermore, RE materials have been shown to be a potential source of SOT due to their large SOC [180,214,215], due to their partially-filled *f* orbitals [215,216]. Large spin Hall efficiency in RE metals were reported for Gd, Dy, Ho, Lu, and Tb [180,214,215,217]. However, there exists untapped potential in the exploration of doped and alloyed materials to achieve large SOC, accompanied by the modification of other properties such as magnetic damping, magnetic grain control, and interfacial spin transparency [218-224].

8.2.2 VCMA-Assisted Magnetization Switching

Parallel computing allows for concurrent execution of processes. Modern computers come with multiple cores within the CPU or GPU to perform certain tasks in a parallel manner within a single machine. Others use clusters comprising multiple computers to undertake heavier computational loads.

Similarly for spintronic device arrays, individual devices can be multiplexed such as in a random-access memory. However, computation using crossbar arrays such as illustrated in **Figure 7** can also be implemented in parallel. However, for current-induced spin-torque driven devices, the charge current requirements scale with device array size [225]. Using VCMA-assisted magnetization switching will allow for selective device switching with lower power utilisation [226-229]. The choice of high-κ dielectric materials and their thicknesses determine the electric field strength and induced change in interface anisotropy.

8.2.3 Stochastic MTJ as a Multistate Device

The multistate behaviour achieved using DW-MTJ and Hall cross devices are dependent on the number of magnetic domains that can be switched. The gradual changes in Hall voltage in a Hall cross device was shown to be a result of the inhomogeneous current density across the device junction. This implies that the number of device states is dependent on the areal size of the device junction, and this clearly poses a challenge with regards to scalability and device density. Instead of utilizing the magnetization domains, it has been demonstrated that a properly scaled MTJ with quasi-stable binary states exhibits stochasticity due to thermal fluctuations. Furthermore, by using electrical control of the device anisotropy such as by VCMA, or by applying an STT bias, the probability of the device state being up, down, or varying probability can be biased or tuned [87,88,230]. Therefore, instead of using space as a requisite for multi-domain switching, one can use a single spin in the time domain to perform averaging of the fluctuating spin state. Furthermore, the dynamics of a spin is intrinsically in the GHz range, and high speed time-averaged probing of the spin state is possible. However, such a device does not serve as non-volatile memory, as it is the probabilistic property of the device that is exploited. **Figure 55** (a) illustrates the stochastic behaviour of a probabilistic bit due to thermal noise. At zero bias $V =$

0 V, the magnetization has equal probability of being in the up or down state, and the average magnetization is close to 0. A bias voltage V can be used to tune the tendency for the magnetization to preferentially be in the down state ($V < 0$) or up state ($V > 0$). The time-averaged magnetization across bias voltages from -5 V to $+5$ V is shown in **Figure 55** (b). The points closely approximate a sigmoid function.

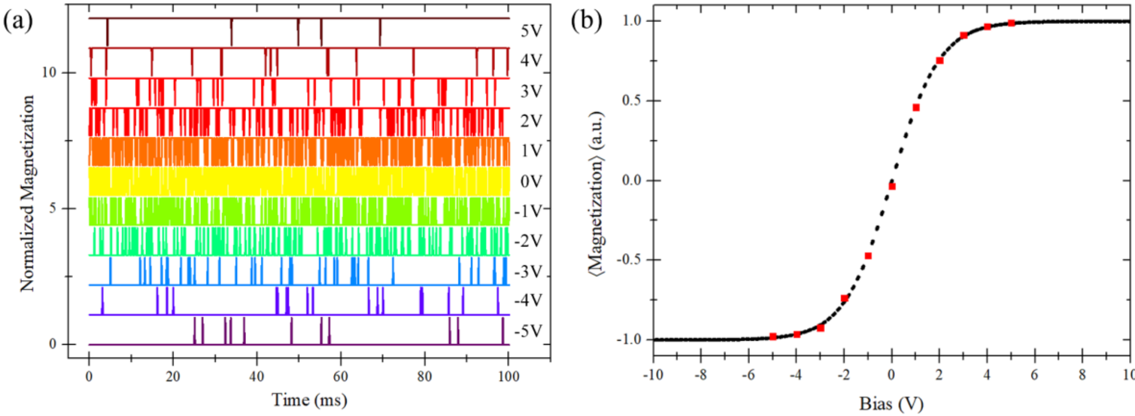

Figure 55: (a) Stochastic readout of a probabilistic bit across varying bias voltages over 100 ms sample time. (b) Average magnetization over 100 ms across a range of bias voltage.

Unlike domain-dependent devices, stochastic MTJs can be used to generate a multistate response by time averaging the thermally-induced stochastic behaviour of the magnetization. Stochastic MTJs can be applied to existing applications that use conventional deterministic memory and devices, as well as for problems that require the stochasticity and probabilistic behaviour, such as in probabilistic neuromorphic applications [231-233], energy-based problems [234,235], as well as combinatorial optimization problems [225,235].

Appendix A

Analytical Derivation for Harmonic Measurement

In this section, we derive the analytical formula for evaluating the effective fields due to current-induced SOT in the presence of an external applied magnetic field through low-frequency harmonic Hall voltage measurements.

A1 Magnetization Angle Due to Effective Magnetic Fields

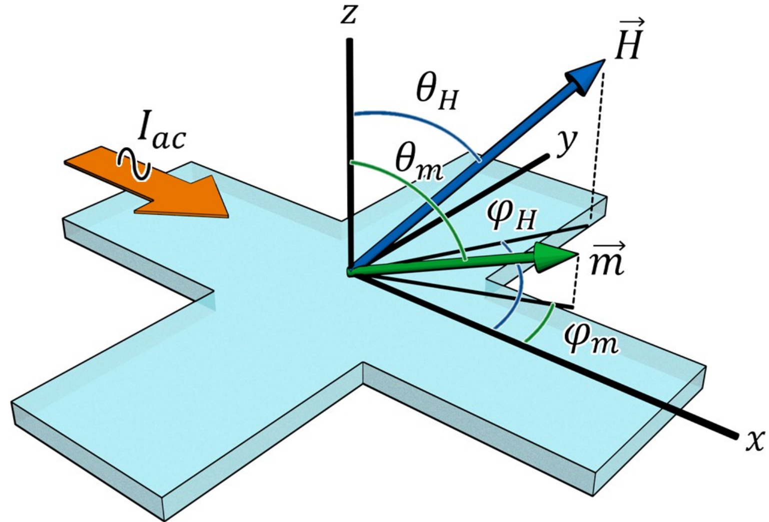

Figure 56: Schematic of a Hall cross structure.

An AC current-induced effective field ΔH_i can change the magnetization angle from its equilibrium polar and azimuthal angles (θ_0, φ_0) by a modulation amplitude $(\Delta\theta, \Delta\varphi)$. The subscript i denotes the component (x, y, z). Using a Hall cross structure as shown in **Figure 56**, the SOT efficiency can be quantitatively characterised through adiabatic (low frequency) anomalous Hall voltage measurements. The magnetic energy of the system can be expressed by:

$$E = -K_{\perp}\cos^2\theta - K_{\parallel}\sin^2\theta\sin^2\varphi - \vec{M}\cdot\vec{H} \tag{60}$$

where $\vec{M}$ and $\vec{H}$ are the magnetization and external magnetic field vectors, respectively. The magnetization and external magnetic field directions are represented by (θ, φ) and (θ_H, φ_H), respectively. The first two terms in equation (59), $K_\perp = K_u - \frac{1}{2}(N_z - N_x)M_s^2$ and $K_\parallel = \frac{1}{2}(N_x - N_y)M_s^2$, are the effective anisotropy energies perpendicular (OOP) and parallel (IP) to the xy plane, respectively. N_x, N_y and N_z are the demagnetization factors. The third term is the Zeeman energy which minimizes when $\vec{M}$ is parallel to $\vec{H}$. $\vec{M}$ and $\vec{H}$ can be described by:

$$\vec{M} = M_s\hat{m} = M_s \begin{pmatrix} \sin\theta\cos\varphi \\ \sin\theta\sin\varphi \\ \cos\theta \end{pmatrix} \tag{61}$$

$$\vec{H} = H \begin{pmatrix} \sin\theta_H\cos\varphi_H \\ \sin\theta_H\sin\varphi_H \\ \cos\theta_H \end{pmatrix} = \begin{pmatrix} H_x \\ H_y \\ H_z \end{pmatrix} \tag{62}$$

where M_s is the saturation magnetization and $\hat{m}$ is the magnetization unit vector.

A2 Determining the Equilibrium Magnetization Direction

The equilibrium magnetization direction (θ_0, φ_0) is determined when the system is at its energy minima. For strong PMA materials, $K_\parallel \ll K_\perp$, and the IP anisotropy energy $K_\parallel$ can be neglected. Then, θ_0 and φ_0 can be determined by setting the energy derivative with respect to θ and φ to zero:

$$\begin{aligned} \frac{\partial E}{\partial \theta} &= 0 \\ &= 2K_\perp \sin\theta_0\cos\theta_0 \\ &\qquad - M_sH[\cos\theta_0\sin\theta_H(\cos\varphi_0\cos\varphi_H \\ &\qquad + \sin\varphi_0\sin\varphi_H) - \sin\theta_0\cos\theta_H] \end{aligned} \tag{63}$$

$$\frac{\partial E}{\partial \varphi} = 0$$
$$= -M_s H \sin\theta_0 \sin\theta_H \sin(\varphi_H - \varphi_0) \tag{64}$$

The OOP effective anisotropy field can be represented as $H_{k,eff} \equiv 2K_\perp/M_s$ and substituted into Eq. (5):

$$\frac{\partial E}{\partial \theta} = H_{k,eff} \cos\theta_0 \sin\theta_0 - H[\cos\theta_0 \sin\theta_H (\cos\varphi_0 \cos\varphi_H + \sin\varphi_0 \sin\varphi_H) - \sin\theta_0 \cos\theta_H] \tag{65}$$

Using small angle approximation such that $\theta_0 \ll 1$ and $\cos\theta_0 \approx 1$, $\partial E/\partial\theta$ simplifies to:

$$\frac{\partial E}{\partial \theta} \approx H_{k,eff} \sin\theta_0 - H(\cos\varphi_0 \sin\theta_H \cos\varphi_H + \sin\varphi_0 \sin\theta_H \sin\varphi_H - \sin\theta_0 \cos\theta_H) \tag{66}$$

$$H_{k,eff} \sin\theta_0 = H(\cos\varphi_0 \sin\theta_H \cos\varphi_H + \sin\varphi_0 \sin\theta_H \sin\varphi_H - \sin\theta_0 \cos\theta_H) = H_x \cos\varphi_0 + H_y \sin\varphi_0 - H_z \sin\theta_0 \tag{67}$$

$$\theta_0 = \sin^{-1} \frac{(H_x \cos\varphi_0 + H_y \sin\varphi_0)}{H_{k,eff} + H_z} \tag{68}$$

Similarly, for $\partial E/\partial\varphi$:

$$\frac{\partial E}{\partial \varphi} \approx -M_s(-H_x \sin\theta_0 \sin\varphi_0 + H_y \sin\theta_0 \cos\varphi_0) = 0 \tag{69}$$

$$\varphi_0 = \tan^{-1}\frac{H_y}{H_x} \tag{70}$$

A3 Effect of Current-Induced Effective Fields on the Magnetization

The modulation amplitudes $(\Delta\theta, \Delta\varphi)$ describing the change in magnetization angle from the equilibrium value as a result of the current-induced effective field $\Delta\vec{H} = \sum_{i=x,y,z} \Delta H_i$ are given by

$$\Delta\theta = \sum_{i=x,y,z} \frac{\partial\theta}{\partial H_i}\Delta H_i \tag{71}$$

$$\Delta\varphi = \sum_{i=x,y,z} \frac{\partial\varphi}{\partial H_i}\Delta H_i \tag{72}$$

$\frac{\partial\theta}{\partial H_i}$ and $\frac{\partial\varphi}{\partial H_i}$ describe the rate of change in magnetization angle due to ΔH_i, and can be solved by the following relations:

$$\begin{aligned}\frac{\partial}{\partial H_i}\left(\frac{\partial E}{\partial\theta}\right) &= 0 \\ &= \Big[2K_{eff}\cos 2\theta_0 \\ &\quad - M_s H[-\sin\theta_0 \sin\theta_H (\cos\varphi_0 \cos\varphi_H \\ &\quad + \sin\varphi_0 \sin\varphi_H) - \cos\theta_0 \cos\theta_H]\Big]\frac{\partial\theta}{\partial H_i} \\ &\quad + \Big[-K_{\parallel}\sin 2\varphi_0 \sin 2\theta_0 \\ &\quad - M_s H[\cos\theta_0 \sin\theta_H (-\sin\varphi_0 \cos\varphi_H \\ &\quad + \cos\varphi_0 \sin\varphi_H)]\Big]\frac{\partial\varphi}{\partial H_i} - M_s f_i\end{aligned} \tag{73}$$

$$\frac{\partial}{\partial H_i}\left(\frac{\partial E}{\partial \varphi}\right) = 0$$

$$\begin{aligned}
&= [-K_{\parallel} \sin 2\theta_0 \sin 2\varphi_0 \\
&\quad + M_s H(\cos\theta_0 \sin\varphi_0 \sin\theta_H \cos\varphi_H \\
&\quad - \cos\theta_0 \cos\varphi_0 \sin\theta_H \sin\varphi_H)] \frac{\partial \theta}{\partial H_i} \\
&\quad + [-2K_{\parallel} \sin^2\theta_0 \cos 2\varphi_0 \\
&\quad + M_s H \sin\theta_0 \sin\theta_H \,(\sin\varphi_H \sin\varphi_0 \\
&\quad + \cos\varphi_0 \cos\varphi_H)] \frac{\partial \varphi}{\partial H_i} - M_s g_i
\end{aligned} \tag{74}$$

where $\vec{f} = \frac{d}{d\theta_0}\begin{pmatrix} \sin\theta_0 \cos\varphi_0 \\ \sin\theta_0 \sin\varphi_0 \\ \cos\theta_0 \end{pmatrix}$ and $\vec{g} = \frac{d}{d\varphi_0}\begin{pmatrix} \sin\theta_0 \cos\varphi_0 \\ \sin\theta_0 \sin\varphi_0 \\ \cos\theta_0 \end{pmatrix}$

Similarly, letting $H_{k,eff} \equiv 2K_{\perp}/M_s$ and $H_{\parallel} \equiv 2K_{\parallel}/M_s$

$$\begin{aligned}
\frac{\partial}{\partial H_i}\left(\frac{\partial E}{\partial \theta}\right) &= \Big[\cos 2\theta_0 \left(H_{eff} - H_{\parallel} \sin^2\varphi_0\right) \\
&\quad - H[-\sin\theta_0 \sin\theta_H \,(\cos\varphi_0 \cos\varphi_H \\
&\quad + \sin\varphi_0 \sin\varphi_H) - \cos\theta_0 \cos\theta_H]\Big] \frac{\partial \theta}{\partial H_i} \\
&\quad + \Big[-\frac{H_{\parallel}}{2} \sin 2\varphi_0 \sin 2\theta_0 \\
&\quad + H[\cos\theta_0 \sin\theta_H \,(\sin\varphi_0 \cos\varphi_H \\
&\quad - \cos\varphi_0 \sin\varphi_H)]\Big] \frac{\partial \varphi}{\partial H_i} - f_i \\
&= 0
\end{aligned} \tag{75}$$

$$\frac{\partial}{\partial H_i}\left(\frac{\partial E}{\partial \varphi}\right) = \left[-\frac{H_{\parallel}}{2}\sin 2\theta_0 \sin 2\varphi_0 \right.$$
$$+ H[\cos\theta_0 \sin\theta_H (\sin\varphi_0 \cos\varphi_H$$
$$\left. - \cos\varphi_0 \sin\varphi_H)]\right]\frac{\partial \theta}{\partial H_i}$$
$$+ [-H_{\parallel} \sin^2\theta_0 \cos 2\varphi_0 \tag{76}$$
$$+ H \sin\theta_0 \sin\theta_H (\sin\varphi_H \sin\varphi_0$$
$$+ \cos\varphi_0 \cos\varphi_H)]\frac{\partial \varphi}{\partial H_i} - g_i$$
$$= 0$$

Let the following pre-factors be represented by:

$$F_0 \equiv \frac{H_{\parallel}}{2}\sin 2\theta_0 \sin 2\varphi_0 - \cos\theta_0 (H_x \sin\varphi_0 - H_y \cos\varphi_0)$$

$$F_1 \equiv F_3 - CF_0$$

$$F_2 \equiv -H_{\parallel} \sin^2\theta_0 \cos 2\varphi_0 + H \sin\theta_0 \sin\theta_H (\sin\varphi_H \sin\varphi_0 + \cos\varphi_0 \cos\varphi_H)$$

$$F_3 \equiv \cos 2\theta_0 \left(H_{eff} - H_{\parallel} \sin^2\varphi_0\right) + \vec{H}\cdot\widehat{m}$$

$$C \equiv \frac{F_0}{F_2}$$

Then,

$$\frac{\partial}{\partial H_i}\left(\frac{\partial E}{\partial \theta}\right) = F_3 \frac{\partial \theta}{\partial H_i} - F_0 \frac{\partial \varphi}{\partial H_i} - f_i \tag{77}$$
$$= 0$$

$$\frac{\partial}{\partial H_i}\left(\frac{\partial E}{\partial \varphi}\right) = -F_0 \frac{\partial \theta}{\partial H_i} - F_2 \frac{\partial \varphi}{\partial H_i} - g_i \tag{78}$$
$$= 0$$

Using Cramer's rule to determine $\frac{\partial\theta}{\partial H_i}$ and $\frac{\partial\varphi}{\partial H_i}$:

$$\frac{\partial\theta}{\partial H_i} = \frac{f_i + Cg_i}{F_1} \tag{79}$$

$$\frac{\partial\varphi}{\partial H_i} = \frac{F_0 f_i + F_3 g_i}{F_2 F_3 - F_0^2} = \frac{F_0 f_i + F_3 g_i}{F_1 F_2} \tag{80}$$

The modulation amplitudes with no approximation made expand to

$$\Delta\theta = \sum_{i=x,y,z} \frac{f_i - Cg_i}{F_1}\Delta H_i = \frac{\begin{pmatrix} \Delta H_x \cos\theta_0 \cos\varphi_0 \\ \Delta H_y \cos\theta_0 \sin\varphi_0 \\ -\Delta H_z \sin\theta_0 \end{pmatrix} + C\begin{pmatrix} -\Delta H_x \sin\theta_0 \sin\varphi_0 \\ \Delta H_y \sin\theta_0 \cos\varphi_0 \\ 0 \end{pmatrix}}{F_1} \tag{81}$$

$$\Delta\varphi = \sum_{i=x,y,z} \frac{F_0 f_i - F_3 g_i}{F_1 F_2}\Delta H_i = \frac{F_0\begin{pmatrix} \Delta H_x \cos\theta_0 \cos\varphi_0 \\ \Delta H_y \cos\theta_0 \sin\varphi_0 \\ -\Delta H_z \sin\theta_0 \end{pmatrix} + F_3\begin{pmatrix} -\Delta H_x \sin\theta_0 \sin\varphi_0 \\ \Delta H_y \sin\theta_0 \cos\varphi_0 \\ 0 \end{pmatrix}}{F_1 F_2} \tag{82}$$

To simplify the above equations, we can assume that $|H_\parallel| \ll |H \sin\theta_H|, |H_\perp|$, such that the in-plane anisotropy field is negligible, then $\varphi_0 = \varphi_H$:

$$C' \equiv \frac{H_\parallel \sin\theta_0 \cos\theta_0 \sin 2\varphi_H}{-H_\parallel \sin\theta_0 \cos 2\varphi_H + H \sin\theta_H}$$

$$\Delta\theta = \frac{\begin{pmatrix} \Delta H_x \cos\theta_0 \cos\varphi_H \\ \Delta H_y \cos\theta_0 \sin\varphi_H \\ -\Delta H_z \sin\theta_0 \end{pmatrix} + C' \begin{pmatrix} -\Delta H_x \sin\theta_0 \sin\varphi_H \\ \Delta H_y \sin\theta_0 \cos\varphi_H \\ 0 \end{pmatrix}}{F_1'} \tag{83}$$

$$= \frac{\cos\theta_0 \left(\Delta H_x \cos\varphi_H + \Delta H_y \sin\varphi_H\right) + \sin\theta_0 \left[C'\left(-\Delta H_x \sin\varphi\right.\right.}{\cos 2\theta_0 \left(H_\perp - H_\parallel \sin^2\varphi_H\right) + H\cos(\theta_H - \theta_0) - C'\left(\frac{H}{2}\right.}$$

$$\Delta\varphi = \frac{A}{B} \tag{84}$$

where

$$A = H_\parallel \sin\theta_0 \sin 2\varphi_H \left[\cos^2\theta_0 \left(\Delta H_x \cos\varphi_H + \Delta H_y \sin\varphi_H\right) - \frac{\Delta H_z}{2} \sin 2\theta_0\right]$$
$$+ \sin\theta_0 \left(\cos 2\theta_0 \left(H_{eff} - H_I \sin^2\varphi_H\right)\right.$$
$$\left. + H\cos(\theta_H - \theta_0)\right)(\Delta H_y \cos\varphi_H - \Delta H_x \sin\varphi_H)$$

$$B = \left[\cos 2\theta_0 \left(H_{eff} - H_\parallel \sin^2\varphi_H\right) + H\cos(\theta_H - \theta_0)\right.$$
$$\left. - C'\left(\frac{H_I}{2} \sin 2\theta_0 \sin 2\varphi_H\right)\right] [-H_\parallel \sin^2\theta_0 \cos 2\varphi_0$$
$$+ H\sin\theta_0 \sin\theta_H]$$

When the in-plane component of the external field is directed along the x or y axis, $\varphi_H = n\frac{\pi}{2}$ for $n \geq 0$ and $\sin 2\varphi_H = 0$

$$\Delta\theta = \frac{\cos\theta_0 \left(\Delta H_x \cos\varphi_H + \Delta H_y \sin\varphi_H\right) - \Delta H_z \sin\theta_0}{\cos 2\theta_0 \left(H_{eff} - H_I \sin^2\varphi_H\right) + H\cos(\theta_H - \theta_0)} \tag{85}$$

$$\Delta\varphi = \frac{\Delta H_y \cos\varphi_H - \Delta H_x \sin\varphi_H}{H\sin\theta_H - H_I \sin\theta_0 \cos 2\varphi_0} \tag{86}$$

A4 Expression for the Hall voltage

If ΔR_A and ΔR_P represent the peak-to-peak change of the anomalous and planar Hall resistance, respectively

$$V_{xy} = IR_{xy} = \frac{1}{2} I\Delta R_A \cos\theta + \frac{1}{2} I\Delta R_P \sin^2\theta \sin 2\varphi \tag{87}$$

An AC current $I = I_{ac} \sin\omega t$ can modulate the magnetization angles such that $\theta \to \theta_0 + \Delta\theta$ and $\varphi \to \varphi_0 + \Delta\varphi$, then

$$\begin{aligned} V_{xy} \approx \frac{1}{2} I_{ac} \sin\omega t \, \Delta R_A \left(\cos\theta_0 + \left(\frac{d}{d\theta}\cos\theta_0\right)\Delta\theta\right) \\ + \frac{1}{2} I_{ac} \sin\omega t \, \Delta R_P \left(\sin^2\theta_0 \right. \\ \left. + \left(\frac{d}{d\varphi}\sin^2\theta_0\right)\Delta\theta\right)\left(\sin\ 2\varphi_0 \right. \\ \left. + \left(\frac{d}{d\varphi}\sin 2\varphi_0\right)\Delta\varphi\right) \end{aligned} \tag{88}$$

Replacing ΔH_i with $\Delta H \sin\omega t$, and consequentially effect on the magnetization will modulate $\Delta\theta$ and $\Delta\varphi$ to $\Delta\theta \sin\omega t$ and $\Delta\varphi \sin\omega t$, respectively:

$$
\begin{aligned}
V_{xy} \approx\ & \frac{1}{2} I_{ac} \sin \omega t\, \Delta R_A (\cos\theta_0 - \sin\theta_0\, \Delta\theta \sin\omega t) \\
& + \frac{1}{2} I_{ac} \sin\omega t\, \Delta R_P (\sin^2\theta_0 \\
& + \sin 2\theta_0\, \Delta\theta \sin\omega t)(\sin\ 2\varphi_0 \\
& + 2\cos 2\varphi_0\, \Delta\varphi \sin\omega t) \\
=\ & \frac{1}{2} I_{ac} \Delta R_A \left(\sin\omega t \cos\theta_0 - \sin\theta_0\, \Delta\theta \left(\frac{1}{2} - \frac{1}{2}\cos 2\omega t \right) \right) \\
& + \frac{1}{2} I_{ac} \Delta R_P \left[\left(\sin\omega t \sin^2\theta_0 \sin\ 2\varphi_0 \right. \right. \\
& \left. + \sin^2\theta_0\, 2\cos 2\varphi_0\, \Delta\varphi \left(\frac{1}{2} - \frac{1}{2}\cos 2\omega t \right) \right) \\
& + \left(\sin 2\theta_0\, \Delta\theta \left(\frac{1}{2} - \frac{1}{2}\cos 2\omega t \right) \sin\ 2\varphi_0 \right. \\
& \left. \left. + \sin 2\theta_0\, \Delta\theta \sin^3\omega t\, 2\cos 2\varphi_0\, \Delta\varphi \right) \right] \\
=\ & \frac{1}{2} I_{ac} R_A \left(\sin\omega t \cos\theta_0 - \frac{1}{2}\sin\theta_0\, \Delta\theta \right. \\
& \left. + \frac{1}{2}\sin\theta_0\, \Delta\theta \cos 2\omega t \right) \\
& + \frac{1}{2} I_{ac} \Delta R_P \left[(\sin\omega t \sin^2\theta_0 \sin\ 2\varphi_0 \right. \\
& + \sin^2\theta_0 \cos 2\varphi_0\, \Delta\varphi \\
& - \sin^2\theta_0 \cos 2\varphi_0\, \Delta\varphi \cos 2\omega t) \\
& + \left(\frac{1}{2}\sin\ 2\varphi_0 \sin 2\theta_0\, \Delta\theta \right. \\
& - \frac{1}{2}\sin\ 2\varphi_0 \sin 2\theta_0\, \Delta\theta \cos 2\omega t \\
& \left. \left. + \sin 2\theta_0\, \Delta\theta \sin^3\omega t\, 2\cos 2\varphi_0\, \Delta\varphi \right) \right]
\end{aligned} \tag{89}
$$

Keeping terms up to the second harmonics, V_{xy} can be represented in the following way:

$$V_{xy} = V_0 + V_\omega \sin\omega t + V_{2\omega} \cos 2\omega t \tag{90}$$

where

$$V_0 = \frac{1}{2} I_{ac} \left[\left(-\frac{1}{2}\Delta R_A \sin\theta_0 + \frac{1}{2}\Delta R_P \sin 2\varphi_0 \sin 2\theta_0 \right) \Delta\theta + (\Delta R_P \sin^2\theta_0 \cos 2\varphi_0)\Delta\varphi \right]$$

$$V_\omega = \frac{1}{2}[(\Delta R_A \cos\theta_0) + (\Delta R_P \sin^2\theta_0 \sin 2\varphi_0)] I_{ac} \tag{91}$$

$$V_{2\omega} = \frac{1}{2} I_{ac} \left[\left(\frac{1}{2}\Delta R_A \sin\theta_0 - \frac{1}{2}\Delta R_P \sin 2\varphi_0 \sin 2\theta_0 \right) \Delta\theta - (\Delta R_P \sin^2\theta_0 \cos 2\varphi_0)\Delta\varphi \right]$$

The second harmonic voltage $V_{2\omega}$ contains information of the current-induced effective fields ΔH_i that causes $\Delta\theta$ and $\Delta\varphi$ to oscillate in sync. The current-induced field $\Delta\vec{H}$ can be decomposed into two components of SOT: (i) The damping-like term $\Delta\vec{H}_{DL} \equiv a_J \hat{m} \times \hat{y}$, and (ii) the field-like term $\Delta\vec{H}_{FL} \equiv b_J \hat{y}$. a_J and b_J correspond to the damping-like and field-like term, respectively. Here, $\hat{y}$ is the spin polarization direction of the injected electron.

A5 Angular Dependence of the SOT Effective Fields for Out-Of-Plane Magnetized Systems

For a perpendicularly magnetized system, and assuming that the equilibrium directions do not deviate far from the z-axis, then $\varphi_0 = \varphi_H$

$$\sin 2\theta_0 \left(K_{eff} - K_I \sin^2 \varphi_0\right) - M_s H[\cos\theta_0 \sin\theta_H (\cos\varphi_0 \cos\varphi_H + \sin\varphi_0 \sin\varphi_H) - \sin\theta_0 \cos\theta_H] = -K_I \sin^2\theta_0 \sin 2\varphi_0 - M_s H \sin\theta_0 \sin\theta_H \sin(\varphi_H - \varphi_0) \quad (92)$$

Approximating for small angles such that $\theta_0 \to \theta_0' \ll 1$, then $\cos\theta_0' \approx 1$ and $\sin\theta_0' \approx \theta_0'$. Taking terms linear with θ_0'

$$\sin 2\theta_0 \left(K_{eff} - K_I \sin^2 \varphi_H\right) - M_s H \sin\theta_H + M_s H \sin\theta_0 \cos\theta_H = 0$$

$$\theta_0'\left(H_{eff} - H_I \sin^2 \varphi_H\right) - H \sin\theta_H + H\theta_0' \cos\theta_H = 0 \quad (93)$$

$$\theta_0' = \frac{H \sin\theta_H}{\left(H_{eff} - H_I \sin^2\varphi_H\right) \pm H\cos\theta_H}$$

Assuming negligible in-plane anisotropy such that $|H_I| \ll |H \sin\theta_H|$, $\varphi_0 = \varphi_H$, and simplifying for small angles using the relation $\cos\theta = \sqrt{1 - \sin^2\theta} \approx 1 - \frac{1}{2}\sin^2\theta$:

$$V_\omega \approx \left[\frac{1}{2}\Delta R_A \left(1 - \frac{1}{2}\left(\frac{H\sin\theta_H}{H_{eff} \pm H\cos\theta_H}\right)^2\right) + \frac{1}{2}\Delta R_P \sin 2\varphi_0 \left(\frac{H\sin\theta_H}{H_{eff} \pm H\cos\theta_H}\right)^2\right] I_{ac}$$

$$V_{2\omega} \approx \frac{1}{2}\left[\left(\frac{1}{2}\Delta R_A \sin\theta_0 - \frac{1}{2}\Delta R_P \sin 2\varphi_0 \sin 2\theta_0\right)\Delta\theta - (\Delta R_P \sin^2\theta_0 \cos 2\varphi_0)\Delta\varphi\right] I_{ac} \quad (94)$$

$$\Delta\theta = \frac{\cos\theta_0' \left(\Delta H_x \cos\varphi_H + \Delta H_y \sin\varphi_H\right) - \Delta H_z \sin\theta_0'}{\cos 2\theta_0' \left(H_{eff} - H_I \sin^2\varphi_H\right) + H\cos(\theta_H - \theta_0')} \tag{95}$$

$$\Delta\varphi = \frac{\Delta H_y \cos\varphi_H - \Delta H_x \sin\varphi_H}{H\sin\theta_H - H_I \sin\theta_0' \cos 2\varphi_0} \tag{96}$$

$$\begin{aligned} V_\omega \approx \frac{1}{2} I_{ac} \Bigg[\Delta R_A \left(1 - \frac{1}{2}\left(\frac{H\sin\theta_H}{H_{eff} \pm H\cos\theta_H}\right)^2\right) \\ + \left(\Delta R_P \left(\frac{H\sin\theta_H}{H_{eff} \pm H\cos\theta_H}\right)^2 \sin 2\varphi_H\right)\Bigg] \end{aligned} \tag{97}$$

$$\begin{aligned} V_{2\omega} \approx \frac{1}{4} I_{ac} \big[(\Delta R_A - 2\Delta R_P \sin 2\varphi_H)\big(\Delta H_x \cos\varphi_H \\ + \Delta H_y \sin\varphi_H\big) \\ - (2\Delta R_P \cos 2\varphi_H)\big(\Delta H_y \cos\varphi_H \\ - \Delta H_x \sin\varphi_H\big)\big] \left(\frac{H\sin\theta_H}{\left(H_{eff} \pm H\cos\theta_H\right)^2}\right) \end{aligned} \tag{98}$$

$$b_\omega = \frac{\partial^2 V_\omega}{\partial H^2} = \left[\frac{I_{ac}}{2}\left(\Delta R_A - \left(\frac{1}{2}\Delta R_A + \Delta R_P \sin 2\varphi_H\right)\frac{\partial^2}{\partial H^2}\left(\left(\frac{H \sin\theta_H}{H_{eff} \pm H\cos\theta_H}\right)^2\right)\right)\right]$$

$$= \left[\frac{I_{ac}}{2}\left(\Delta R_A - \left(\frac{1}{2}\Delta R_A + \Delta R_P \sin 2\varphi_H\right) \times 2H_{eff}\left(\frac{\cos^2\theta_H}{\left(H_{eff} + H\cos\theta_H\right)^4}\right) \times \left(H_{eff} - 2H\cos\theta_H\right)\right)\right] \tag{99}$$

External fields are in plane, $\theta_H = 90°$

$$b_\omega = \frac{\partial^2 V_\omega}{\partial H^2} = \left[\frac{I_{ac}}{2}\left(\Delta R_A - \left(\frac{1}{2}\Delta R_A + \Delta R_P \sin 2\varphi_H\right)\frac{\partial^2}{\partial H^2}\left(\left(\frac{H \sin\theta_H}{H_{eff} \pm H\cos\theta_H}\right)^2\right)\right)\right]$$

$$\approx \frac{I_{ac}}{2H_{eff}^2}\left(\pm\Delta R_A + 2\Delta R_P \sin 2\varphi_H\right) \tag{100}$$

$$b_{2\omega} = \frac{\partial V_{2\omega}}{\partial H} \approx \frac{I_{ac}}{2H_{eff}^2}\left[\left(\frac{1}{2}\Delta R_A - \Delta R_P \sin 2\varphi_H\right)\left(\Delta H_x \cos\varphi_H + \Delta H_y \sin\varphi_H\right) - (\Delta R_P \cos 2\varphi_H)\left(\Delta H_y \cos\varphi_H - \Delta H_x \sin\varphi_H\right)\right] \tag{101}$$

Then, the ratio

$$B = \frac{b_{2\omega}}{b_\omega} = \frac{\left(\frac{1}{2}\Delta R_A - \Delta R_P \sin 2\varphi_H\right)\left(\Delta H_x \cos\varphi_H + \Delta H_y \sin\varphi_H\right) - (\Delta R_}{(\pm\Delta R_A + 2\Delta R_P \sin 2\varphi_H)} = \frac{\left(\Delta H_x \cos\varphi_H + \Delta H_y \sin\varphi_H\right)}{2} - \frac{(\Delta R_P \cos 2\varphi_H)\left(\Delta H_y \cos\varphi_H - \Delta H_x \sin\varphi_H\right)}{(\pm\Delta R_A + 2\Delta R_P \sin 2\varphi_H)} \tag{102}$$

Consolidating the current-induced effective fields:

$$B = \left(\frac{1}{2}\cos\varphi_H + \frac{\xi \cos 2\varphi_H \sin\varphi_H}{1 + 2\xi \sin 2\varphi_H}\right)\Delta H_x + \left(\frac{1}{2}\sin\varphi_H - \frac{\xi \cos 2\varphi_H \cos\varphi_H}{1 + 2\xi \sin 2\varphi_H}\right)\Delta H_y = \alpha\Delta H_x + \beta\Delta H_y \tag{103}$$

A singular measurement at φ_H is insufficient to discern the individual current-induced effective fields ΔH_x and ΔH_y. Another orientation φ_H' is necessary in order to eliminate one of the two, such that

$$B(\varphi_H) - B'(\varphi_H') = \Delta H_{x,y} \tag{104}$$

Using the following equivalent representations

$$\sin\varphi_H = \sin(180 - \varphi_H) = \cos(90 - \varphi_H)$$
$$\cos\varphi_H = -\cos(180 - \varphi_H) = \sin(90 - \varphi_H) \tag{105}$$

Then

$$\alpha = -\frac{1}{2}\sin(90 - \varphi_H) - \frac{\xi\cos(180 - 2\varphi_H)\cos(90 - \varphi_H)}{1 + 2\xi\sin(180 - 2\varphi_H)} = \beta' \tag{106}$$

$$\beta = \frac{1}{2}\cos(90 - \varphi_H) - \frac{\xi\cos(180 - \varphi_H)\sin(90 - \varphi_H)}{1 + 2\xi\sin(180 - \varphi_H)} = \alpha' \tag{107}$$

where $\varphi'_H = 90 - \varphi_H$. This results in

$$B_{\varphi_H} = \alpha\Delta H_x + \beta\Delta H_y = \beta'\Delta H_x + \alpha'\Delta H_y = B_{\varphi'_H} \tag{108}$$

then

$$\Delta H_x = \frac{\beta B_{\varphi H} - \alpha B_{90° - \varphi_H}}{\beta^2 - \alpha^2} \tag{109}$$

$$\Delta H_y = \frac{\alpha B_{\varphi H} - \beta B_{90° - \varphi_H}}{\alpha^2 - \beta^2} \tag{110}$$

Equations (101) and (102) enables the evaluation of current-induced effective fields for arbitrary φ.

Appendix B
SPICE Circuit Modelling

Simulated Program with Integrated Circuit Emphasis (SPICE) circuit modelling is introduced and developed in this section. The three main pieces of physics used in the circuit simulation of the SOT-driven logic device and half-adder in Chapter 6 are presented as circuit models: (i) the Landau-Lifshitz-Gilbert (LLG) equation with spin torques due to the spin Hall effect, (ii) the SHE in NM HM layers using the two-channel model previously described in Chapter 2, and (iii) the anomalous Hall effect (AHE) used to measure the magnetization state of the device. These models will be prepared as separate modules to be called upon in the main spintronic logic device model. The development of the SPICE circuit models are built from scratch with reference to the formalisms developed by Bonhomme *et al*. and Hong *et al*. [204,205]. The SPICE software used is LTSpice, a free analogue circuit simulator software by Analogue Devices (previously Linear Technologies). SPICE circuit simulation has the advantage of modelling more complex circuits without having to physically construct them.

B1 Landau-Lifshitz-Gilbert Model

The dynamics of the magnetization $\vec{m}$ due to an effective field and the torque due to the SHE is given by the LLGS equation:

$$\frac{d\vec{m}}{dt} = -\gamma\mu_0\vec{m} \times \vec{H}_{eff} + \alpha\vec{m} \times \frac{d\vec{m}}{dt} + \gamma a'\vec{m} \times (\vec{m} \times \vec{I}_s) \qquad (111)$$

where the RHS of the equation are represented by the precession, damping, and SOT terms, respectively. Here, we have also defined a reduce damping-like coefficient $a' \equiv \alpha/I_s = \hbar/2eM_sV$, and pure spin current vector $\vec{I}_s \equiv I_s\vec{\sigma}$ where I_s is the magnitude of the pure spin current and $\vec{\sigma}$ is the spin current polarization.

The direction components of the pure spin current $\vec{I}_s$ is denoted as $I_{s,\eta}$ where $\eta = x, y, z$. equation (111) can be transformed to its explicit form, resulting in:

$$\frac{1+\alpha^2}{\mu_0\gamma}\frac{d\vec{m}}{dt} = -\vec{m}\times\vec{H}_{eff} - \alpha\vec{m}\times\left(\vec{m}\times\vec{H}_{eff}\right) - \alpha a'\vec{m}\times\vec{I}_s + a'\vec{m}\times(\vec{m}\times\vec{I}_s) \tag{112}$$

Here, the effective field $\vec{H}_{eff}$ contains the uniaxial anisotropy field $\vec{H}_{uni}$ and external applied field $\vec{H}_{ext}$ terms, such that $\vec{H}_{eff} = \vec{H}_{uni} + \vec{H}_{ext}$. The components can then be represented explicitly as:

$$\begin{aligned}\frac{1+\alpha^2}{\mu_0\gamma}\frac{dm_x}{dt} &= -m_yH_{eff,z} + m_zH_{eff,y} \\ &\quad - \alpha\left[\left(m\cdot\vec{H}_{eff}\right)m_x - H_{eff,x}\right] \\ &\quad - \alpha a'\left[m_yI_{s,z} - m_zI_{s,y}\right] + a'\left[\left(\vec{m}\cdot\vec{I}_s\right)m_x - I_{s,x}\right]\end{aligned} \tag{113}$$

$$\begin{aligned}\frac{1+\alpha^2}{\mu_0\gamma}\frac{dm_y}{dt} &= -m_xH_{eff,z} + m_zH_{eff,x} \\ &\quad - \alpha\left[\left(m\cdot\vec{H}_{eff}\right)m_y - H_{eff,y}\right] \\ &\quad - \alpha a'\left[m_xI_{s,z} - m_zI_{s,x}\right] + a'\left[\left(\vec{m}\cdot\vec{I}_s\right)m_y - I_{s,y}\right]\end{aligned} \tag{114}$$

$$\begin{aligned}\frac{1+\alpha^2}{\mu_0\gamma}\frac{dm_z}{dt} &= -m_xH_{eff,y} + m_yH_{eff,x} \\ &\quad - \alpha\left[\left(m\cdot\vec{H}_{eff}\right)m_z - H_{eff,z}\right] \\ &\quad - \alpha a'\left[m_xI_{s,y} - m_yI_{s,x}\right] + a'\left[\left(\vec{m}\cdot\vec{I}_s\right)m_z - I_{s,z}\right]\end{aligned} \tag{115}$$

The above equations (113), (114), and (115) now comprise of a constant factor $C \equiv \frac{1+\alpha^2}{\gamma}$ multiplied by the time derivative of the components of magnetization $\frac{d}{dt}m_i$, on the LHS, and scalar functions $f_i(\vec{m}, \vec{H}_{eff}, \vec{I}_s)$ on the RHS, where $i = x, y, z$. The three equations then have the following form,

$$C\frac{dm_i}{dt} = f_i(\vec{m}, \vec{H}_{eff}, \vec{I}_s) \quad (116)$$

Equation (116) resembles that of a capacitor-current equation $C\frac{d}{dt}V = I$, where the function f_i can be modelled as a behavioural current source attached to a capacitor with capacitance C, and m_i is analogous to voltage V. The Gilbert damping coefficient α and gyromagnetic ratio γ are all contained within the constant factor C. Equations (113), (114), and (115) can therefore be represented by equivalent capacitor circuits. The components of the effective field $\vec{H}_{eff}$ are modelled as voltage sources in series. Finally, the spin current vector $\vec{I}_s$ is represented by current sources. The current-capacitor circuit for the LLGS module, effective field voltage source circuit, and spin current source circuit are shown in **Figure 57**.

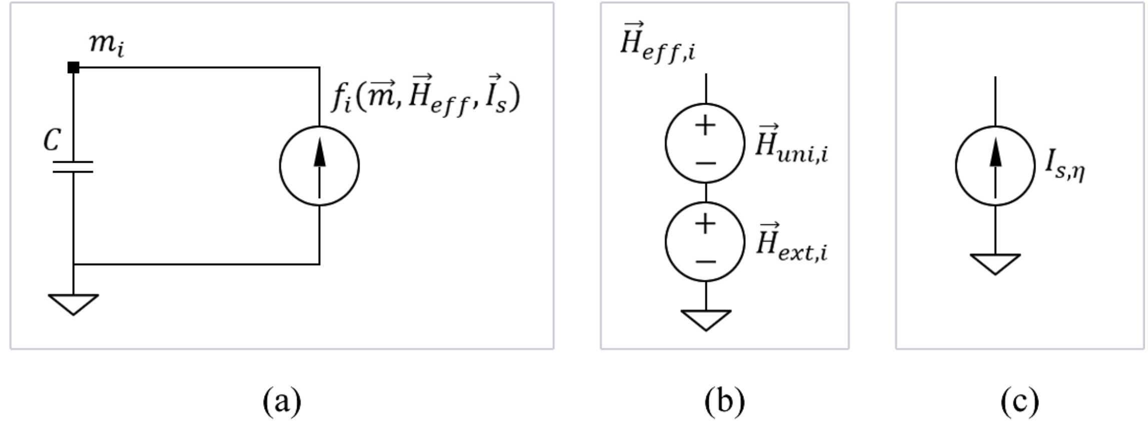

Figure 57: (a) Current-capacitor circuit for the LLGS module. (b) Voltage source for the effective fields. (c) Current source for the spin currents.

Using this equivalent circuit to model the magnetization dynamics, effective fields, and spin currents, magnetization switching dynamics due to field and spin current can be simulated within LTSpice.

B2 Spin Hall Effect Module

The spin Hall effect module is developed here by solving the 3D charge and spin diffusion equations given by:

$$\nabla^2 V_c = 0 \tag{117}$$

$$\nabla^2 V_{s,\eta} = \frac{V_{s,\eta}}{l_{sd}^2} \tag{118}$$

where $\eta = x, y, z$ is the direction of spin polarization. For a 6-sided NM conductor of length l, width w, and thickness t, a charge current flowing along the $+x$ direction will result in polarised spins accumulating along the lateral surfaces of the conductor as illustrated in **Figure 57** (a):

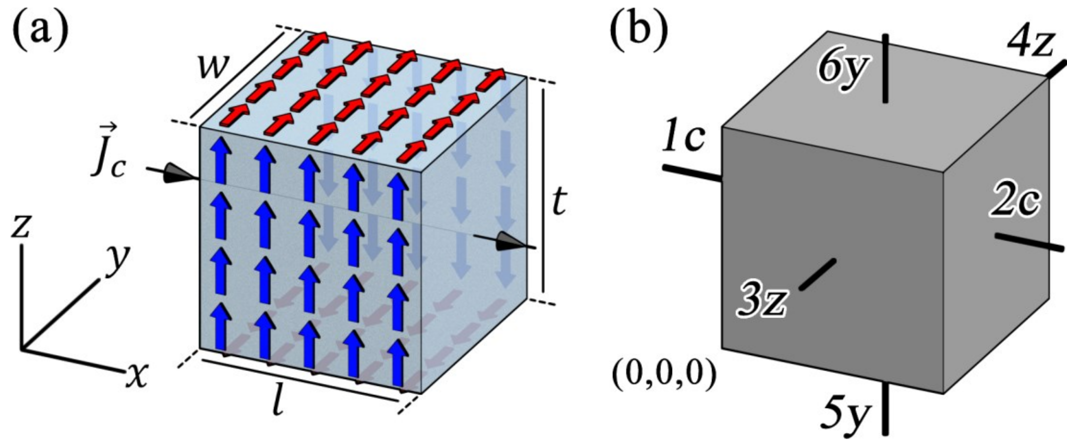

Figure 58: (a) Spin current along the $+\boldsymbol{x}$ direction and polarised spins accumulating along the $\boldsymbol{x}$-$\boldsymbol{y}$ and $\boldsymbol{x}$-$\boldsymbol{z}$ surfaces. (b) Terminals for each side of the NM block.

The direction of spin polarization is orthogonal to both the charge and spin current flow, so that opposite spins accumulate on opposite lateral surfaces of the conductor. There is no spin accumulation of spins polarized along the direction of charge current flow. Taking the origin in space as illustrated in **Figure 58** (b), this gives the boundary conditions as:

$$\begin{aligned} V_c &= V_c(x) \\ V_{s,x} &= \text{constant} \\ V_{s,y} &= V_{s,y}(z) \end{aligned} \tag{119}$$

$$V_{s,z} = V_{s,z}(y)$$

According to Eq. (119), the charge potential varies along x, and there is no spin accumulation of x-polarized electrons along the y-z surfaces. The y-polarised spin current $I_{s,y}$ flows along the z-axis and accumulates at the surfaces with normal along the z-axis. The z-polarised spin current $I_{s,z}$ flows along the y-axis and accumulates at the surfaces with normal along the y-axis. Using these boundary conditions, the diffusion equations can then be written as:

$$\partial_x^2 V_c = 0 \tag{120}$$

$$\partial_y^2 V_{s,z} = \frac{V_{s,z}}{l_{sd}^2} \tag{121}$$

$$\partial_z^2 V_{s,y} = \frac{V_{s,y}}{l_{sd}^2} \tag{122}$$

The terminal potentials for defining the block in LTSpice are labelled by running numbers 1 thru 6, and accompanied by a letter indicating charge (c) or spin polarization (y, z) direction as shown in **Figure 58** (b). Letting the origin (0,0,0) of the block of length l, width w, and thickness t to be the coordinate origin, then the terminal potentials can be written as

$$V_c(0) \equiv V_c^1 \text{ and } V_c(l) \equiv V_c^2 \tag{123}$$

$$V_{s,z}(0) \equiv V_{s,z}^3 \text{ and } V_{s,z}(w) \equiv V_{s,z}^4 \tag{124}$$

$$V_{s,y}(0) \equiv V_{s,y}^5 \text{ and } V_{s,y}(t) \equiv V_{s,y}^6 \tag{125}$$

The solutions for $V_c(x)$, $V_{s,z}(y)$, and $V_{s,y}(z)$ are then

$$V_c(x) = \frac{V_c^2 x + V_c^1 (l - x)}{l} \tag{126}$$

$$V_{s,z}(y) = \frac{V_{s,z}^{4} \sinh\left(\frac{y}{l_{sd}}\right) + V_{s,z}^{3} \sinh\left(\frac{w-y}{l_{sd}}\right)}{\sinh\left(\frac{w}{l_{sd}}\right)} \tag{127}$$

$$V_{s,y}(z) = \frac{V_{s,y}^{6} \sinh\left(\frac{z}{l_{sd}}\right) + V_{s,y}^{5} \sinh\left(\frac{t-z}{l_{sd}}\right)}{\sinh\left(\frac{t}{l_{sd}}\right)} \tag{128}$$

Equations (26) – (28) describe the charge and spin potentials variation in space, and serve as the boundary conditions for expanding the generalized Ohm's law:

$$J_c = -\sigma\left(\partial_x V_C(x) + \theta_{SH}\partial_z V_{s,y}(z) - \theta_{SH}\partial_y V_{s,z}(y)\right) \tag{129}$$

$$J_{sz} = -\sigma\left(\theta_{SH}\partial_x V_c(x) + \partial_y V_{s,z}(y)\right) \tag{130}$$

$$J_{sy} = -\sigma\left(-\theta_{SH}\partial_x V_c(x) + \partial_z V_{s,y}(z)\right) \tag{131}$$

Using equations (26) – (31), the charge and spin currents through the terminal nodes can now be solved for specific dimensions. The charge current I_C^1 injected through terminal *1c* is given by:

$$
\begin{aligned}
I_c^1 &= \int J_c^x \, dA \\
&= \int_0^w dy \int_0^t dz \left[-\sigma \left(\partial_x V_C(x) + \theta_{SH} \partial_z V_{s,y}(z) \right.\right. \\
&\qquad \left.\left. - \theta_{SH} \partial_y V_{s,z}(y) \right) \right]_{x=0} \\
&= -\sigma \left[wt\partial_x \frac{V_c^2 x + V_c^1 (l-x)}{l} \Big|_{x=0} + \theta_{SH} w \int_0^t \frac{\partial V_{s,y}(z)}{\partial z} dz \right. \\
&\qquad \left. - \theta_{SH} t \int_0^w \frac{\partial V_{s,z}(y)}{\partial y} dy \right] \\
&= -\frac{\sigma wt}{l} (V_c^2 - V_c^1) - \sigma \theta_{SH} w \left(V_{s,y}^6 - V_{s,y}^5 \right) \\
&\qquad + \sigma \theta_{SH} t \left(V_{s,z}^4 - V_{s,z}^3 \right) \\
&= -G_0 (V_c^2 - V_c^1) - \beta_1 G_0 \left(V_{s,y}^6 - V_{s,y}^5 \right) + \beta_2 G_0 \left(V_{s,z}^4 - V_{s,z}^3 \right)
\end{aligned}
\tag{132}
$$

where the following substitutions have been made

$$
\begin{aligned}
G_0 &\equiv \frac{\sigma wt}{l} \\
\beta_1 &\equiv \frac{\theta_{SH} l}{w} \\
\beta_2 &\equiv \frac{\theta_{SH} l}{t}
\end{aligned}
\tag{133}
$$

Similarly, for charge current I_C^2 through terminal *2c*:

$$
\begin{aligned}
I_c^2 &= \frac{\sigma wt}{l} (V_c^2 - V_c^1) + \sigma \theta_{SH} w \left(V_{s,y}^6 - V_{s,y}^5 \right) \\
&\qquad - \sigma \theta_{SH} t \left(V_{s,z}^4 - V_{s,z}^3 \right) \\
&= G_0 (V_c^2 - V_c^1) + \beta_1 G_0 \left(V_{s,y}^6 - V_{s,y}^5 \right) - \beta_2 G_0 \left(V_{s,z}^4 - V_{s,z}^3 \right) \\
&= -I_c^1
\end{aligned}
\tag{134}
$$

The first term on the RHS of Eq. (132) and (134) is Ohm's law, which governs the conventional charge current conduction. The last two terms representing the spin-to-charge conversion due to ISHE is dependent on the spin potentials, which we label as I_0:

$$I_0 \equiv -\beta_1 G_0\left(V_{s,y}^6 - V_{s,y}^5\right) + \beta_2 G_0\left(V_{s,z}^4 - V_{s,z}^3\right) \tag{135}$$

Since $I_c^1 = -I_c^2$, equations (132) and (134) can be represented by a circuit as shown in **Figure 59**. The circuit has a conductance G_0.

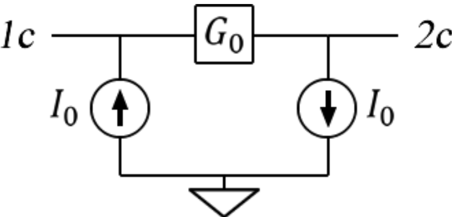

Figure 59: Circuit representation of charge current flowing across terminals *1c* and *2c*.

Similarly, solving for terminal *3z*, we obtain the following expression for the *z* polarized spin current:

$$I_{s,z}^3 = -\sigma t \theta_{SH}(V_c^2 - V_c^1) + \sigma \frac{lt}{\lambda_{sd}} V_{s,z}^3 \coth \frac{w}{\lambda_{sd}} - \sigma \frac{lt}{\lambda_{sd}} V_{s,z}^4 \operatorname{csch} \frac{w}{\lambda_{sd}} \tag{136}$$

Equation (26) can be rearranged using the identity $\coth x = \operatorname{csch} x + \tanh \frac{x}{2}$:

$$
\begin{aligned}
I_{s,z}^{3} &= -\sigma t\theta_{SH}(V_c^2 - V_c^1) + \sigma\frac{lt}{\lambda_{sd}}V_{s,z}^{3}\left[\operatorname{csch}\frac{w}{\lambda_{sd}} + \tanh\frac{w}{2\lambda_{sd}}\right] \\
&\qquad - \sigma\frac{lt}{\lambda_{sd}}V_{s,z}^{4}\operatorname{csch}\frac{w}{\lambda_{sd}} \\
&= -\sigma t\theta_{SH}(V_c^2 - V_c^1) + \sigma\frac{lt}{\lambda_{sd}}\operatorname{csch}\left(\frac{w}{\lambda_{sd}}\right)\left(V_{s,z}^{3} - V_{s,z}^{4}\right) \\
&\qquad + \sigma\frac{lt}{\lambda_{sd}}\tanh\left(\frac{w}{2\lambda_{sd}}\right)\left(V_{s,z}^{3} - 0\right) \\
&= -I_0^z + G_2^z(V_{s,z}^{3} - V_{s,z}^{4}) + G_1^z(V_{s,z}^{3} - 0)
\end{aligned}
\tag{137}
$$

where we have define the charge to spin conversion due to SHE I_0^z, conductance along the y direction G_2^z, and shunt conductance due to spin-flip processes G_1^z for z polarized spins:

$$
\begin{aligned}
I_0^z &\equiv \sigma t\theta_{SH}(V_c^2 - V_c^1) \\
G_2^z &\equiv \frac{lt}{\lambda_{sd}}\operatorname{csch}\left(\frac{w}{\lambda_{sd}}\right) \\
G_1^z &\equiv \sigma\frac{lt}{\lambda_{sd}}\tanh\left(\frac{w}{2\lambda_{sd}}\right)
\end{aligned}
\tag{138}
$$

charge to spin conversion due to SHE $I_0^z \equiv \sigma t\theta_{SH}(V_c^2 - V_c^1)$, conductance along the y direction $G_2^z \equiv \frac{lt}{\lambda_{sd}}\operatorname{csch}\left(\frac{w}{\lambda_{sd}}\right)$, and shunt conductance due to spin-flip processes $G_1^z \equiv \sigma\frac{lt}{\lambda_{sd}}\tanh\left(\frac{t}{2\lambda_{sd}}\right)$. Repeating the process for y polarized spin currents along terminals *5y* and *6y*, we define the charge to spin conversion due to SHE I_0^y, conductance along the y direction G_2^y, and shunt conductance due to spin-flip processes G_1^y for y polarized spins:

$$
I_0^y \equiv \sigma w\theta_{SH}(V_c^2 - V_c^1) \tag{139}
$$

$$G_2^y \equiv \frac{lw}{\lambda_{sd}} \operatorname{csch}\left(\frac{t}{\lambda_{sd}}\right)$$

$$G_1^y \equiv \sigma \frac{lw}{\lambda_{sd}} \tanh\left(\frac{t}{2\lambda_{sd}}\right)$$

The circuit representation for z polarised spin current flowing through terminals *3z* and *4z*, and y polarized spin current flowing through terminals *5y* and *6y* are shown in **Figure 60**.

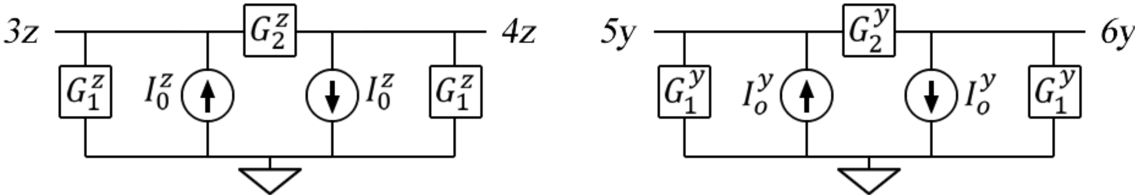

Figure 60: Circuit representation of $\boldsymbol{x}$ and $\boldsymbol{y}$ polarized spin current flow with respective spin flip conductance for spin attenuation.

B3 Anomalous Hall Effect Module

The anomalous Hall voltage V_{AHE} due to the anomalous Hall effect (AHE) can be modelled as a behavioural voltage source. The V_{AHE} due to a probing charge current I_c is given by:

$$V_{AHE} = \frac{R_{AHE} M_s}{t_{FM}} m_z I_c \tag{140}$$

where R_{AHE} is the anomalous Hall coefficient, M_s is the saturation magnetization, t_{FM} is the thickness of the FM layer, and m_Z is the z component of the unit magnetization.

B4 SPICE Simulations

Using the above LLG module, a transient simulation is performed on LTSpice. The following material parameters for the FM layer were used: $M_s = 6.757 \times 10^5$ A/m, $H_k = 1$ T, $\alpha = 0.02$. At time $t = 0$ s, $\vec{m} = (0,0,1)$ and a field $H_x = 1$ T was applied. The plots in **Figure 61** (a) shows the three components of

magnetization m_x, m_y, and m_z over a simulation time of 3 ns. **Figure 61** (b) shows the 3D trajectory of the magnetization $\vec{m}$.

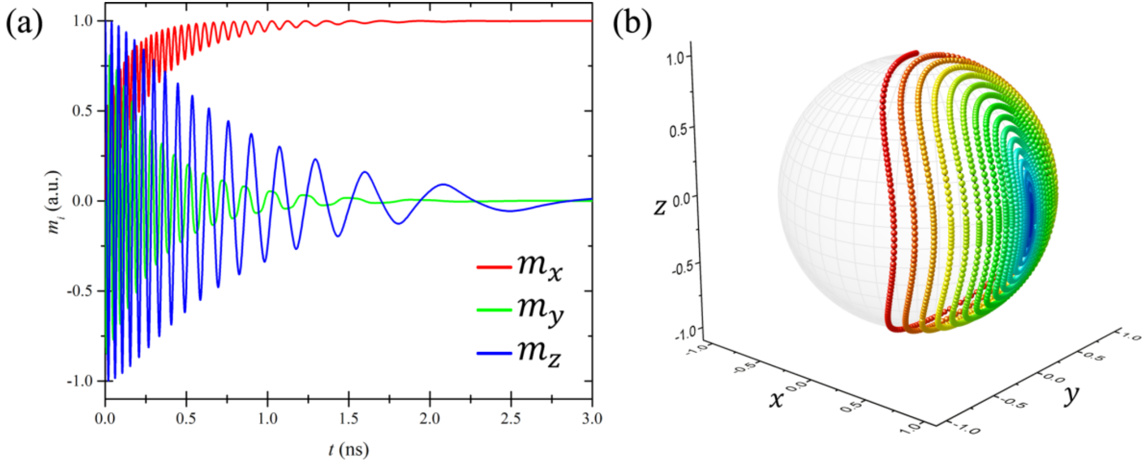

Figure 61: (a) Magnetization components m_x, m_y, and m_z over 3 ns due to an in-plane magnetic field H_x. (b) Magnetization trajectory of the magnetization $\vec{m}$.

Both plots show the magnetization immediately begin to precess about the x axis and gradually settling along the applied field H_x direction due to the non-zero damping parameter. **Figure 62** (a) and (b) show the SPICE plots for an in-plane field H_x and pulse current I applied to the SPICE model, simulating current-induced SOT magnetization switching and reversal of the z-component of the magnetization from +1 (up) to -1 (down).

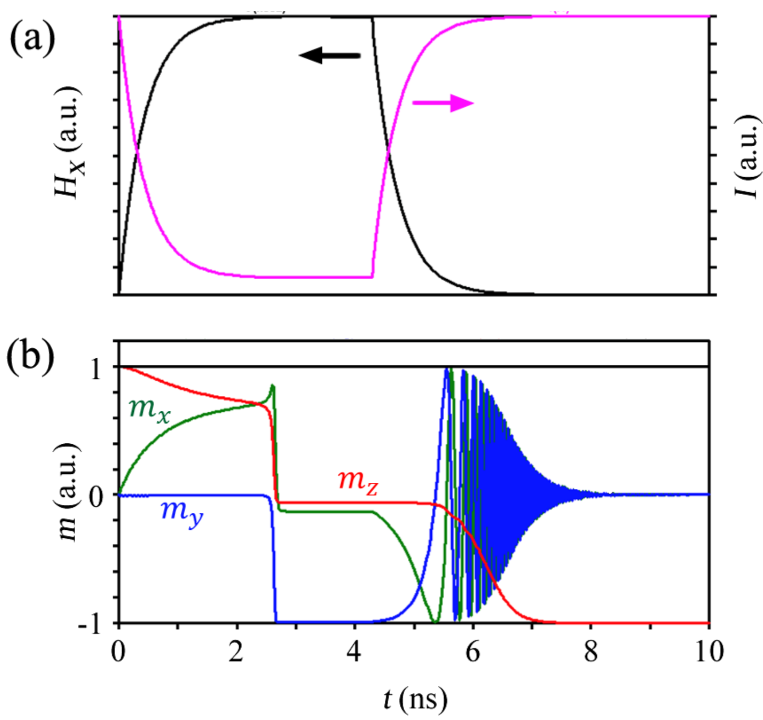

Figure 62: (a) In-plane field H_x (black) and pulse current I (pink) applied to the SPICE model. (b) Magnetization components across 10 ns due to H_x and I.

Appendix C
Implementation of Multistate Device in a Hopfield Network

The Hopfield network, named after and popularized by John Hopfield, is a type of recurrent artificial neural network in which the neurons or nodes share a connection between each other [236]. It can be used in applications such as pattern recognition. In this section, we demonstrate the use of the Hall cross device with multistate, analogue-like behaviour developed in Chapter 4 in a Hopfield network for character recognition. The devices serve as artificial synapse in which is used to store the inter-neuron connection strength, or the weight $w_{m,n}$ between neurons m and n.

C1 Hopfield Network

The Hopfield network was chosen as a platform for demonstrating the SOT-driven multistate device as it required the least number of synaptic weight representations. A graphical representation of an 8-neuron Hopfield network is shown in **Figure 63**.

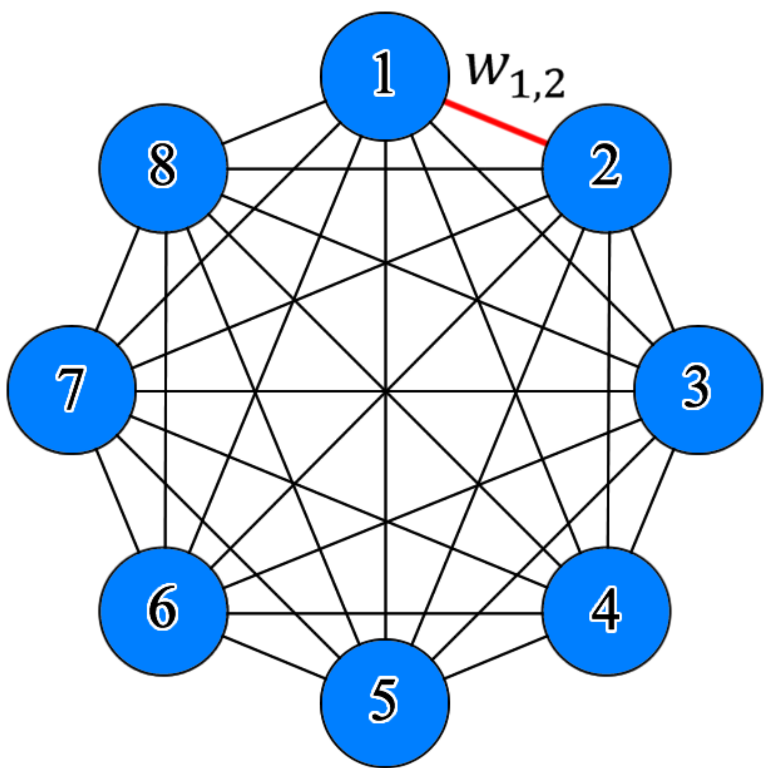

Figure 63: An 8-neuron (node) Hopfield network. The red line represents the synaptic weight $w_{1,2}$ between neurons 1 and 2.

Each neuron shares a synapse with every other neuron, but not back to itself. The synaptic weights are also bi-directional, therefore $w_{m,n} = w_{n,m}$. Therefore, the weights for $N = m \times n$ number of neurons can be represented by:

$$W = \begin{bmatrix} w_{1,1} & \cdots & w_{1,n} \\ \vdots & \ddots & \vdots \\ w_{n,1} & \cdots & w_{n,n} \end{bmatrix} \tag{141}$$

where the diagonal elements are zero, i.e. $w_{m,n} = 0$ for $m = n$, and $w_{m,n} = w_{n,m}$. From this, we can see that the Hopfield network requires $(N^2 - N)/2$ number of synapses to represent n number of neurons.

The neurons represent pixels, and in the case of this demonstration, an array of black and white pixels used to record the letter of the alphabet. The neurons therefore only store binary values of -1 for white and $+1$ for black.

C2 Training

A 5-by-5 array of pixels is used to train the Hopfield network, as shown in **Figure 64**. This network then requires 300 synapses to represent the inter-neuron connection strength.

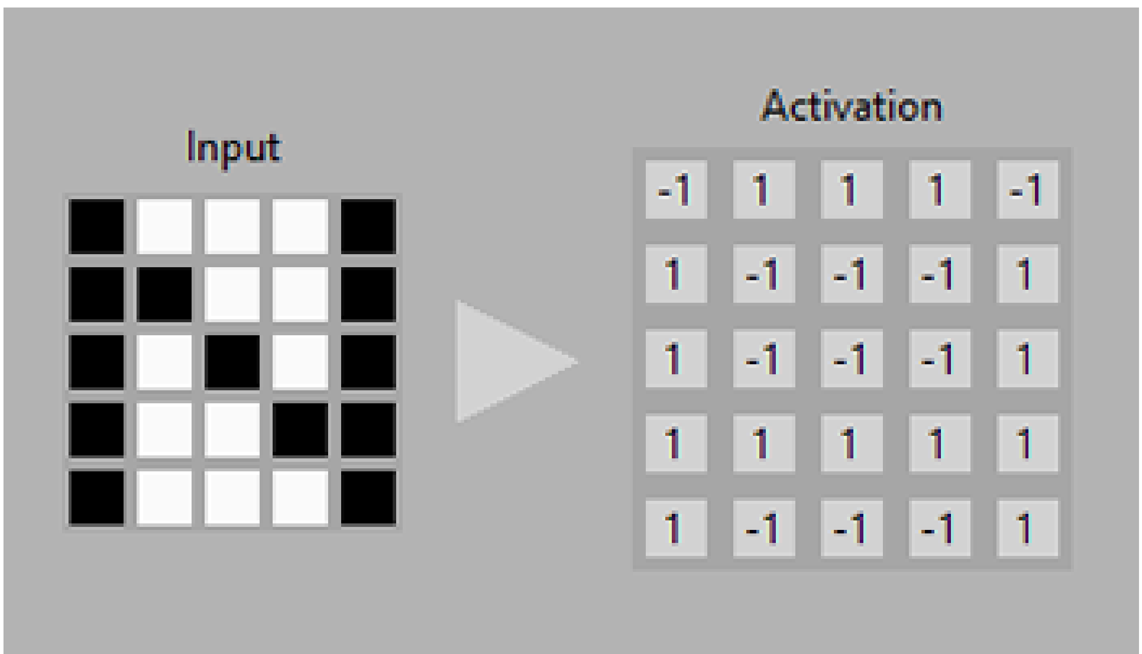

Figure 64: Learning the letter N and converting the white and black pixels to -1 and $+1$, respectively

Upon learning each character, the energy E is calculated using the modified Ising energy equivalent equation across all neurons x.

$$E = -\sum_{m<n} w_{m,n} x_m x_n \tag{142}$$

where x_m and x_n are neurons connected to each other by the synaptic weight $w_{m,n}$. The criteria in which $m < n$ is to prevent double counting. The synaptic weights are calculated and adjusted based on how each pixel relate across patterns. For three patterns learnt, the synaptic weights can be $+3$, $+1$, -1, -3. Therefore, the synaptic weight should be able to represent at least 4 possible

states. **Figure 65** shows the histogram and respective weights across the 300 synapses after learning the letters N, T, and U.

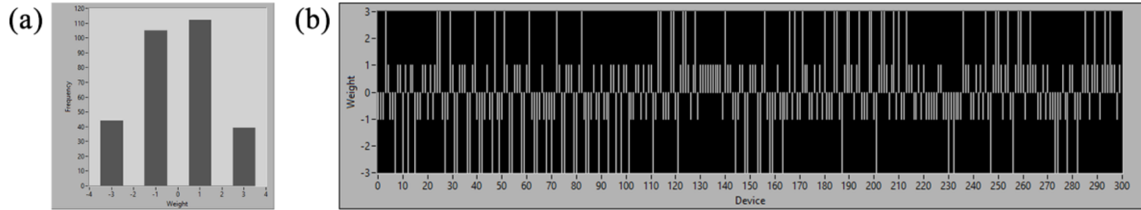

Figure 65: (a) Histogram of weights across 300 synapses for a 5-by-5 array pixel after learning the letters N, T, and U. (b) Individually addressed synapses and their respective weights.

The intent of the SOT-driven Hall cross device with non-volatile multistate characteristics is to store each addressed synaptic weight, such that they can be recalled when required during the solving stage. For this to be implemented on hardware, random access to multiple devices is required.

C3 Hardware Implementation

Typically, measurement and characterization are performed on individual devices. However, in order to access multiple devices, electronic switches and multiplexing is required. Several substrates no larger than 1 cm by 1 cm were fabricated, each containing 20 working devices and wire bonded on to a CCL board as shown in **Figure 66** (a). A PCB cartridge was also designed to accommodate the CCL board and several other soldered-on discrete electronic components and IC chips as shown in **Figure 66** (b). The electronic components and IC chips include multiplexers, demultiplexers, solid state relays, counters, and resistors. These were necessary to allow random access to each Hall cross device representing synapses.

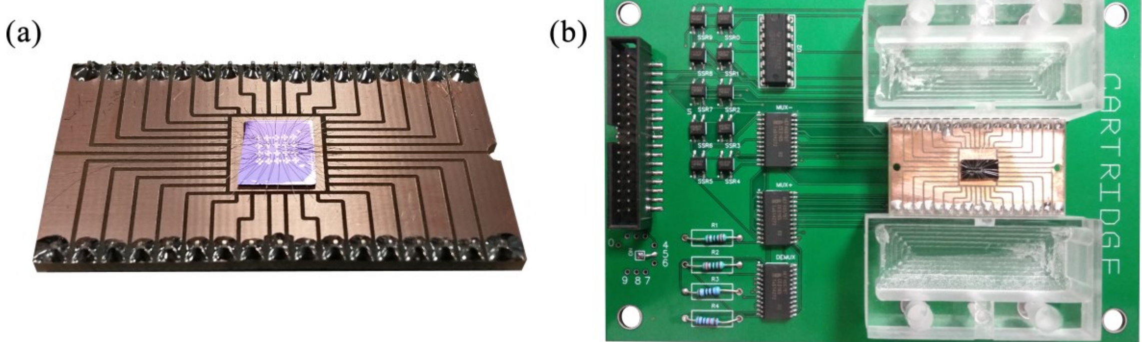

Figure 66: (a) A substrate with 20 devices wire bonded on to a CCL board. (b) A PCB cartridge with mounted CCL board and soldered discrete electronic components and IC chips.

The schematic for the device, hardware, and software control interface is shown in **Figure 67**. Communication to individual cartridges and devices was managed using Arduino and LabVIEW through interfacing add-ons such as LabVIEW Interface for Arduino (LIFA). Programs and sub-routine Virtual Instruments (VI) were written for the device read/write operations and the Hopfield model.

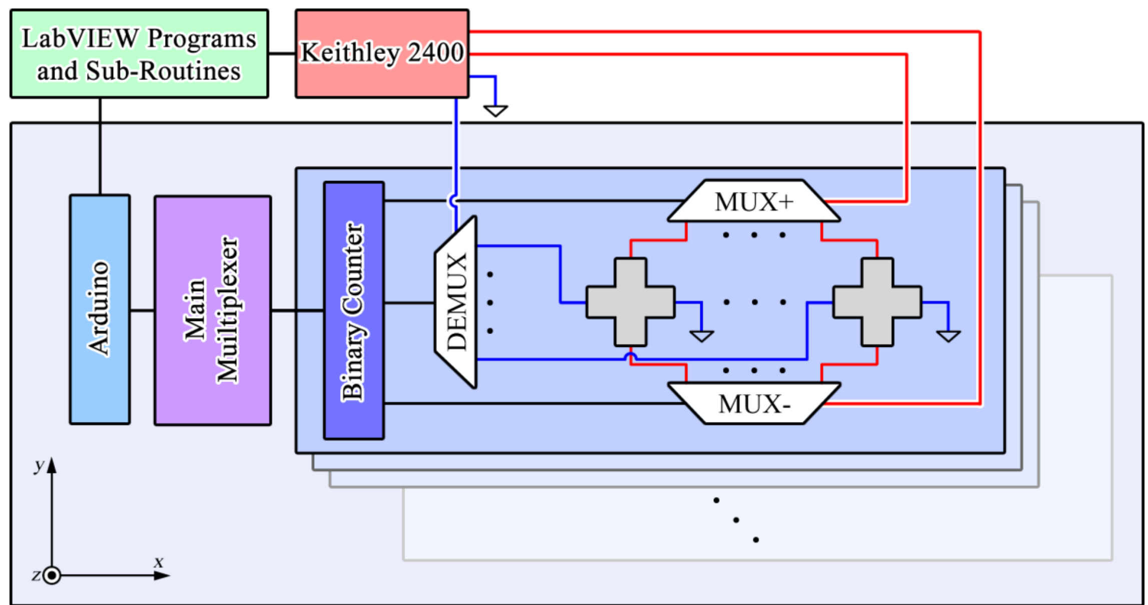

Figure 67: Schematic of SOT device array with controllers.

As each cartridge can hold up to 20 devices as shown in **Figure 68**, multiple cartridges were daisy-chained in order to expand the accessible number of devices.

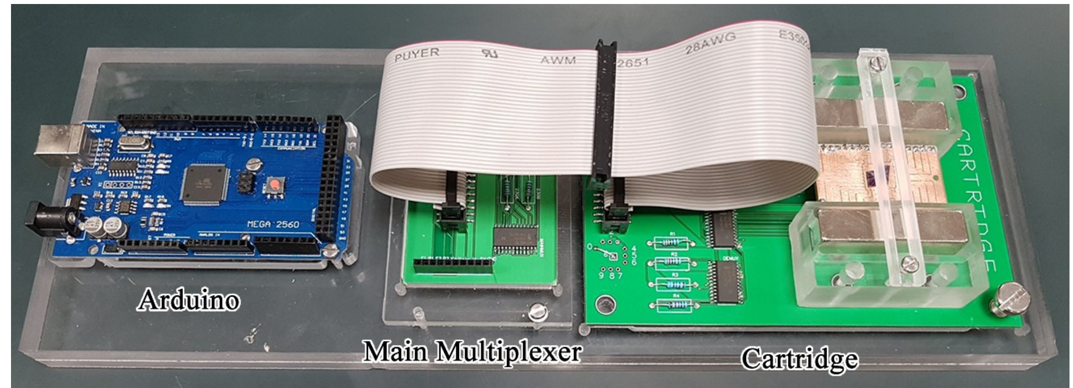

Figure 68: Arduino, main multiplexer, and single cartridge set-up.

Due to device-to-device non-uniformities, each device may perform slightly different from each other. Therefore, all the devices would first require characterization. Using the multiplexer set up, the full $I - R_H$ hysteresis loop was measured across all devices. The useable range of write current I is the region in which there is linear correlation with the Hall resistance R_H as shown in **Figure 69** (a). In order to identify the linear region between up and down states for each device, differentiation on a spline fit was utilized, from which the FWHM range was deemed "linear enough" to serve as the multi-state range of $I - R_H$ values. **Figure 69** (b) shows the first ten devices: #0 thru #9.

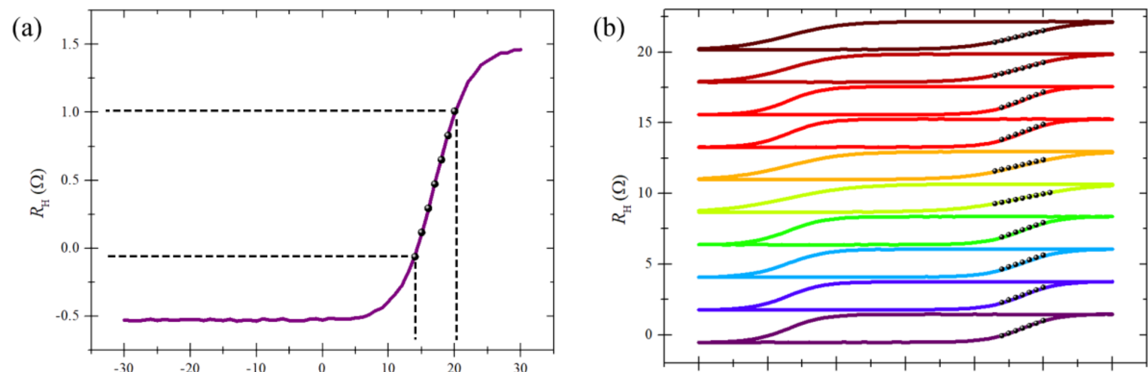

Figure 69: (a) $I - R_H$ hysteresis for Device #0 with linear region indicated by dashed lines for corresponding range of I and R_H. (b) $I - R_H$ hysteresis loops for the first ten devices: #0 thru #9.

The variation in Hall resistance R_H across 300 devices for the current range $14 \text{ mA} \leq I \leq 20 \text{ mA}$ is shown in **Figure 70**. For a 5-by-5 pixel array with three learned patterns, only four values of weights exist: -3, -1, 1, and 3. Therefore, an appropriate current range and interval should be chosen such that the assignment of weights will be distinct with clear thresholds.

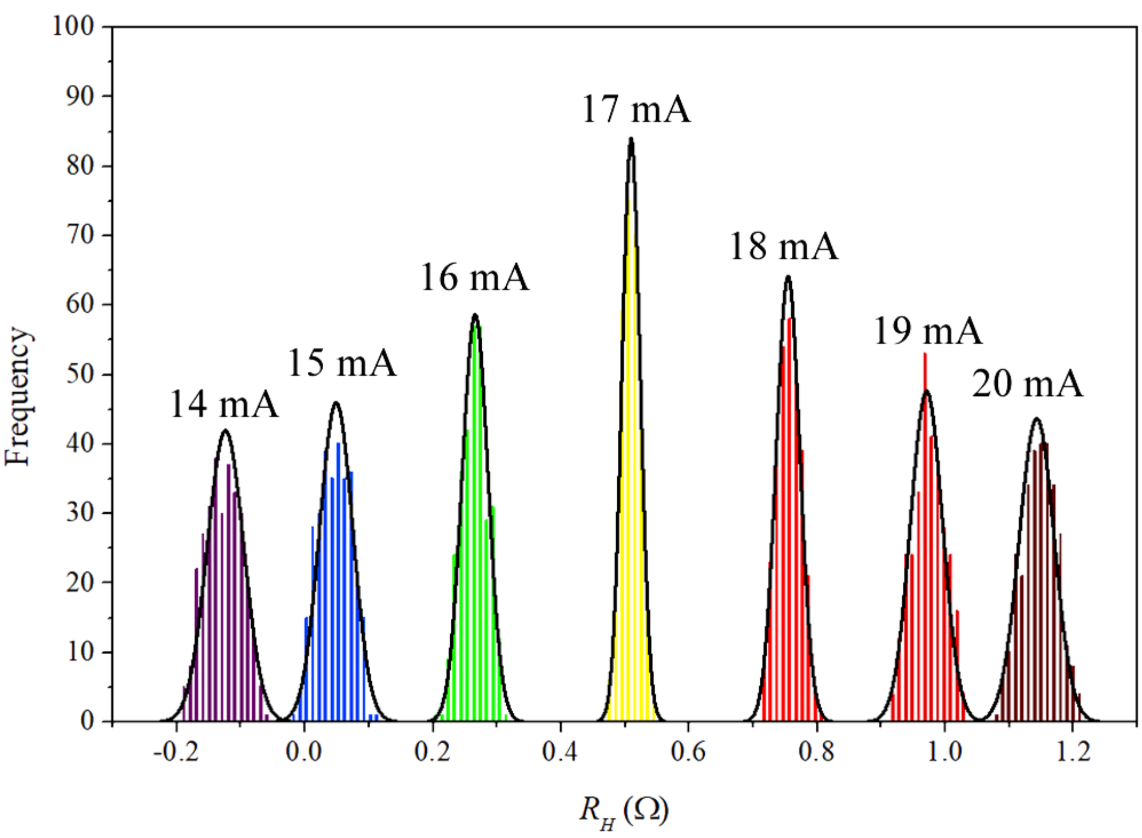

Figure 70: Histogram of R_H frequency for current range $14 \text{ mA} \leq I \leq 20 \text{ mA}$.

Using the SOT-driven Hall cross device with multistate characteristics, the synaptic weight can be mapped on to the magnetization state and corresponding Hall resistance R_H. The multistate non-volatile spintronic memory serves to describe the relationship between neurons m and n. The Hopfield network is then able to resolve noisy or distorted 5-by-5 pixel inputs of the letters "N", "T", and "U" as shown in **Figure 71** using the weights stored in the spintronic synaptic memory.

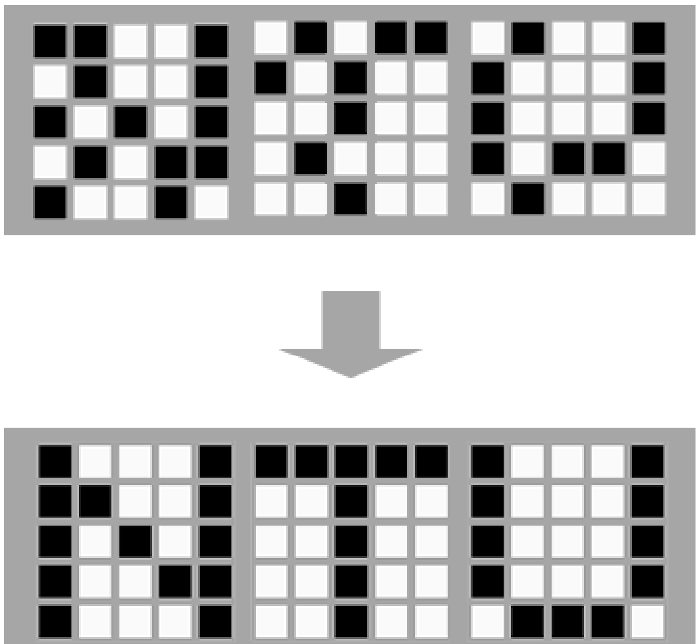

Figure 71: Resolving 5-by-5 pixel characters “N”, “T”, and “U” from noisy or distorted inputs.

Bibliography

1 Wong, H. S. P. & Salahuddin, S. Memory leads the way to better computing. *Nat. Nanotechnol.* **10**, 191-194 (2015).

2 Moore, G. E. Cramming more components onto integrated circuits, Reprinted from Electronics, volume 38, number 8, April 19, 1965, pp.114 ff. *IEEE Solid-State Circuits Society Newsletter* **11**, 33-35 (2006).

3 Borkar, S. & Chien, A. A. The future of microprocessors. *Commun. ACM* **54**, 67–77 (2011).

4 Danowitz, A., Kelley, K., Mao, J., Stevenson, J. P. & Horowitz, M. CPU DB: recording microprocessor history. *Commun. ACM* **55**, 55–63 (2012).

5 Theis, T. N. & Solomon, P. M. It's Time to Reinvent the Transistor! *Science* **327**, 1600-1601 (2010).

6 Nikonov, D. E. & Young, I. A. Overview of Beyond-CMOS Devices and a Uniform Methodology for Their Benchmarking. *Proc. IEEE* **101**, 2498-2533 (2013).

7 Tudu, B. & Tiwari, A. Recent Developments in Perpendicular Magnetic Anisotropy Thin Films for Data Storage Applications. *Vacuum* **146**, 329-341 (2017).

8 Sarwat, S. G. Materials science and engineering of phase change random access memory. *Mater. Sci. Technol.* **33**, 1890-1906 (2017).

9 Endoh, T., Koike, H., Ikeda, S., Hanyu, T. & Ohno, H. An Overview of Nonvolatile Emerging Memories— Spintronics for Working Memories. *IEEE Trans. Emerg. Sel. Topics Circuits Syst.* **6**, 109-119 (2016).

10 Thomson, W. XIX. On the electro-dynamic qualities of metals:--Effects of magnetization on the electric conductivity of nickel and of iron. *Proc. R. Soc. London* **8**, 546-550 (1857).

11 Mott, N. F. & Bohr, N. H. D. The scattering of fast electrons by atomic nuclei. *Proc. R. Soc. A* **124**, 425-442 (1929).

12 Julliere, M. Tunneling between ferromagnetic films. *Phys. Lett. A* **54**, 225-226 (1975).

13 Binasch, G., Grünberg, P., Saurenbach, F. & Zinn, W. Enhanced magnetoresistance in layered magnetic structures with antiferromagnetic interlayer exchange. *Phys. Rev. B* **39**, 4828-4830 (1989).

14 Baibich, M. N. *et al.* Giant Magnetoresistance of (001)Fe/(001)Cr Magnetic Superlattices. *Phys. Rev. Lett.* **61**, 2472-2475 (1988).

15 Miyazaki, T. & Tezuka, N. Giant magnetic tunneling effect in Fe/Al2O3/Fe junction. *J. Magn. Magn. Mater.* **139**, L231-L234 (1995).

16 Moodera, J. S., Kinder, L. R., Wong, T. M. & Meservey, R. Large Magnetoresistance at Room Temperature in Ferromagnetic Thin Film Tunnel Junctions. *Phys. Rev. Lett.* **74**, 3273-3276 (1995).

17 Yuasa, S., Nagahama, T., Fukushima, A., Suzuki, Y. & Ando, K. Giant room-temperature magnetoresistance in single-crystal Fe/MgO/Fe magnetic tunnel junctions. *Nat. Mater.* **3**, 868-871 (2004).

18 Parkin, S. S. P. *et al.* Giant tunnelling magnetoresistance at room temperature with MgO (100) tunnel barriers. *Nat. Mater.* **3**, 862-867 (2004).

19 Ramu, M. *et al.* Spin orbit torque induced asymmetric depinning of chiral Néel domain wall in Co/Ni heterostructures. *Appl. Phys. Lett.* **110**, 162402 (2017).

20 Sethi, P. *et al.* Bi-directional high speed domain wall motion in perpendicular magnetic anisotropy Co/Pt double stack structures. *Sci. Rep.* **7**, 4964 (2017).

21 Krohling, A. C. *et al.* The influence of Cu spacer morphology in Cu/Py/Cu/Co/IrMn spin valves with induced non-collinear spin structures. *J. Magn. Magn. Mater.* **512**, 166985 (2020).

22 Fong, X. *et al.* Spin-Transfer Torque Memories: Devices, Circuits, and Systems. *Proc. IEEE* **104**, 1449-1488 (2016).

23 Prejbeanu, I. L. *et al.* Thermally assisted MRAMs: ultimate scalability and logic functionalities. *J. Phys. D: Appl. Phys* **46**, 074002 (2013).

24 Liu, L. *et al.* Spin-Torque Switching with the Giant Spin Hall Effect of Tantalum. *Science* **336**, 555-558 (2012).

25 Yu, G. *et al.* Switching of perpendicular magnetization by spin–orbit torques in the absence of external magnetic fields. *Nat. Nanotechnol.* **9**, 548-554 (2014).

26 Brataas, A. & Hals, K. M. D. Spin–orbit torques in action. *Nat. Nanotechnol.* **9**, 86-88 (2014).

27 Miron, I. M. *et al.* Perpendicular switching of a single ferromagnetic layer induced by in-plane current injection. *Nature* **476**, 189-193 (2011).

28 Hirsch, J. E. Spin Hall Effect. *Phys. Rev. Lett.* **83**, 1834-1837 (1999).

29 Locatelli, N., Cros, V. & Grollier, J. Spin-torque building blocks. *Nat. Mater.* **13**, 11-20 (2014).

30 Grollier, J., Querlioz, D. & Stiles, M. D. Spintronic Nanodevices for Bioinspired Computing. *Proc. IEEE* **104**, 2024-2039 (2016).

31 Romera, M. *et al.* Vowel recognition with four coupled spin-torque nano-oscillators. *Nature* **563**, 230-234 (2018).

32 Torrejon, J. *et al.* Neuromorphic computing with nanoscale spintronic oscillators. *Nature* **547**, 428-431 (2017).

33 Sharad, M., Yogendra, K. & Roy, K. Dual pillar spin torque nano-oscillator. *Appl. Phys. Lett.* **103**, 152403 (2013).

34 Jenkins, A. S., Alvarez, L. S. E., Freitas, P. P. & Ferreira, R. Nanoscale true random bit generator based on magnetic state transitions in magnetic tunnel junctions. *Sci. Rep.* **9**, 15661 (2019).

35 Verma, S., Murthy, M. S. & Kaushik, B. K. All Spin Logic: A Micromagnetic Perspective. *IEEE Trans. Magn.* **51**, 1-10 (2015).

36 An, Q., Beux, S. L., Connor, I. O., Klein, J. O. & Zhao, W. in *2017 15th IEEE International New Circuits and Systems Conference (NEWCAS).* 317-320.

37 Chen, M., Kim, Y., Yogendra, K. & Roy, K. Domino-Style Spin–Orbit Torque-Based Spin Logic. *IEEE Magn. Lett.* **6**, 1-4 (2015).

38 Sarkar, A., Srinivasan, S., Behin-Aein, B. & Datta, S. in *2011 International Electron Devices Meeting.*

39 Behin-Aein, B., Datta, D., Salahuddin, S. & Datta, S. Proposal for an all-spin logic device with built-in memory. *Nat. Nanotechnol.* **5**, 266-270 (2010).

40 Patra, M. & Maiti, S. K. All-spin logic operations: Memory device and reconfigurable computing. *EPL* **121**, 38004 (2018).

41 Luo, Z. *et al.* Current-driven magnetic domain-wall logic. *Nature* **579**, 214-218 (2020).

42 Allwood, D. A. *et al.* Magnetic Domain-Wall Logic. *Science* **309**, 1688-1692 (2005).

43 Omari, K. A. & Hayward, T. J. Chirality-Based Vortex Domain-Wall Logic Gates. *Phys. Rev. Appl.* **2**, 044001 (2014).

44 Omari, K. A. *et al.* Toward Chirality-Encoded Domain Wall Logic. *Adv. Funct. Mater.* **29**, 1807282 (2019).

45 Gypens, P., Leliaert, J. & Van Waeyenberge, B. Balanced Magnetic Logic Gates in a Kagome Spin Ice. *Phys. Rev. Appl.* **9**, 034004 (2018).

46 Alawein, M., Amara, S. & Fariborzi, H. Multistate Nanomagnetic Logic Using Equilateral Permalloy Triangles. *IEEE Magn. Lett.* **10**, 1-5 (2019).

47 Nikonov, D. E., Bourianoff, G. I. & Ghani, T. in *2011 11th IEEE International Conference on Nanotechnology.* 1384-1388.

48 Debashis, P., Faria, R., Camsari, K. Y. & Chen, Z. Design of Stochastic Nanomagnets for Probabilistic Spin Logic. *IEEE Magn. Lett.* **9**, 1-5 (2018).

49 Bhowmik, D., You, L. & Salahuddin, S. Spin Hall effect clocking of nanomagnetic logic without a magnetic field. *Nat. Nanotechnol.* **9**, 59-63 (2014).

50 Manipatruni, S., Nikonov, D. E. & Young, I. A. All-spin nanomagnetic state elements. *Appl. Phys. Lett.* **103**, 063503 (2013).

51 Mahmoudi, H., Windbacher, T., Sverdlov, V. & Selberherr, S. in *Proceedings of the 2013 9th Conference on Ph.D. Research in Microelectronics and Electronics (PRIME).* 157-160.

52 Matsunaga, S. *et al.* in *2009 Design, Automation & Test in Europe Conference & Exhibition.* 433-435.

53 Wang, M. *et al.* in *2014 12th IEEE International Conference on Solid-State and Integrated Circuit Technology (ICSICT).* 1-4.

54 Mahmoudi, H., Windbacher, T., Sverdlov, V. & Selberherr, S. Implication logic gates using spin-transfer-torque-operated magnetic tunnel junctions for intrinsic logic-in-memory. *Solid State Electron.* **84**, 191-197 (2013).

55 Kuzum, D., Yu, S. & Philip Wong, H. S. Synaptic electronics: materials, devices and applications. *Nanotechnology* **24**, 382001 (2013).

56 Mead, C. Neuromorphic electronic systems. *Proc. IEEE* **78**, 1629-1636 (1990).

57 Drachman, D. A. Do we have brain to spare? *Neurology* **64**, 2004-2005 (2005).

58 Widrow, B., Kim, Y., Park, D. & Perin, J. K. in *Artificial Intelligence in the Age of Neural Networks and Brain Computing* (eds Robert Kozma, Cesare Alippi, Yoonsuck Choe, & Francesco Carlo Morabito) 1-30 (Academic Press, 2019).

59 Izhikevich, E. M. Which model to use for cortical spiking neurons? *IEEE Trans. Neural Netw.* **15**, 1063-1070 (2004).

60 Markram, H., Gerstner, W. & Sjöström, P. J. A History of Spike-Timing-Dependent Plasticity. *Front. Synaptic Neurosci.* **3** (2011).

61 Cao, Y., Rushforth, A., Sheng, Y., Zheng, H. & Wang, K. Tuning a Binary Ferromagnet into a Multistate Synapse with Spin–Orbit-Torque-Induced Plasticity. *Adv. Funct. Mater.* **29**, 1808104 (2019).

62 Lequeux, S. *et al.* A magnetic synapse: multilevel spin-torque memristor with perpendicular anisotropy. *Sci. Rep.* **6**, 31510 (2016).

63 Bhowmik, D. *et al.* On-chip learning for domain wall synapse based Fully Connected Neural Network. *J. Magn. Magn. Mater.* **489**, 165434 (2019).

64 Bhattacharya, T. *et al.* Low-Power (1T1N) Skyrmionic Synapses for Spiking Neuromorphic Systems. *IEEE Access* **7**, 5034-5044 (2019).

65 Srinivasan, G., Sengupta, A. & Roy, K. Magnetic Tunnel Junction Based Long-Term Short-Term Stochastic Synapse for a Spiking Neural Network with On-Chip STDP Learning. *Sci. Rep.* **6**, 29545 (2016).

66 Song, K. M. *et al.* Skyrmion-based artificial synapses for neuromorphic computing. *Nat. Electron.* **3**, 148-155 (2020).

67 Zhang, D., Zeng, L., Zhang, Y., Zhao, W. & Klein, J. O. in *2016 IEEE/ACM International Symposium on Nanoscale Architectures (NANOARCH).* 173-178.

68 Lequeux, S. *et al.* A magnetic synapse: multilevel spin-torque memristor with perpendicular anisotropy. *Sci. Rep.* **6**, 31510 (2016).

69 Borders, W. A. *et al.* Analogue spin–orbit torque device for artificial-neural-network-based associative memory operation. *Appl. Phys. Express* **10**, 013007 (2016).

70 Kurenkov, A., Zhang, C., DuttaGupta, S., Fukami, S. & Ohno, H. Device-size dependence of field-free spin-orbit torque induced magnetization switching in antiferromagnet/ferromagnet structures. *Appl. Phys. Lett.* **110**, 092410 (2017).

71 Sengupta, A., Choday, S. H., Kim, Y. & Roy, K. Spin orbit torque based electronic neuron. *Appl. Phys. Lett.* **106**, 143701 (2015).

72 Chanthbouala, A. *et al.* Vertical-current-induced domain-wall motion in MgO-based magnetic tunnel junctions with low current densities. *Nat. Phys.* **7**, 626-630 (2011).

73 Fan, D., Shim, Y., Raghunathan, A. & Roy, K. STT-SNN: A Spin-Transfer-Torque Based Soft-Limiting Non-Linear Neuron for Low-Power Artificial Neural Networks. *IEEE Trans. Nanotechnol.* **14**, 1013-1023 (2015).

74 Sengupta, A., Shim, Y. & Roy, K. Proposal for an All-Spin Artificial Neural Network: Emulating Neural and Synaptic Functionalities Through Domain Wall Motion in Ferromagnets. *IEEE Trans. Biomed. Circuits. Syst.* **10**, 1152-1160 (2016).

75 Chen, X. *et al.* A compact skyrmionic leaky–integrate–fire spiking neuron device. *Nanoscale* **10**, 6139-6146 (2018).

76 Agrawal, A. & Roy, K. Mimicking Leaky-Integrate-Fire Spiking Neuron Using Automotion of Domain Walls for Energy-Efficient Brain-Inspired Computing. *IEEE Trans. Magn.* **55**, 1-7 (2019).

77 Brigner, W. H. *et al.* Shape-Based Magnetic Domain Wall Drift for an Artificial Spintronic Leaky Integrate-and-Fire Neuron. *IEEE Trans. Electron Devices* **66**, 4970-4975 (2019).

78 Hassan, N. *et al.* Magnetic domain wall neuron with lateral inhibition. *J. Appl. Phys.* **124**, 152127 (2018).

79 Brigner, W. H. *et al.* Graded-Anisotropy-Induced Magnetic Domain Wall Drift for an Artificial Spintronic Leaky Integrate-and-Fire Neuron. *IEEE J. Explor. Solid-State Computat.*, 1-1 (2019).

80 Liyanagedera, C. M., Sengupta, A., Jaiswal, A. & Roy, K. Stochastic Spiking Neural Networks Enabled by Magnetic Tunnel Junctions: From Nontelegraphic to Telegraphic Switching Regimes. *Phys. Rev. Appl.* **8**, 064017 (2017).

81 Cai, J. *et al.* Voltage-Controlled Spintronic Stochastic Neuron Based on a Magnetic Tunnel Junction. *Phys. Rev. Appl.* **11**, 034015 (2019).

82 Poppelbaum, W. J., Afuso, C. & Esch, J. W. in *Proceedings of the November 14-16, 1967, fall joint computer conference* 635–644 (Association for Computing Machinery, Anaheim, California, 1967).

83 Deco, G., Rolls, E. T. & Romo, R. Stochastic dynamics as a principle of brain function. *Prog. Neurobiol.* **88**, 1-16 (2009).

84 Tarequzzaman, M. *et al.* Spin torque nano-oscillator driven by combined spin injection from tunneling and spin Hall current. *Commun. Phys.* **2**, 20 (2019).

85 Vodenicarevic, D., Mizrahi, A., Locatelli, N., Grollier, J. & Querlioz, D. in *2017 European Conference on Circuit Theory and Design (ECCTD).* 1-4.

86 Zahedinejad, M. *et al.* Two-dimensional mutually synchronized spin Hall nano-oscillator arrays for neuromorphic computing. *Nat. Nanotechnol.* **15**, 47-52 (2020).

87 Camsari, K. Y., Sutton, B. M. & Datta, S. p-bits for probabilistic spin logic. *Appl. Phys. Rev.* **6**, 011305 (2019).

88 Borders, W. A. *et al.* Integer factorization using stochastic magnetic tunnel junctions. *Nature* **573**, 390-393 (2019).

89 Friedrich, B. & Herschbach, D. Stern and Gerlach: How a Bad Cigar Helped Reorient Atomic Physics. *Phys. Today* **56**, 53-59 (2003).

90 Schmidt-Böcking, H. *et al.* The Stern-Gerlach experiment revisited. *Eur. Phys. J. H* **41**, 327-364 (2016).

91 Dzyaloshinsky, I. A thermodynamic theory of “weak” ferromagnetism of antiferromagnetics. *J. Phys. Chem. Solids.* **4**, 241-255 (1958).

92 Moriya, T. Anisotropic Superexchange Interaction and Weak Ferromagnetism. *Phys. Rev.* **120**, 91-98 (1960).

93 Schlotter, S., Agrawal, P. & Beach, G. S. D. Temperature dependence of the Dzyaloshinskii-Moriya interaction in Pt/Co/Cu thin film heterostructures. *Appl. Phys. Lett.* **113**, 092402 (2018).

94 Nembach, H. T., Shaw, J. M., Weiler, M., Jué, E. & Silva, T. J. Linear relation between Heisenberg exchange and interfacial Dzyaloshinskii–Moriya interaction in metal films. *Nat. Phys.* **11**, 825-829 (2015).

95 Kim, S. *et al.* Correlation of the Dzyaloshinskii–Moriya interaction with Heisenberg exchange and orbital asphericity. *Nat. Commun.* **9**, 1648 (2018).

96 Kim, N.-H. *et al.* Dependence of interfacial Dzyaloshinskii–Moriya interaction and perpendicular magnetic anisotropy on the thickness of the heavy-metal layer. *Appl. Phys. Express* **10**, 103003 (2017).

97 Fert, A., Cros, V. & Sampaio, J. Skyrmions on the track. *Nat. Nanotechnol.* **8**, 152-156 (2013).

98 Blundell, S. Magnetism in Condensed Matter. *Oxford University Press Inc., New York* (2009).

99 Peng, S. *et al.* Giant interfacial perpendicular magnetic anisotropy in MgO/CoFe/capping layer structures. *Appl. Phys. Lett.* **110**, 072403 (2017).

100 Coey, J. M. D. *Magnetism and Magnetic Materials*. Cambridge University Press (2010).

101 Stoner, E. C. & Wohlfarth, E. P. A mechanism of magnetic hysteresis in heterogeneous alloys. *Philos. Trans. R. Soc. A* **240**, 599-642 (1948).

102 Zhang, S., Levy, P. M. & Fert, A. Mechanisms of Spin-Polarized Current-Driven Magnetization Switching. *Phys. Rev. Lett.* **88**, 236601 (2002).

103 Zahnd, G. *et al.* Spin diffusion length and polarization of ferromagnetic metals measured by the spin-absorption technique in lateral spin valves. *Phys. Rev. B* **98**, 174414 (2018).

104 Rojas-Sánchez, J. C. *et al.* Spin Pumping and Inverse Spin Hall Effect in Platinum: The Essential Role of Spin-Memory Loss at Metallic Interfaces. *Phys. Rev. Lett.* **112**, 106602 (2014).

105 Srinivasan, S., Diep, V., Behin-Aein, B., Sarkar, A. & Datta, S. in *Handbook of Spintronics* (eds Yongbing Xu, David D. Awschalom, & Junsaku Nitta) 1281-1335 (Springer Netherlands, 2016).

106 Manchon, A., Koo, H. C., Nitta, J., Frolov, S. M. & Duine, R. A. New perspectives for Rashba spin–orbit coupling. *Nat. Mater.* **14**, 871-882 (2015).

107 Dyakonov, M. I. & Perel, V. I. Current-induced spin orientation of electrons in semiconductors. *Phys. Lett. A* **35**, 459-460 (1971).

108 D'Yakonov, M. I. & Perel', V. I. Possibility of Orienting Electron Spins with Current. *J. Exp. Theor. Phys.* **13**, 467 (1971).

109 Chazalviel, J. N. & Solomon, I. Experimental Evidence of the Anomalous Hall Effect in a Nonmagnetic Semiconductor. *Phys. Rev. Lett.* **29**, 1676-1679 (1972).

110 Wunderlich, J., Kaestner, B., Sinova, J. & Jungwirth, T. Experimental Observation of the Spin-Hall Effect in a Two-Dimensional Spin-Orbit Coupled Semiconductor System. *Phys. Rev. Lett.* **94**, 047204 (2005).

111 Kato, Y. K., Myers, R. C., Gossard, A. C. & Awschalom, D. D. Observation of the Spin Hall Effect in Semiconductors. *Science* **306**, 1910-1913 (2004).

112 Saitoh, E., Ueda, M., Miyajima, H. & Tatara, G. Conversion of spin current into charge current at room temperature: Inverse spin-Hall effect. *Appl. Phys. Lett.* **88**, 182509 (2006).

113 Valenzuela, S. O. & Tinkham, M. Direct electronic measurement of the spin Hall effect. *Nature* **442**, 176-179 (2006).

114 Berger, L. Influence of spin-orbit interaction on the transport processes in ferromagnetic nickel alloys, in the presence of a degeneracy of the 3d band. *Physica* **30**, 1141-1159 (1964).

115 Asik, J. R., Ball, M. A. & Slichter, C. P. Spin-Flip Scattering of Conduction Electrons from Impurities. *Phys. Rev. Lett.* **16**, 740-743 (1966).

116 Pai, C.-F., Mann, M., Tan, A. J. & Beach, G. S. D. Determination of spin torque efficiencies in heterostructures with perpendicular magnetic anisotropy. *Phys. Rev. B* **93**, 144409 (2016).

117 Zhang, B. *et al.* Energy-Efficient Domain-Wall Motion Governed by the Interplay of Helicity-Dependent Optical Effect and Spin-Orbit Torque. *Phys. Rev. Appl.* **11**, 034001 (2019).

118 Lee, O. J. *et al.* Central role of domain wall depinning for perpendicular magnetization switching driven by spin torque from the spin Hall effect. *Phys. Rev. B* **89**, 024418 (2014).

119 Bhowmik, D. *et al.* Deterministic Domain Wall Motion Orthogonal To Current Flow Due To Spin Orbit Torque. *Sci. Rep.* **5**, 11823 (2015).

120 Emori, S., Bauer, U., Ahn, S.-M., Martinez, E. & Beach, G. S. D. Current-driven dynamics of chiral ferromagnetic domain walls. *Nat. Mater.* **12**, 611-616 (2013).

121 Li, D. *et al.* Current-Induced Domain Wall Motion and Tilting in Perpendicularly Magnetized Racetracks. *Nanoscale Res. Lett.* **13**, 238 (2018).

122 Miron, I. M. *et al.* Fast current-induced domain-wall motion controlled by the Rashba effect. *Nat. Mater.* **10**, 419-423 (2011).

123 Chen, T.-Y. *et al.* Efficient Spin–Orbit Torque Switching with Nonepitaxial Chalcogenide Heterostructures. *ACS Appl. Mater. Interfaces* **12**, 7788-7794 (2020).

124 Liu, L., Lee, O. J., Gudmundsen, T. J., Ralph, D. C. & Buhrman, R. A. Current-Induced Switching of Perpendicularly Magnetized Magnetic Layers Using Spin Torque from the Spin Hall Effect. *Phys. Rev. Lett.* **109**, 096602 (2012).

125 Ramaswamy, R., Lee, J. M., Cai, K. & Yang, H. Recent advances in spin-orbit torques: Moving towards device applications. *Appl. Phys. Rev.* **5**, 031107 (2018).

126 Garello, K. *et al.* Symmetry and magnitude of spin–orbit torques in ferromagnetic heterostructures. *Nat. Nanotechnol.* **8**, 587-593 (2013).

127 Hayashi, M., Kim, J., Yamanouchi, M. & Ohno, H. Quantitative characterization of the spin-orbit torque using harmonic Hall voltage measurements. *Phys. Rev. B* **89**, 144425 (2014).

128 Pi, U. H. *et al.* Tilting of the spin orientation induced by Rashba effect in ferromagnetic metal layer. *Appl. Phys. Lett.* **97**, 162507 (2010).

129 Wong, Q. Y. *et al.* In situ Kerr and harmonic measurement in determining current-induced effective fields in MgO/CoFeB/Ta. *Journal of Physics D: Applied Physics* **51**, 115004 (2018).

130 Du, Y. *et al.* Disentanglement of Spin-Orbit Torques in Pt/Co Bilayers with the Presence of Spin Hall Effect and Rashba-Edelstein Effect. *Phys. Rev. Appl.* **13**, 054014 (2020).

131 Nagaosa, N., Sinova, J., Onoda, S., MacDonald, A. H. & Ong, N. P. Anomalous Hall effect. *Rev. Mod. Phys.* **82**, 1539-1592 (2010).

132 Cao, J. *et al.* Spin orbit torques induced magnetization reversal through asymmetric domain wall propagation in Ta/CoFeB/MgO structures. *Sci. Rep.* **8**, 1355 (2018).

133 Karplus, R. & Luttinger, J. M. Hall Effect in Ferromagnetics. *Phys. Rev.* **95**, 1154-1160 (1954).

134 Berger, L. Side-Jump Mechanism for the Hall Effect of Ferromagnets. *Phys. Rev. B* **2**, 4559-4566 (1970).

135 Lim, G. J., Gan, W. L., Law, W. C., Murapaka, C. & Lew, W. S. Spin-orbit torque induced multi-state magnetization switching in Co/Pt hall cross structures at elevated temperatures. *J. Magn. Magn. Mater.* **514**, 167201 (2020).

136 Wang, X. & Manchon, A. Diffusive Spin Dynamics in Ferromagnetic Thin Films with a Rashba Interaction. *Phys. Rev. Lett.* **108**, 117201 (2012).

137 Kurebayashi, H. *et al.* An antidamping spin–orbit torque originating from the Berry curvature. *Nature Nanotechnology* **9**, 211 (2014).

138 Qiu, X. *et al.* Spin–orbit-torque engineering via oxygen manipulation. *Nature Nanotechnology* **10**, 333 (2015).

139 van der Bijl, E. & Duine, R. A. Current-induced torques in textured Rashba ferromagnets. *Phys. Rev. B* **86**, 094406 (2012).

140 Kim, K.-W., Seo, S.-M., Ryu, J., Lee, K.-J. & Lee, H.-W. Magnetization dynamics induced by in-plane currents in ultrathin magnetic nanostructures with Rashba spin-orbit coupling. *Phys. Rev. B* **85**, 180404 (2012).

141 Pesin, D. A. & MacDonald, A. H. Quantum kinetic theory of current-induced torques in Rashba ferromagnets. *Physical Review B* **86**, 014416 (2012).

142 Miron, I. M. *et al.* Perpendicular switching of a single ferromagnetic layer induced by in-plane current injection. *Nature* **476**, 189-193 (2011).

143 Emori, S., Bauer, U., Ahn, S. M., Martinez, E. & Beach, G. S. Current-driven dynamics of chiral ferromagnetic domain walls. *Nat Mater* **12**, 611-616 (2013).

144 Ryu, K.-S., Thomas, L., Yang, S.-H. & Parkin, S. Chiral spin torque at magnetic domain walls. *Nat. Nanotechnol.* **8**, 527 (2013).

145 Torrejon, J. *et al.* Interface control of the magnetic chirality in CoFeB/MgO heterostructures with heavy-metal underlayers. *Nature Communications* **5**, 4655 (2014).

146 Liu, R. H., Lim, W. L. & Urazhdin, S. Dynamical Skyrmion State in a Spin Current Nano-Oscillator with Perpendicular Magnetic Anisotropy. *Physical Review Letters* **114**, 137201 (2015).

147 Awad, A. A. *et al.* Long-range mutual synchronization of spin Hall nano-oscillators. *Nature Physics* **13**, 292 (2016).

148 van den Brink, A. *et al.* Field-free magnetization reversal by spin-Hall effect and exchange bias. *Nature Communications* **7**, 10854 (2016).

149 Fukami, S., Zhang, C., DuttaGupta, S., Kurenkov, A. & Ohno, H. Magnetization switching by spin–orbit torque in an antiferromagnet–ferromagnet bilayer system. *Nat. Mater.* **15**, 535 (2016).

150 William, A. B. *et al.* Analogue spin–orbit torque device for artificial-neural-network-based associative memory operation. *Applied Physics Express* **10**, 013007 (2017).

151 Andy, T. Memristor-based neural networks. *Journal of Physics D: Applied Physics* **46**, 093001 (2013).

152 Kang, W. *et al.* Reconfigurable Codesign of STT-MRAM Under Process Variations in Deeply Scaled Technology. *IEEE Trans. Electron Devices* **62**, 1769-1777 (2015).

153 Wu, B., Cheng, Y., Yang, J., Todri-Sanial, A. & Zhao, W. Temperature Impact Analysis and Access Reliability Enhancement for 1T1MTJ STT-RAM. *IEEE Transactions on Reliability* **65**, 1755-1768 (2016).

154 Fukami, S., Anekawa, T., Zhang, C. & Ohno, H. A spin–orbit torque switching scheme with collinear magnetic easy axis and current configuration. *Nat. Nanotechnol.* **11**, 621 (2016).

155 Vansteenkiste, A. *et al.* The design and verification of MuMax3. *AIP Advances* **4**, 107133 (2014).

156 Eyrich, C. *et al.* Exchange stiffness in thin film Co alloys. *J. Appl. Phys.* **111**, 07C919 (2012).

157 Sampaio, J., Cros, V., Rohart, S., Thiaville, A. & Fert, A. Nucleation, stability and current-induced motion of isolated magnetic skyrmions in nanostructures. *Nat. Nanotechnol.* **8**, 839-844 (2013).

158 Metaxas, P. J. *et al.* Creep and Flow Regimes of Magnetic Domain-Wall Motion in Ultrathin Pt/Co/Pt Films with Perpendicular Anisotropy. *Phys. Rev. Lett.* **99**, 217208 (2007).

159 Han, J. *et al.* Room-Temperature Spin-Orbit Torque Switching Induced by a Topological Insulator. *Phys. Rev. Lett.* **119**, 077702 (2017).

160 Wang, Y., Deorani, P., Qiu, X., Kwon, J. H. & Yang, H. Determination of intrinsic spin Hall angle in Pt. *Appl. Phys. Lett.* **105**, 152412 (2014).

161 Nakagawara, K. *et al.* Temperature-dependent spin Hall effect tunneling spectroscopy in platinum. *Appl. Phys. Lett.* **115**, 162403 (2019).

162 Pai, C.-F., Ou, Y., Vilela-Leão, L. H., Ralph, D. C. & Buhrman, R. A. Dependence of the efficiency of spin Hall torque on the transparency of Pt/ferromagnetic layer interfaces. *Phys. Rev. B* **92**, 064426 (2015).

163 Phu, P. *et al.* Bolometric ferromagnetic resonance techniques for characterising spin-Hall effect at high temperatures. *J. Magn. Magn. Mater.* **485**, 304-307 (2019).

164 Kim, J. *et al.* Anomalous temperature dependence of current-induced torques in CoFeB/MgO heterostructures with Ta-based underlayers. *Phys. Rev. B* **89**, 174424 (2014).

165 Tsai, T. Y., Chen, T. Y., Wu, C. T., Chan, H. I. & Pai, C. F. Spin-orbit torque magnetometry by wide-field magneto-optical Kerr effect. *Sci Rep* **8**, 5613 (2018).

166 Zhou, Y., Mansell, R., Valencia, S., Kronast, F. & van Dijken, S. Temperature dependence of the Dzyaloshinskii-Moriya interaction in ultrathin films. *Phys. Rev. B* **101**, 054433 (2020).

167 Khadka, D., Karayev, S. & Huang, S. X. Dzyaloshinskii–Moriya interaction in Pt/Co/Ir and Pt/Co/Ru multilayer films. *J. Appl. Phys.* **123**, 123905 (2018).

168 Rahaman, S. Z. *et al.* Pulse-Width and Temperature Effect on the Switching Behavior of an Etch-Stop-on-MgO-Barrier Spin-Orbit Torque MRAM Cell. *IEEE Electron Device Lett.* **39**, 1306-1309 (2018).

169 Wang, S. *et al.* in *2016 53nd ACM/EDAC/IEEE Design Automation Conference (DAC).* 1-6.

170 Sengupta, A., Liyanagedera, C. M., Jung, B. & Roy, K. Magnetic Tunnel Junction as an On-Chip Temperature Sensor. *Sci. Rep.* **7**, 11764 (2017).

171 Lim, G. J., Gan, W. & Lew, W. S. Effect of seed and interlayer Pt thickness on spin-orbit torque efficiency in Co/Pt multilayer with perpendicular magnetic anisotropy. *J. Phys. D: Appl. Phys* **53**, 505002 (2020).

172 Miron, I. M. *et al.* Perpendicular switching of a single ferromagnetic layer induced by in-plane current injection. *Nature* **476**, 189 (2011).

173 Lim, S. T., Tran, M., Chenchen, J. W., Ying, J. F. & Han, G. Effect of different seed layers with varying Co and Pt thicknesses on the magnetic properties of Co/Pt multilayers. *J. Appl. Phys.* **117**, 17A731 (2015).

174 Johnson, M. T., Bloemen, P. J. H., Broeder, F. J. A. d. & Vries, J. J. d. Magnetic anisotropy in metallic multilayers. *Rep. Prog. Phys.* **59**, 1409-1458 (1996).

175 Lin, C. J. *et al.* Magnetic and structural properties of Co/Pt multilayers. *J. Magn. Magn. Mater.* **93**, 194-206 (1991).

176 Chowdhury, P. *et al.* Effect of coherent to incoherent structural transition on magnetic anisotropy in Co/Pt multilayers. *J. Appl. Phys.* **112**, 023912 (2012).

177 Baek, S.-h. C. *et al.* Complementary logic operation based on electric-field controlled spin–orbit torques. *Nat. Electron.* **1**, 398-403 (2018).

178 Lim, G. J., Chua, D., Gan, W., Murapaka, C. & Lew, W. S. Programmable Spin–Orbit-Torque Logic Device with Integrated Bipolar Bias Field for Chirality Control. *Adv. Electron. Mater.* **n/a**, 1901090.

179 Liu, L., Buhrman, R. A. & Ralph, D. C. Review and Analysis of Measurements of the Spin Hall Effect in Platinum. *arXiv e-prints*, arXiv:1111.3702 (2011).

180 Wong, Q. Y. *et al.* Enhanced Spin-Orbit Torques in Rare-Earth Pt/[Co/Ni]2/Co/Tb Systems. *Phys. Rev. Appl.* **11**, 024057 (2019).

181 Wang, R. *et al.* Enhancement of perpendicular magnetic anisotropy and spin-orbit torque in Ta/Pt/Co/Ta multi-layered heterostructures through interfacial diffusion. *Appl. Phys. Lett.* **114**, 042404 (2019).

182 Huang, K.-F., Wang, D.-S., Lin, H.-H. & Lai, C.-H. Engineering spin-orbit torque in Co/Pt multilayers with perpendicular magnetic anisotropy. *Appl. Phys. Lett.* **107**, 232407 (2015).

183 Nagaosa, N., Sinova, J., Onoda, S., MacDonald, A. H. & Ong, N. P. Anomalous Hall effect. *Revs. Mod. Phys.* **82**, 1539-1592 (2010).

184 Mathet, V. *et al.* Morphology and magnetic properties of Pt/Co/Pt sandwiches grown by argon sputter deposition. *J. Magn. Magn. Mater.* **260**, 295-304 (2003).

185 Takemura, Y., Lee, D.-Y., Lee, S.-E. & Park, J.-G. Dependency of tunneling magnetoresistance ratio on Pt seed-layer thickness for double MgO perpendicular magnetic tunneling junction spin-valves with a top Co2Fe6B2free layerex-situannealed at 400 °C. *Nanotechnology* **27**, 485203 (2016).

186 Ghosh, A., Garello, K., Avci, C. O., Gabureac, M. & Gambardella, P. Interface-Enhanced Spin-Orbit Torques and Current-Induced Magnetization Switching of $\mathrm{Pd}/\mathrm{Co}/{\mathrm{AlO}}_{x}$ Layers. *Phys. Rev. Appl.* **7**, 014004 (2017).

187 Huang, J. C. A. *et al.* Pt thickness and buffer layer effects on the structure and magnetism of Co/Pt multilayers. *Journal of Magnetism and Magnetic Materials* **239**, 326-328 (2002).

188 Lim, J.-E. *et al.* Microstructural characterization of sputter-deposited Pt thin film electrode. *J. Mater. Res.* **19**, 460-468 (2004).

189 Moritz, J., Garcia, F., Toussaint, J. C., Dieny, B. & Nozières, J. P. Orange peel coupling in multilayers with perpendicular magnetic anisotropy: Application to (Co/Pt)-based exchange-biased spin-valves. *Europhysics Letters (EPL)* **65**, 123-129 (2004).

190 Rossnagel, S. M. Characteristics of ultrathin Ta and TaN films. *Journal of Vacuum Science & Technology B: Microelectronics and Nanometer Structures Processing, Measurement, and Phenomena* **20**, 2328-2336 (2002).

191 Zhang, J., Huai, Y., Chen, L. & Zhang, J. Formation of low resistivity alpha Ta by ion beam sputtering. *Journal of Vacuum Science & Technology B: Microelectronics and Nanometer Structures Processing, Measurement, and Phenomena* **21**, 237-240 (2003).

192 Agustsson, J. S. *et al.* Electrical resistivity and morphology of ultra thin Pt films grown by dc magnetron sputtering on SiO2. *J. Phys. Conf. Ser.* **100**, 082006 (2008).

193 Baker, P. N. Preparation and properties of tantalum thin films. *Thin Solid Films* **14**, 3-25 (1972).

194 Woo, S., Mann, M., Tan, A. J., Caretta, L. & Beach, G. S. D. Enhanced spin-orbit torques in Pt/Co/Ta heterostructures. *Appl. Phys. Lett.* **105**, 212404 (2014).

195 Pi, U. H. *et al.* Tilting of the spin orientation induced by Rashba effect in ferromagnetic metal layer. *Appl. Phys. Lett.* **97**, 162507 (2010).

196 Yang, M. *et al.* Spin-orbit torque in Pt/CoNiCo/Pt symmetric devices. *Sci. Rep.* **6**, 20778 (2016).

197 Martinez, E., Emori, S. & Beach, G. S. D. Current-driven domain wall motion along high perpendicular anisotropy multilayers: The role of the Rashba field, the spin Hall effect, and the Dzyaloshinskii-Moriya interaction. *Appl. Phys. Lett.* **103**, 072406 (2013).

198 Amin, V. P. & Stiles, M. D. Spin transport at interfaces with spin-orbit coupling: Phenomenology. *Phys. Rev. B* **94**, 104420 (2016).

199 Wang, K. *et al.* Optimization of Co/Pt multilayers for applications of current-driven domain wall propagation. *J. Appl. Phys.* **110**, 083913 (2011).

200 Hao, Q. & Xiao, G. Giant spin Hall effect and magnetotransport in a Ta/CoFeB/MgO layered structure: A temperature dependence study. *Phys. Rev. B* **91**, 224413 (2015).

201 Cecot, M. *et al.* Influence of intermixing at the Ta/CoFeB interface on spin Hall angle in Ta/CoFeB/MgO heterostructures. *Sci. Rep.* **7**, 968 (2017).

202 Nguyen, M.-H. *et al.* Enhancement of the anti-damping spin torque efficacy of platinum by interface modification. *Appl. Phys. Lett.* **106**, 222402 (2015).

203 Zhang, W., Han, W., Jiang, X., Yang, S.-H. & S. P. Parkin, S. Role of transparency of platinum–ferromagnet interfaces in determining the intrinsic magnitude of the spin Hall effect. *Nat. Phys.* **11**, 496-502 (2015).

204 Bonhomme, P. *et al.* Circuit Simulation of Magnetization Dynamics and Spin Transport. *IEEE Trans. Electron Devices* **61**, 1553-1560 (2014).

205 Hong, S., Sayed, S. & Datta, S. Spin Circuit Representation for the Spin Hall Effect. *IEEE Trans. Nanotechnol.* **15**, 225-236 (2016).

206 Kim, N. S. *et al.* Leakage current: Moore's law meets static power. *Computer* **36**, 68-75 (2003).

207 Behin-Aein, B., Datta, D., Salahuddin, S. & Datta, S. Proposal for an all-spin logic device with built-in memory. *Nat. Nanotechnol.* **5**, 266 (2010).

208 Wang, S. *et al.* Proposal of a magneto-electric effect assisted all spin logic device. *J. Phys. D: Appl. Phys* **52**, 125001 (2019).

209 Cao, K. *et al.* In-memory direct processing based on nanoscale perpendicular magnetic tunnel junctions. *Nanoscale* **10**, 21225-21230 (2018).

210 Yao, X. *et al.* Magnetic Tunnel Junction-Based Spintronic Logic Units Operated by Spin Transfer Torque. *IEEE Trans. Nanotechnol.* **11**, 120-126 (2012).

211 Wang, X. *et al.* Field-Free Programmable Spin Logics via Chirality-Reversible Spin–Orbit Torque Switching. *Adv. Mater.* **30**, 1801318 (2018).

212 Wan, C. *et al.* Programmable Spin Logic Based on Spin Hall Effect in a Single Device. *Adv. Electron. Mater.* **3**, 1600282 (2017).

213 Ikeda, S. *et al.* A perpendicular-anisotropy CoFeB–MgO magnetic tunnel junction. *Nat. Mater.* **9**, 721-724 (2010).

214 Ueda, K., Pai, C.-F., Tan, A. J., Mann, M. & Beach, G. S. D. Effect of rare earth metal on the spin-orbit torque in magnetic heterostructures. *Appl. Phys. Lett.* **108**, 232405 (2016).

215 Reynolds, N. *et al.* Spin Hall torques generated by rare-earth thin films. *Phys. Rev. B* **95**, 064412 (2017).

216 Tanaka, T. & Kontani, H. Intrinsic spin and orbital Hall effects in heavy-fermion systems. *Phys. Rev. B* **81**, 224401 (2010).

217 Bang, D. *et al.* Enhancement of spin Hall effect induced torques for current-driven magnetic domain wall motion: Inner interface effect. *Phys. Rev. B* **93**, 174424 (2016).

218 Xu, Z. *et al.* Giant Spin Hall Effect in Cu–Tb Alloy Thin Films. *ACS Appl. Mater. Interfaces* **12**, 32898-32904 (2020).

219 Fritz, K., Wimmer, S., Ebert, H. & Meinert, M. Large spin Hall effect in an amorphous binary alloy. *Phys. Rev. B* **98**, 094433 (2018).

220 Legrand, W. *et al.* Room-Temperature Current-Induced Generation and Motion of sub-100 nm Skyrmions. *Nano Lett.* **17**, 2703-2712 (2017).

221 Ramaswamy, R. *et al.* Extrinsic Spin Hall Effect in Cu1-x/Ptx. *Phys. Rev. Appl.* **8**, 024034 (2017).

222 Niimi, Y. *et al.* Giant Spin Hall Effect Induced by Skew Scattering from Bismuth Impurities inside Thin Film CuBi Alloys. *Phys. Rev. Lett.* **109**, 156602 (2012).

223 Musha, A., Kanno, Y. & Ando, K. Extrinsic-intrinsic crossover of the spin Hall effect induced by alloying. *Phys. Rev. Mater.* **3**, 054411 (2019).

224 Tian, K. & Tiwari, A. CuPt Alloy Thin Films for Application in Spin Thermoelectrics. *Sci. Rep.* **9**, 3133 (2019).

225 Sharmin, S., Shim, Y. & Roy, K. Magnetoelectric oxide based stochastic spin device towards solving combinatorial optimization problems. *Sci. Rep.* **7**, 11276 (2017).

226 Tan, F. N. *et al.* Electric field control for energy efficient domain wall injection. *J. Magn. Magn. Mater.* **485**, 174-179 (2019).

227 Tan, F. N. *et al.* High velocity domain wall propagation using voltage controlled magnetic anisotropy. *Sci. Rep.* **9**, 7369 (2019).

228 Yamada, K. *et al.* Electric Field Modulation of Magnetic Anisotropy in MgO/Co/Pt Structure. *Appl. Phys. Express* **6**, 073004 (2013).

229 Chiba, D. *et al.* Electric-field control of magnetic domain-wall velocity in ultrathin cobalt with perpendicular magnetization. *Nat. Commun.* **3**, 888 (2012).

230 McCray, M. T., Abeed, M. A. & Bandyopadhyay, S. Electrically programmable probabilistic bit anti-correlator on a nanomagnetic platform. *Sci. Rep.* **10**, 12361 (2020).

231 Behin-Aein, B., Diep, V. & Datta, S. A building block for hardware belief networks. *Sci. Rep.* **6**, 29893 (2016).

232 Roy, K., Sengupta, A. & Shim, Y. Perspective: Stochastic magnetic devices for cognitive computing. *J. Appl. Phys.* **123**, 210901 (2018).

233 Nasrin, S., Drobitch, J. L., Bandyopadhyay, S. & Trivedi, A. R. Low Power Restricted Boltzmann Machine Using Mixed-Mode Magneto-Tunneling Junctions. *IEEE Electron Device Lett.* **40**, 345-348 (2019).

234 Peng, X. *et al.* Quantum Adiabatic Algorithm for Factorization and Its Experimental Implementation. *Phys. Rev. Lett.* **101**, 220405 (2008).

235 Shim, Y., Jaiswal, A. & Roy, K. Ising computation based combinatorial optimization using spin-Hall effect (SHE) induced stochastic magnetization reversal. *J. Appl. Phys.* **121**, 193902 (2017).

236 Hopfield, J. J. Neural networks and physical systems with emergent collective computational abilities. *Proc. Natl. Acad. Sci.* **79**, 2554-2558 (1982).

List of Publications

1. **G. J. Lim**, W. L. Gan, and W. S. Lew, "Effect of Seed and Interlayer Pt on SOT in Co/Pt Multilayers", *Journal of Physics D: Applied Physics*, 53, 505002 (2020).
2. **G. J. Lim**, W. L. Gan, W. C. Law, C. Murapaka, and W. S. Lew, "Spin-Orbit Torque Driven Analogue-Like Behaviour in Co/Pt Hall Cross Structures at Elevated Temperatures", *Journal of Magnetism and Magnetic Materials*, 514, 167201 (2020).
3. **G. J. Lim**, D. Chua, W. L. Gan, C. Murapaka, and W. S. Lew, "Programmable Spin-Orbit Torque Logic Device with Integrated Bipolar Bias Field for Chirality Control", *Advanced Electronic Materials*, 1901090 (2020)
4. F. L. Luo, Q. Y. Wong, S. H. Li, F. N. Tan, **G. J. Lim**, X. Wang, and W. S. Lew, "Dependence of spin-orbit torque effective fields on magnetization uniformity in Ta/Co/Pt structure", *Scientific Reports*, 9(10776) (2019)

5. F. N. Tan, **G. J. Lim**, T. L. Jin, H. X. Liu, F. Poh, and W. S. Lew, "Electric field control on single and double Pt/Co heterostructure for enhanced thermal stability", *Journal of Magnetism and Magnetic Materials*, 490, 165448 (2019)
6. Q. Y. Wong, C. Murapaka, W. C. Law, W. L. Gan, **G. J. Lim**, and W. S. Lew, "Enhanced Spin-orbit Torques in Rare Earth Pt/[Co/Ni]2/Co/Tb systems", *Physical Review Applied*, 11, 024057 (2019)
7. S. Krishnia, C. Murapaka, P. Sethi, W. L. Gan, Q. Y. Wong, **G. J. Lim**, and W. S. Lew, "Current-induced spin-orbit effective field modulations in synthetic antiferromagnetic structures", *Journal of Magnetism and Magnetic Materials*, 475, 327-333 (2018)
8. S. H. Li, **G. J. Lim**, W. L. Gan, W. C. Law, F. N. Tan, and W. S. Lew, "Tuning the spin-orbit torque effective fields by varying Pt insertion layer thickness in perpendicularly magnetized Pt/Co/Pt(t)/Ta structures", *Journal of Magnetism and Magnetic Materials*, 473, 394-398 (2018)
9. F. N. Tan, **G. J. Lim**, W. C. Law, F. L. Luo, H. X. Liu, F. Poh, D. Shum, and W. S. Lew, "Electric Field control on Gated Pt/Co/SiO2 Heterostructure with Insulating Polymer", *Journal of Physics D: Applied Physics*, 51, 365001 (2018)
10. Q. Y. Wong, W. L. Gan, F.L Luo, **G. J. Lim**, C. C. I. Ang, F. N. Tan, W. C. Law, and W. S. Lew, "*In-situ* Kerr harmonic measurement in determining current-induced effective fields in MgO/CoFeB/Ta", *Journal of Physics D: Applied Physics*, 51, 115004 (2018)
11. M. Ramu, G. Sarjoosing, S. Krishnia, **G. J. Lim**, and W. S. Lew, "Spin orbit torque induced asymmetric depinning of chiral Néel domain wall in Co/Ni heterostructures", *Applied Physics Letters*, 110, 162402 (2017)
12. F. L. Luo, G. Sarjoosing, S. H. Li, **G. J. Lim**, F. N. Tan, C. Engel, S. F. Zhang, Ma Fusheng, Zhou Tiejun, and W. S. Lew, "Characterizing the spin orbit torque field-like term in in-plane magnetic system using transverse field", *Journal of Applied Physics*, 120, 083908 (2016)
13. D. W. Wong, I. Purnama, **G. J. Lim**, W. L. Gan, C. Murapaka, and W. S. Lew, "Current-induced three-dimensional domain wall propagation in cylindrical NiFe nanowires", *Journal of Applied Physics*, 119, 153902 (2016)
14. S. F. Zhang, W. L. Gan, J. S. Kwon, F. L. Luo, **G. J. Lim**, J. B. Wang, and W. S. Lew, "Highly efficient domain walls injection in perpendicular magnetic anisotropy memory devices", *Scientific Reports*, 6, 24804 (2016)

15. P. Sethi, M. Chandrasekhar, **G. J. Lim**, and W. S. Lew, “In-plane current induced domain wall nucleation and its stochasticity in perpendicular magnetic anisotropy Hall cross structures”, *Applied Physics Letters*, 107, 192401 (2015)

16. J. S. Kwon, G. Sarjoosing, **G. J. Lim**, I. S. Kerk, C. H. Chang, K. Roy, and W. S. Lew, “Low field domain wall dynamics in artificial spin-ice basis structure”, *Journal of Applied Physics*, 118, 163907 (2015)

17. I. Purnama, I. S. Kerk, **G. J. Lim**, and W. S. Lew, “Coupled Neel domain wall motion in sandwiched perpendicular magnetic anisotropy nanowires”, *Scientific Reports*, 5, 8754 (2015)

List of Conferences

1. Impact of Stopping Voltage and Hopping Conduction on the Oxygen Vacancy Concentration of Multi-Level HfO2-Based Resistive Switching Devices”, D. J. J. Loy, P. A. Dananjaya, S. Chakrabarti, K. H. Tan, S. C. W. Chow, M. Y. Chee, J. R. Thong, K. Q. Hou, J. M. Ang, **G. J. Lim**, Y. C. Ee, and W. S. Lew, *Conference Proceedings in IEEE Silicon Nanoelectronics Workshop (2020)*
2. “Enhanced Spin Orbit Torques in Rare Earth Pt/[Co/Ni]2/Co/Tb Systems”, Q. Y. Wong, C. Murapaka, W. C. Law, W. L. Gan, **G. J. Lim**, and W. S. Lew, *2019 Annual Conference on Magnetism and Magnetic Materials (MMM 2019), Las Vegas, USA*
3. “Hopping Conduction Temperature Investigations on High Retention Electrochemical Metallization MgO-based Resistive Switching Devices in the Low Resistance State”, D. J. J. Loy, P. A. Dananjaya, W. C. Law, **G. J. Lim**, F. N. Tan, X. L. Hong, S. C. W. Chow, E. H. Toh, and W. S. Lew, *Electron Devices Technology and Manufacturing Conference, IEEE (2019)*
4. “Nearest Neighbor Hopping in High Retention MgO-based Resistive Switching Devices in the High Resistance State”, D. J. J. Loy, P. A. Dananjaya, W. C. Law, **G. J. Lim**, F. N. Tan, X. L. Hong, S. C. W. Chow, E. H. Toh, and W. S. Lew, *Materials Research Society Conference (2019)*
5. “Reconfigurable spin orbit torque logic”, **G. J. Lim**, W. L. Gan, and W. S. Lew, *2019 Annual Conference on Magnetism and Magnetic Materials (MMM 2019), Las Vegas, USA*
6. “The effect of inserting a Pt layer in Pt/Co/Ta structure on spin orbit torque”, S. H. Li, **G. J. Lim**, and W. S. Lew, *INTERMAG 2018, Singapore*
7. “Temperature Dependence Of Spin Orbit Torque Induced Magnetization Switching In Co/Pt Multilayers”, **G. J. Lim** and W. S. Lew, *62nd Annual Conference on Magnetism and Magnetic Materials (MMM 2017), Pittsburgh, USA*
8. “In-situ high temperature FMR measurements of pMTJ with various diffusion barrier cap”, W. C. Law, T. Tahmasebi, F. N. Tan, W. L. Gan, **G. J. Lim**, C. S. Seet, A. See, and W. S. Lew, *62nd Annual Conference on Magnetism and Magnetic Materials (MMM 2017), Pittsburgh, USA*
9. “Time Dynamics Study of Voltage Control Magnetic Anisotropy Using Gate Polymer”, F. N. Tan, **G. J. Lim**, W. C. Law, F. L. Luo, H. X. Liu, F.

Poh, D. Shum, and W. S. Lew, *62nd Annual Conference on Magnetism and Magnetic Materials (MMM 2017), Pittsburgh, USA*

10. HZ Biased Field Modulation of The Harmonic Measurement in the Determination Of The Effective Fields In MgO/CoFeB/W", Q. Y. Wong, **G. J. Lim**, W. L. Gan, and W. S. Lew, *62nd Annual Conference on Magnetism and Magnetic Materials (MMM 2017), Pittsburgh, USA*

11. "Skyrmion in-line injection and driving by spin Hall torque", W. L. Gan, S. Krishnia, Q. Y. Wong, W. C. Law, **G. J. Lim**, and W. S. Lew, *INTERMAG 2017, Dublin, Ireland*

12. "Interfacial Dzyaloshinkii-Moriya interaction-induced domain wall depinning anomaly", **G. J. Lim**, H. K. Teoh, G. Sarjoosing, C. Engel, and W. S. Lew, *The 4th International Conference of Asian Union of Magnetics Societies (IcAUMS 2016), Tainan, Taiwan*

13. "Flip-Flop SR Latch and Half-Adder Logic Circuit Configurations using SOT-MTJ", D. J. J. Loy, **G. J. Lim**, G. Sarjoosing, and W. S. Lew, *The 4th International Conference of Asian Union of Magnetics Societies (IcAUMS 2016), Tainan, Taiwan*

14. "Characterization of the field-like term of spin-orbit torque in Ta/Co/Pt by sweeping transverse field", F. L. Luo, **G. J. Lim**, G. Sarjoosing, C. Engel, T. J. Zhou, and W. S. Lew, *The 4th International Conference of Asian Union of Magnetics Societies (IcAUMS 2016), Tainan, Taiwan*

15. "Chirality-dependent domain wall pinning and oscillation at Ta hall probe in perpendicular magnetic anisotropy nanowires", J. S. Kwon, H. K. Teoh, G. Sarjoosing, **G. J. Lim**, C. H. Chang, K. Roy, and W. S. Lew, *2016 Joint MMM-Intermag Conference, San Diego, USA*

16. "Neel coupling in sandwiched perpendicular magnetic anisotropy nanowires", I. Purnama, I. S. Kerk, **G. J. Lim**, and W. S. Lew, *4th International Conference on Superconductivity and Magnetism 2014, Antalya, Turkey*

17. "Spin-Hall torque induced domain wall motion in PMA nanowire network", J. S. Kwon, H. K. Teoh, G. Sarjoosing, **G. J. Lim**, C. H. Chang, K. Roy, and W. S. Lew, *2016 Joint MMM-Intermag Conference, San Diego, USA*

18. "Neel coupling in sandwiched perpendicular magnetic anisotropy nanowires", I. Purnama, I. S. Kerk, **G. J. Lim**, and W. S. Lew, *INTERMAG 2014 Dresden, Germany*

List of Intellectual Properties

1. “Spin-Orbit Torque Driven Logic”, **G. J. Lim**, C. Murapaka, and W. S. Lew, Technology Disclosure, NTU TD ref 2018-197 (2018)
2. “A High-Temperature Ferromagnetic Resonance Spectrometer”, **G. J. Lim** and W. S. Lew, Technology Disclosure, NTU TD ref 2018-232 (2018)
3. “Integrated Circuits With Magnetic Tunnel Junctions and Methods of Producing The Same”, W. C. Law, T. Tahmasebi, C. S. Seet, A. See, **G. J. Lim**, and W. S. Lew, US Patent Application, GF Ref. No.: JSG053
4. “A Ferromagnetic Resonance Spectrometer", W. S. Lew, and **G. J. Lim,** Technology Disclosure, NTU ref TD/326/16
5. “Magnetic memory devices and methods of operating the same", W. S. Lew, S. F. Zhang, W. L. Gan, and **G. J. Lim**, PCT Application No: PCT/SG2016/050526
6. “Low-power bit writing in perpendicular magnetic anisotropy memory devices”, W. S. Lew, S. F. Zhang, W. L. Gan, and **G. J. Lim,** Singapore Provisional Patent, 10201508828X (2015)
7. “A magnetron thin film sputter deposition system”, W. S. Lew and **G. J. Lim,** Technology Disclosure, NTU ref TD/203/14 (2014)
8. “A resistively-heated thin film evaporation deposition system”, W. S. Lew and **G. J. Lim,** Technology Disclosure, NTU ref TD/202/14 (2014)
9. “An electron beam-heated thin film evaporation deposition system”, W. S. Lew and **G. J. Lim,** Technology Disclosure, NTU ref TD/202/14 (2014)
10. “Non-volatile memory architecture based on domain wall remote driving sandwiched perpendicular magnetic anisotropy nanowires”, W. S. Lew, I. Purnama, I. S. Kerk, and **G. J. Lim,** Technology Disclosure, NTU ref TD/268/13 (2013)

Award

1. Magnetism and Magnetic Materials conference award for the 2019 MMM Conference, Las Vegas